University of Stavanger

FACULTY OF SCIENCE AND TECHNOLOGY

MASTER'S THESIS

Study programme/specialization: Petroleum Geoscience Engineering	Spring semester, 2018 Open / Confidential
Author: Tine Vigdel Bredal	…… (signature of author)
Programme coordinator: Supervisor(s): Udo Zimmermann	
Title of master's thesis: **Micro- and nano-analyses of fracture-filling after flooding on-shore chalk with different IOR fluids**	
Credits: 30	
Keywords: Chalk, hollow cylinder Flooding brines, MgCl2, NaCl, SSW Minerals, precipitation, distribution Scanning Electron Microscopy (SEM) Mineral Liberation Analyser (MLA) Transmission Electron Microscopy (TEM)	Number of pages: …… + supplemental material/other: …… Stavanger, 22.06.2018

Micro- and nano-analyses of fracture-filling after flooding on-shore chalk with different IOR fluids

by

Tine Vigdel Bredal

MSc Thesis

Petroleum Geosciences Engineering

Faculty of science and Technology

University of Stavanger

June 2018

Acknowledgement

Primarily, I would like to share my gratitude to Professor Udo Zimmermann for giving me the opportunity to conduct this specific topic which has been a highly desirable challenge. Your dedication to geology is inspiring, and it is catching. Not only through this thesis have your attitude been appreciated, but also during unforgettable fieldtrips that you have previously provided.

I will especially express my gratefulness to PhD student Mona Wetrhus Minde for giving valuable advices from the very start considering all aspect of the subject and for sharing experience in scanning electron microscope (SEM) procedures.

A gratitude goes to Caroline Ruud for her admirable attitude to new challenging tasks concerning sample preparation in lab, and Emanuela Iedidia Kallesten for teaching X-Ray Diffraction (XRD) methods. I would also like to thank Wakshum Mekonnen Tucho for implementing examination of Transmission Electron Microscope (TEM) samples.

I would like to thank Per Erik Vullum at SINTEF/NTNU for introducing me to cleanroom procedures and the FIB-TEM method. I will also express my appreciation to staff at the Bergakademie in Freiberg, Sabine Haser and Professor Bernhard Schultz for providing their Mineral Liberation Analysis (MLA) and completing MLA tests and assistance with following analysis.

Finally, I want to express my gratefulness to the IOR centre for funding's, for making this thesis possible and for letting me participate at the IOR-conference which was educational and entertaining.

Tine Vigdel Bredal

Table of contents

List of figures

List of tables

List of commonly used abbreviations

BSE – Backscattered Electrons

EDS – Energy Dispersive system

EOR – Enhanced oil Recovery

FIB – Focused Ion Beam

IOR – Improved Oil Recovery

LM – Light Microscopy

$MgCl_2$ – Magnesium Chloride

MLA – Mineral Liberation Analyzer

NaCl – Natrium Chloride

NCS – Norwegian Continental Shelf

NPD – Norwegian Petroleum Department

OBSV – Obourg quarry, Saint Vaast Formation

OLM – Optical Light Microscopy

SE – Secondary Electrons

SEM – Scanning Electron Microscopy

SSW – Synthetic Seawater

SSA – Specific Surface Area

TEM –Transmission electron microscopy

wt.% – Weight percent

XRD – X-ray diffraction

Abstract

Water injection into the Ekofisk-reservoir was introduced in 1987 to enhance oil recovery (EOR) dissolution and precipitation by exposing chalk to various brines at reservoir conditions, which further increased deformation of chalk matrix. This deformation affected mechanical properties of the tested samples and is referred to as water weakening of chalk.

This thesis has focused on identifying mineral changes and mapping the distribution of precipitated mineral during flooding of samples which have an artificial fracture and will compare hollow cylinder to intact chalk cores. Methods used to achieve a mineralogic map are:

- Optical Light Microscopy (OLM)
- Light microscopy (LM)
- X-ray diffraction (XRD)
- Scanning Electron Microscopy (SEM)
- Focused Ion Beam (FIB) sample for Transmission Electron Microscopy (TEM)
- Mineral Liberation Analyzer (MLA)

All cores tested, either intact or hollow and representing all combinations of brine injected, distributed an increased abundance of chlorite. The most sensational observation was the precipitation of magnesite inside the core of the hollow cylinder flooded by $MgCl_2$, and the distinct boundary that this distribution created. Ilmenite was also observed at the same location, while calcite was limited to the matrix itself. Pyrite was not observed in the reference rock, but this was however identified in cores flooded by both $MgCl_2$ and SSW. One non-fractured core injected by SSW experienced clogging after 20 days of flooding. The two samples from this core provided similar composition as the reference rock, hence the reduction of permeability was related to the composition of the brine (SSW) as the comparable core injected with $MgCl_2$ experienced a more dramatic calcite dissolution. This core that clogged also experienced a rapid creep phase and imply that pores could have been clogged solely due to the compression and dissolution of grain to grain contacts during flooding.

These results, among others, allows an interpretation that dissolution of original grains and distribution of precipitated minerals is dependent on a variety of processes. The type of brine injected, distribution of porous network and the distance from the inlet are essential parameter which affect the precipitation in the hollow core, so verified in this study. The reactivity and the content of silicate and clay minerals may also influence the process.

1. Introduction

In June last year, (2017), The Norwegian Petroleum Department (NPD) estimated the recovery factor or the proportion of oil originally in place extracted from fields on the Norwegian Continental Shelf (NCS) to 47 per cent, and average global recovery of slightly less than 40 per cent. By implementing new technologies based on research, the recovery factor is continuously increasing. This refers to Improved Oil Recovery (IOR). IOR may recover mobile oil which is not recovered by primary methods. One method is to stimulate oil production by water, gas or polymer- injection, another method may include improved reservoir management, cost reduction initiatives and advanced methods or tertiary recovery. Enhanced Oil Recovery (EOR), or the tertiary recovery, is an approach which is used to recover mostly immobile oil that remains in the reservoir after production by conventional methods. Research conducted at the IOR centre of Norway and their aim to disseminate their knowledge, may contribute to increased oil recovery not only on the NCS, but worldwide.

The ultimate oil recovery is usually lower for carbonate reservoirs compared to sandstone reservoirs. The two different reservoir types have elementary dissimilarities concerning essential properties. Carbonate reservoirs have a tendency in not being water-wet, have often low permeability and heterogeneity of rock properties compared to properties of sandstone reservoirs. Porosity is often very high for carbonate reservoirs, 40-50 % (Korsnes et al., 2008) (Sulak and Danielsen, 1989) and has great potential to accumulate oil. By implementing new technologies especially targeting carbonate reservoirs, large volumes of increased oil recovery may be created.

Ekofisk is a carbonate reservoir which is located in the southern part of the Norwegian sector in the North Sea. Oil production started in 1971 and had an initial expected recovery factor of 17 per cent according to NPD, and it was originally planned to produce hydrocarbons by pressure depletion. A substantial increase in oil recovery followed by implementing previously mentioned techniques as water injection. Large-scale water injection started in 1987, (Fig. 1) and continued in subsequent years. Experience proved that water displaced the oil much more effectively than anticipated, and the expected final recovery factor for Ekofisk is now estimated to be over 50 per cent according to NPD (2017). In addition to the water injection, deformation of chalk matrix and compaction of the soft chalk provides extra force to drainage of the field. This is referred to as water weakening effect (Risnes et al., 2005).

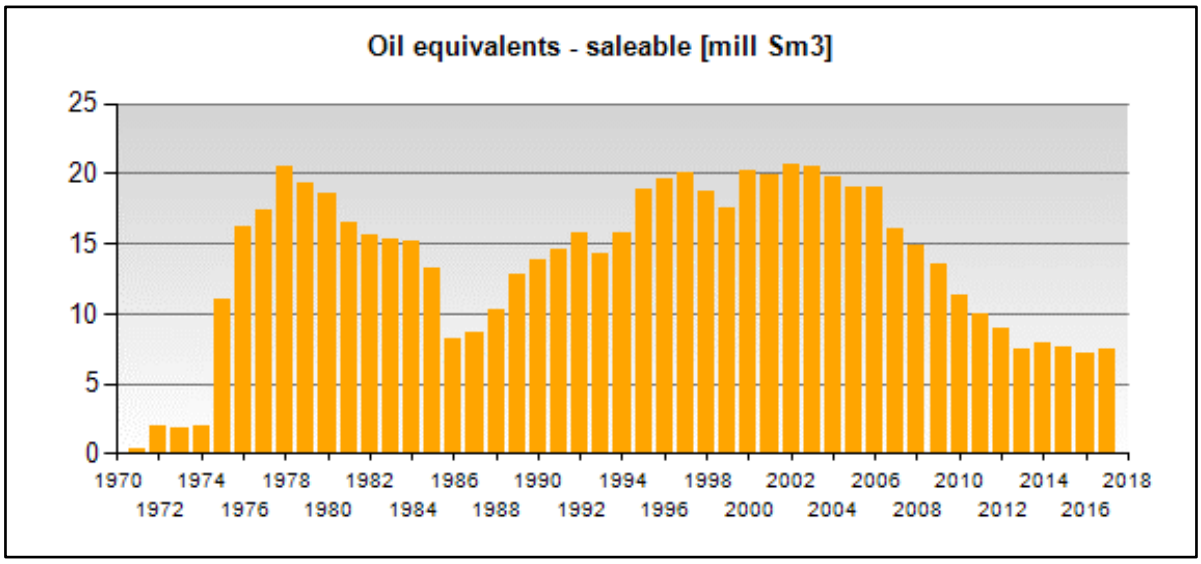

Fig. 1) The diagram distributes recovered oil equivalents on the Ekofisk Field since the start of the production in 1971 and until present. By implementing water-injection in 1987 the recovery rate increased (Figure: www.npd.no).

Increased recovery at the Ekofisk field since the initiation of water injection occurred not only during injection, but also after. The lowering of resistance to compaction, indicate a change of the properties of the chalk. The topic is of high interest among researchers as details around the process of water injection and its consequence is still not completely understood. However, research has shown that the mineral exchange is dependent on the composition of the brine (Strand et al., 2003) (Korsnes et al., 2008). It is proposed that during this exchange, the chalk matrix is dissolved and will influence mineral precipitation. This mechanism has proved to be dependent on effective stresses, porosity, chemistry, diagenetic processes and cementation (Bjørlykke and Høeg, 1997). The dissolution of calcium carbonate, $CaCO_3$ to Ca^{2+} and CO_3^{2-}. ions, when injected with brine, has shown that new precipitated minerals will have a smaller grainsize and reduce overall mass and hence reduce the contactpressure created by capillary forces and contributes to weakening of the chalk. Mineral changes are, as previously mentioned, dependent on composition of the injected brine and reservoir properties. Furthermore researchers have observed that this process is also dependent on non-carbonate minerals in the original matrix of the reservoir (Madland et al., 2011) (Megawati et al., 2015). Re-precipitation of Si-bearing minerals leads to enhanced calcite dissolution and loss of matrix which could explain the high compaction in $MgCl_2$-flooded chalk (Andersen et al., 2017). Other research has shown that compaction can affect chemistry by pressure solution (Newman 1983). The increased stress applied on a core is transferred through grain to grain contacts which may result

in a continuous local dissolution (Paterson, 1973). The result of this chemical alteration may lead to a change in the wetting condition of the chalk. An initial oil-wet chalk surface will become water-wet due to injection of sulphate ions in the brine (Strand et al., 2007). All these processes contribute to enhanced oil recovery.

Properties of chalk reservoirs may vary according to variation in environmental conditions at the location as temperature, pH, depth at deposition and distance from shore and type of organic matter that has been deposited. The ideal situation would have been to study deeply buried offshore chalk originated from the Ekofisk field. Due to the expense, difficulty of collection and challenge to clean offshore samples, chalk cores with similar characteristics from accessible onshore outcrop of the Mons basin in Belgium were chosen for further studies. The chalk was deposited as the Saint Vaast Formation during the Upper Cretaceous. Its composition and characteristics are similar with chalk at Ekofisk (Hjuler and Fabricius, 2009).

Three hollow cylinder tests were implemented on chalk cores flooded respectively by magnesium chloride ($MgCl_2$), sodium chloride (NaCl) and synthetic seawater (SSW) in a previous study. The studied chalk originates from Obourg quarry, more specifically Saint Vaast formation, located in Mons basin in southern Belgium. The age is Upper Cretaceous, and its composition and characteristics are thought to be similar with chalk at Ekofisk, a giant hydrocarbon reservoir in the North Sea. The authors compared these three flow-through experiments with two intact cores flooded by $MgCl_2$ and SSW at reservoir temperatures. No significant difference in yield strength was found, yet the average yield strength is slightly higher for intact cores.

1.1 Objective of thesis

Precipitation of minerals is a process that occurs when chalk gets in contact with non-equilibrium brines, as this specific rock is easy to alter. Mineral changes may increase oil recovery, but surely change rock mechanical parameters like porosity, permeability, density etc. By mapping those mineral changes and implementing these results to reservoir conditions, it may provide predicted results after a longer flooding time. In this specific study a hole was drilled in the centre core of approximately 3 mm in diameter to investigate the change in properties followed by a different water flow compared to intact cores. The focus will therefore be to attempt answering the following key issues:

- Identification of minerals which are precipitating during flooding and their formation in relation to the injected brine.
- How will the precipitated minerals distribute along and across the flooding direction comparing different brines?
- Will the fracture influence the distribution of precipitated minerals?
- Try to understand and proof dissolution and precipitation processes.

1.2 Outline

1. Fracturing
2. Flooding by NaCl, $MgCl_2$ and SSW.
3. Beforehand, samples were observed with a lower magnification to classify and study textural characteristics of the chalk, and substantial variation between the different cores.
4. The minerals that have precipitated during flooding will mainly be studied on nano-and microscale.

2. Study object

Chalk is a marine sedimentary rock formed mainly by calcareous micro- and nannofossils called coccolithophores (Fig 2.) They will normally degrade into individual skeletal plates called coccoliths.

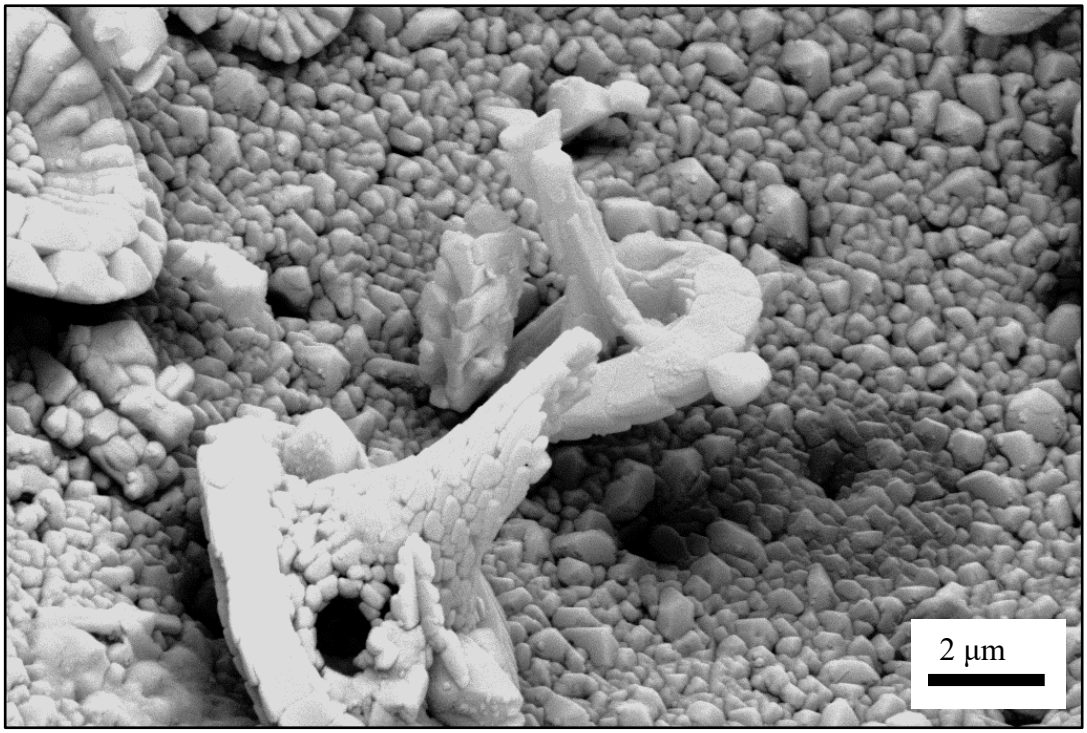

Fig. 2) Partly degraded coccolithophores. These microorganisms will normally degrade during compaction. Location inside a shell of a foraminifera may prevent degrading.

The size of the coccolithophores is clay to silt size and measure approximately 10 μm, whereas individual coccolith rings range between 0.3 and 5 μm (Hjuler and Fabricius, 2009). Abundant microfossils debris in chalk are foraminifera, bryozoan, echinoderms, brachiopods and bivalves. Chalk is mineralogically composed of mainly calcium carbonate ($CaCO_3$) where calcite is being the most common and stable form, followed by aragonite, and finally the unstable form known as vaterite. The crystal structure of calcium carbonate ($CaCO_3$) is trigonal, orthorhombic or hexagonal, respectively. Pure chalk has a density of 2,71 kg/m^3, is relatively soft and achieves a hardness of only 3 on Mohs scale.

Clay-minerals are major constituents of the non-carbonate content of chalk, either as detrital mineral or of authigenic origin. These impurities of chalk influence the colour of the rock in

darkening it slightly, while chalk is expected to be white when it comprises pure calcium carbonate ($CaCO_3$). Quartz is another phase common in the group of non-carbonate minerals in chalk from Mons. Chalk may be defined as a limestone and is further classified as fine-grained chalk of mudstone or pack stone (Dunham, 1962).

2.1 Chalk deposition and diagenesis

As coccolithophores die, they deposit in a basin and gradually accumulating a significant layer over millions of years. The carbonate ooze has initially a porosity which ranges from 60 to 80%, depending on the prevalence of hollow microfossils. As burial continues, fluid expulsion leads to compaction and lithification, forming a fine-grained sedimentary rock. Calcite particles recrystallize into more equant shapes and grow, and consequently expand pore -sizes. The stiffness of the rock increases and subsequently reduces the compaction rate (Fabricius, 2003). Porosity will normally not decrease any further, which indicates an absence of chemical compaction by calcite-calcite pressure dissolution and the porosity preserving effect of contact cementation. The increasing weight of overlaying sediments contributes to a gradual consolidation of the rock. Porosity may continue to reduce, due to mechanical compaction or pore-filling cementation via pressure dissolution. Abundant stylolites may indicate that pressure dissolution takes place between calcite and silicates as burial stress increases. High compaction rates may keep the particles in relative motion, and a low compaction rate will allow the formation of contact cement (Fabricius, 2003). Pore-filling cementation is dependent on pore-water chemistry and temperature. The initial porosity reduces, but still sustain high values around 35 – 50% (Hjuler and Fabricius, 2009). Depending on the environment it may be reduced to less than 20% (Fabricius, 2003). Presence of hydrocarbons causes a fall in effective burial stress, and the adsorption of polar hydrocarbons on the silicates may shield calcite from the silicate and further prevent diagenetic processes (Risnes, 2001).

2.2 Properties of chalk reservoirs

Despite the high porosity, chalk achieves a relatively low permeability ranging between 1 to-5 mD (Sulak and Danielsen, 1989). This is seen in context of the small grainsize of the coccoliths. The geometry of pore networks controls fluid flow and the accessibility of fluids to cover mineral surfaces, which will influence the fluid-rock interaction potential. Fluid migration and the accessibility of fluids to grain surfaces depend on the morphology and connectivity of both intra and inter granular pore networks (Olgaard and Gerald, 1993). The evolution of the morphology of pore connectivity in unfractured rocks affects not only fluid flow, but other

geological processes as dissolution, cementation, electrical conductivity, and weakening of seismic wave velocities. The connectivity of three grained junctions is highly considered because it probably controls the permeability (Brace, 1980). Permeability will additionally increase if there is connectivity between two pores. Such an increase will let fluid access a substantially larger fraction of minerals surfaces. High specific surface area allows an increase of fluid-rock interaction (Heggheim et al., 2005). Another petrophysical parameter which determine reservoir quality is capillary entry pressure.

Due to its high porosity, a chalk reservoir may accumulate excessive amounts of oil and gas. About 40% of the world`s oil is produced from chalk and carbonate rocks (Tanner et al., 1991). However, the low permeability and oil wet surfaces result in a challenging recovery of the hydrocarbons from chalk reservoirs. Chalk reservoirs have therefor great potential for IOR methods.

2.3 Fracture and fluid flow in chalk

Since chalk reservoirs have a combination of high porosity and rather low permeability, fractures and high permeable zones are of great importance concerning fluid flow. High intensity of fractures may create a spatially distinct, permeable zone (Michie et al., 2014). The main fluid flow will follow the easiest path of well-connected networks. To better understand reservoir fluid transfer and petrophysical properties, it is important to consider the details of a fault zone, and categorize the zones as barriers, conduits, or a combined conduit/barrier (Chester et al., 1993). Faultzones may have an intensely and a weakly deformed damage zone (Micarelli et al., 2006). This pattern of deformation is controlled by how lithologies deform (Agosta and Aydin, 2006) depending on its strength and texture like grain size, matrix and porosity. Matrix permeability may be further diminished by pore collapse due to increase in effective stress during depletion of the reservoir. This means that well production depends on a certain concentration of fractures to increase the effective permeability (Snow and Brownlee, 1989). The effective permeability in the Ekofisk field ranges between 1 to 100 mD (Sulak and Danielsen, 1989).

Most of the oil in chalk reservoirs is trapped in the matrix. When water is injected into a chalk reservoir, it may not necessarily flow into the matrix itself. Hence, it is important to understand how reservoir fractures change during flooding and how to fully utilize the injected water to mobilize oil from the matrix and create a more effective drainage. To maximize production, it

is also important to understand chemical interaction between fluids and rocks. Subsequent textural changes in the pore space will affect wettability and expulsion of oil from the reservoir (Zimmermann et al., 2015).

2.4 Detrital and authigenic minerals

Precipitation and deposition of chalk occurs normally in deep marine settings, distal to deltas and estuaries. Occurrence of detrital grains except calcite, are normally minor. Detrital clay minerals that are present, may alter during burial diagenesis. Examples may be smectites which evolve via intermediate stage to illite, and smectite-chlorites evolve towards chlorites (Fabricius, 2007). In other cases, one mineral may replace another. Because of the often distal location of deposition, further clastic input is absent, and the mentioned minerals are mostly introduced by aerial transport, like ash falls.

Alterations of minerals are influenced by organic matter, its molecular mass soluble and thermal maturation. Carbon dioxide and organic acids present in pore-water will influence pH and hence the solubility of clay minerals. On the contrary, organic matter also acts as a reducing agent when iron oxides are destabilized to produce Fe^{2+} and increases the alkalinity. This reaction stabilizes trioctahedral clays such as chamosite (Fabricius, 2003). The presence of hydrocarbons may prevent dissolution and reprecipitation of calcite for several reasons. One example is due to hydrocarbons contributing to elevated pore-pressures which relaxes the maximum stress acting at the contacts between silicates and chalk particles and thus prevent contact dissolution (Hancock, 1990) Another fact is that hydrocarbon saturation will leave no water in the pores for interaction with chalk (Hancock and Scholle, 1975). Hydrocarbons may adhere to the surface of silicates and prevent pressure dissolution of calcite and thus reduce cementation (Fabricius, 2003; Hjuler and Fabricius, 2009).

Other polymorphs of calcium carbonate are as previously mentioned aragonite and vaterite. Aragonite will transform to calcite within days depending on temperature, and vaterite is even less stable (Zhou and Zheng, 2001). When optimal conditions for precipitation are given, calcite will form mineral coatings that cement the existing grains or fill fractures. Certain conditions will be favourable for dissolution, and this removal of calcite can dramatically increase porosity and permeability of the rock, which over time may result in formation of caves.

Pyrite and sulphates may via microbial action grow as concretions in an environment rich in organic matter. Authigenic clays as kaolinite, illite and chlorite can precipitate directly from

aqueous solution. Even organisms may alter its own composition during burial diagenesis. For instance the diatoms, which may transform from amorphous colloidal silica, through intermediate stage, to microcrystalline quartz if temperature reaches 190 °C (Fabricius, 2007). Chert concretions may also form.

2.5 Cretaceous climate and deposition of chalk in Europe

Large volumes of chalk reservoirs were formed during the Cretaceous. A major hothouse on earth enabled vast quantities of coccolithophores and other calcium carbonate rich species to evolve and, increase abundance. The Cretaceous hothouse refers to a part of geological history that started in Albian and had the highest temperatures until Turonian, during the Upper Cretaceous. The source of the hothouse Earth had been initiated by the breakup of Pangea, prior to the Albanian. Plate tectonic forced seafloor spreading and opening of the Atlantic. Submarine volcanic carbon dioxide emissions were released and caused high atmospheric CO_2 concentrations (Haupt and Seidov, 2001). The eruption of large super-plumes was the primary source of volcanic carbondioxid that contributed to the extreme global temperature increases. Seawater temperatures during Cretaceous had low latitudinal temperature gradients (O'Brien et al., 2017). In polar areas, the temperature reached approximately 25 °C higher than present levels, whilst equatorial temperatures were only a few degrees warmer than present. The salinity and circulation were low and anaerobic conditions prevailed. A combination of several processes caused a dramatic increase in sealevel that flooded the interiors of most continents. Global warming was the main contributor and led to melting of all land-based ice. Supplementary activities were volume expansion of seawater caused by increased temperatures, displacement of water due to large igneous provinces that erupted, and seafloor elevation caused by plumes that did not erupt. A longterm sealevel rise was evident throughout the hothouse and reached about 200 m above present sealevel. This resulted in widespread epicontinental seas (Fig. 3). Increased seaways and longterm transgression created optimal condition for biological diversification, in high water temperatures, shallow seas with partly optimal light conditions, and clear water. The high abundance of marine organisms led to vast accumulation of carbonate deposits.

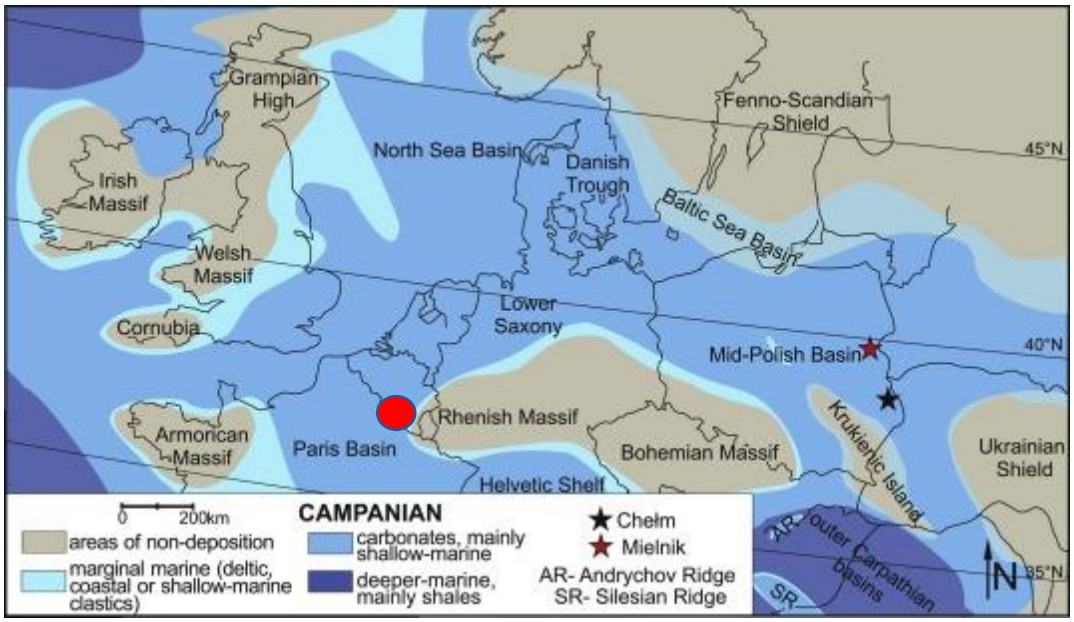

Fig. 3) European epicontinental seas during late Cretaceous created basins for accumulations for marine deposits. (Dubicka et al., 2018). Red circle indicates location of Mons Basin.

2.6 Mons Basin

The analogue chalk here used, originates from the Saint Vaast Formation deposited in the Mons Basin during the Upper Cretaceous. The Mons basin is located adjacent to the town of Mons in southern Belgium. There have been several shifts in sedimentation periods and deformation events which has formed the underground into major sedimentary and structural units. The basin may be considered as a gentle "syncline" developed on a folded and faulted Devonian-Carboniferous basement (Pirson et al., 2008). Early Cretaceous facies are locally covered by calcirudites, sandstones and conglomerates rich in glauconite and ferriferous illite. These Albian-Cenomanian deposits accumulate in local depressions where the subsidence rate is higher than in adjacent areas. These depressions, called "cuves", are distributed throughout the basin (Pirson et al., 2008). Glauconiferous marls followed by siliceous marls (Fig. 4) dominated the late Cenomanian and Turonian during a worldwide transgression. A thin bed of glauconitic sediments marks the lower, transgressive sequence of the chalk deposits from the Coniacian onwards in the Mons region.

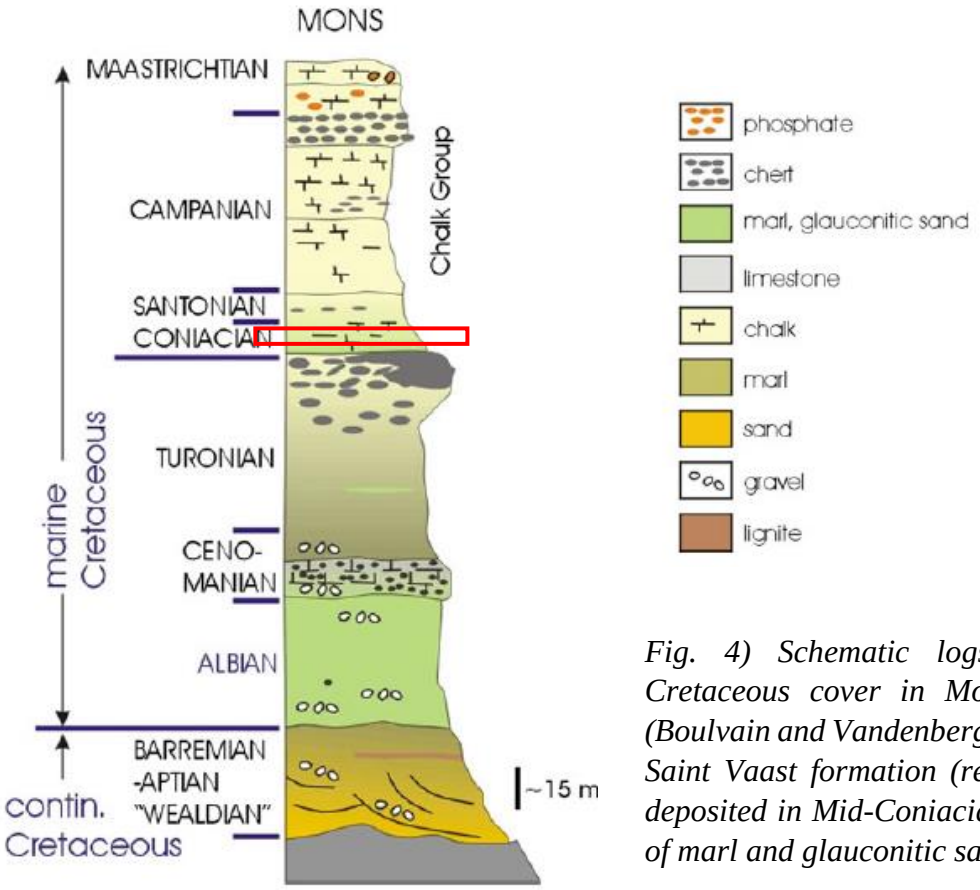

Fig. 4) Schematic logs of the Cretaceous cover in Mons Basin (Boulvain and Vandenberghe, 2018) Saint Vaast formation (red box) is deposited in Mid-Coniacian, on top of marl and glauconitic sand.

The Saint Vaast, Trivières, Obourg, Nouvelles and Spiennes formations are chalk sediments that were deposited in the Mons Basin simultaneously with normal faulting during late Cretaceous. After deposition of the Cretaceous and Cenozoic covers, the Mons Basin infill was exposed to the Variscan fold and thrust belt. This included two major tectonic units, the Brabant parauthocthon and the Ardenne allochthon. They are separated by the Midi-Eifel thrust fault and the Haine-Sambre-Meuse thrust sheets. The Ardenne allochthon is itself formed into major anticlines and synclines (Pirson et al., 2008). The uplift of Brabant Massif relative to the Campine Basin led to progressive erosion of the Maastrichtian and Campanian deposition (Dusar and Lagrou, 2007).

2.7 Analogue

Chalk from Obourg quarry within the Saint Vaast Formation in the Mons basin (OBSV) was chosen as analogue due to the accessibility of onshore chalk, compared to samples originating from reservoir fields as Ekofisk at the Norwegian Continental Shelf (NCS). When choosing an analogue, it is important that the sample has a similar or comparable composition in terms of

mineralogy and petrophysical properties. Same sedimentary age and environment at deposition is an advantage. Mons chalk has been collected from an outcrop in Belgium whereas Ekofisk chalk is deeply buried at 3000m depth (Fig. 5) and swept with hydrocarbons. They have common properties, yet there are dissimilarities as well. Burial depth is obviously one dissemblance and possibly calcite redistribution, since redistribution is linked to burial depth (Hjuler and Fabricius, 2009). Burial induced mineralogical changes may reduce specific surface area and cause permeability differences (Fabricius, 2003). The various diagenetic histories may influence test results and must be accounted for when implementing to reservoir conditions at Ekofisk.

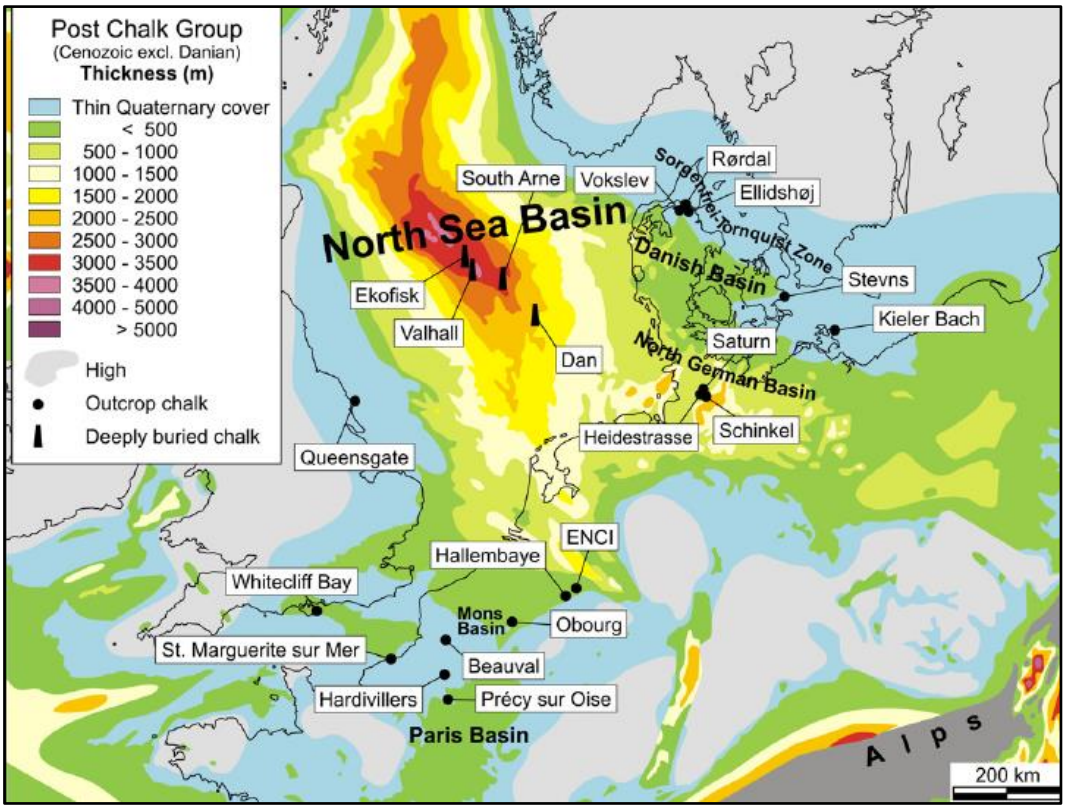

Fig. 5) European basins with variations in their respectively accumulated thickness. Ekofisk is deeply buried chalk with thickness ranging from 3000-3500m whilst Mons chalk has accumulated a maximum of 500m (Hjuler and Fabricius, 2009) modified by (Ziegler, 1990).

3. Previous flooding experiment

Three hollow cylinder tests on chalk cores were flooded by magnesium chloride ($MgCl_2$), sodium chloride (NaCl) and synthetic seawater (SSW). These three flow-through experiments were compared with two intact cores flooded by $MgCl_2$ and SSW at reservoir temperatures with 130°C. Composition of injected brines are listed App. A. The purpose of the experiment was to study how porewater chemistry influences the mechanical strength of a chalk core. Two mechanical tests were conducted; hydrostatic and creep. Effluent water was collected throughout the testing period. By analysing the presence of ions in the effluent water, one will be able to confirm whether the injected brine reacted with the rock or passed through the easiest path in the high permeable zone.

Every sample was flooded by NaCl during the first six days of the flooding experiment. The total number of flooding days exceeded 60 days. OBSV 9 (intact core flooded by SSW) was clogged and the experiment terminated after three weeks for this specific sample (Tab. 1). Properties of the tested cores were measured before and after the experiment. The cores had similar porosity with an average of 41,0% which reduced insignificantly by 0,24% during the flooding experiment. OBSV 6 ($MgCl_2$) was the only core that increased its porosity. The average increase in density was 0.03 g/cm^3. OBSV 9 on the contrary, showed a decrease in density (Tab. 1).

Tab.1) Porosity and density measures pre- and post-flooding.

Sample	Porosity %			Density g/cm^3		
	Pre-flooding	Post-flooding	Change	Pre-flooding	Post-flooding	Change
OBSV 9 Intact SSW	41.34	40.6	-0.74	2.69	2.67	-0.02
OBSV 6 Intact $MgCl_2$	40.81	41.86	1.05	2.68	2.72	0.04
OBSV 12 Fracture SSW	41.34	40.21	-1.13	2.7	2.74	0.04
OBSV 4 Fracture $MgCl_2$	40.49	40.37	-0.12	2.69	2.73	0.04
OBSV 18 Fracture NaCl	40.18					

The two cores flooded with SSW (OBSV 9 and OBSV 12) experienced the highest deformation rates. The intact core (OBSV 9) had a slightly higher value comparing the two (Figs. 8 and 9). Similar behaviours were observed for the cores flooded with $MgCl_2$ (OBSV 6 and OBSV 4). Hence, the intact core had a slightly higher deformation rate. OBSV 18 (NaCl) showed the least deformation.

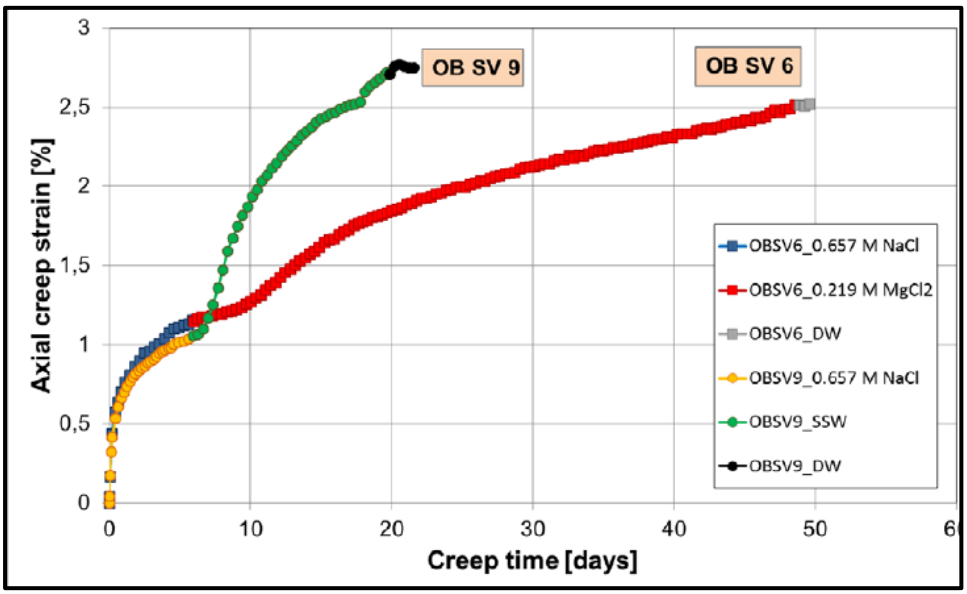

Fig. 6) Axial creep strain (%) plotted as a function of creep time (days). Comparison of two intact cores, OBSV 6 ($MgCl_2$) and OBSV 9 (SSW).

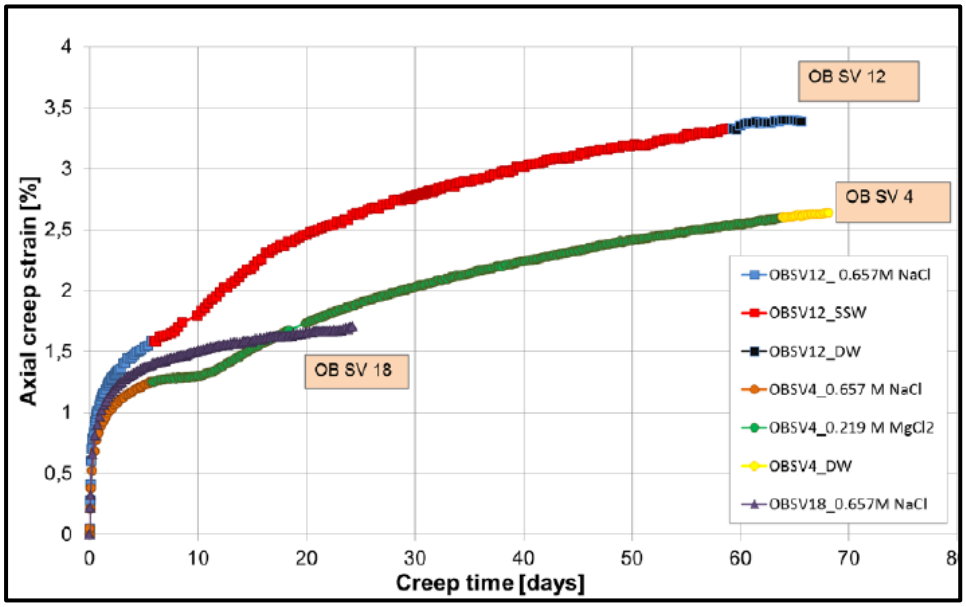

Fig. 7) Axial creep strain (%) plotted as a function of creep time (days). Comparison of three cores with hollow cylinder; OBSV 4 ($MgCl_2$), OBSV 12 (SSW) and OBSV 18(NaCl)

The reason for the increased deformation rate observed for the intact cores, was suggested to be a result of the core matrix being immediately in contact by the flooding brine. For the cores containing fractures, the brine would spend longer time to diffuse into the matrix and hence deform the chalk core. There was no significant difference in yield strength, yet the average

yield strength is slightly higher for intact cores. The experimental work showed that the fractures did not have a remarkable effect on the mechanical strength during hydrostatic loading.

Mineral exchange is reflected in the effluent water. Magnesium loss accompanied by calcium production was noted for all cores flooded with $MgCl_2$ and SSW (App. 2).

The cores were sliced (Fig. 8) and observed (OBSV 12) in the SEM. It was suggested that the location of precipitated minerals deposited in the center of the hollow cylinder.

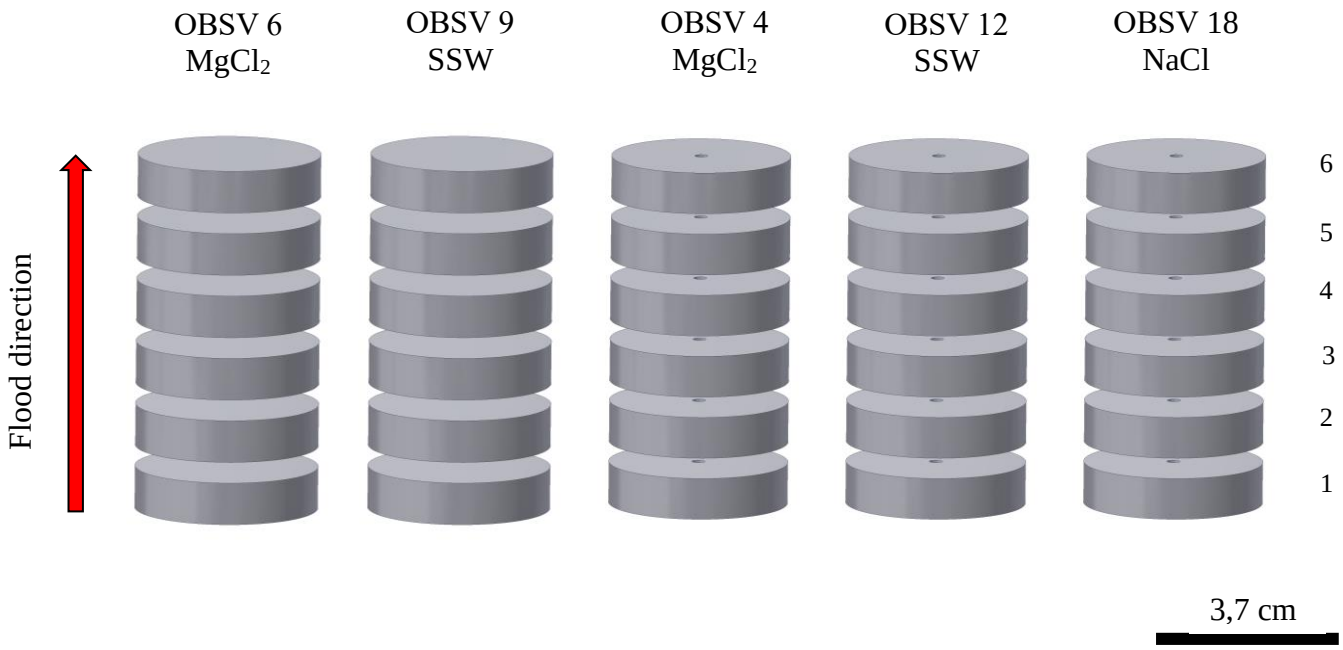

Fig. 8). Presentation of the five chalk samples summarizing the combination of the flooding brine relativ to hollow or intact core. OBSV 6 and OBSV 9 are intact, where as OBSV 4, OBSV 12 and OBSV 18 have the hollow cylinder. The red arrow demonstrate the flood direction in relation to slice number on the right side, hence number one is the inlet and six is the outlet.

4. Methodology

It was desirable to apply more than one single method to solve the issue presented in the definition of the thesis. Coinciding results will be amplified and more trustworthy by using several methods. One method will also complement the other. Methods which were applied during this study are:

- Optical Light Microscopy (OLM)
- Light microscopy (LM)
- Scanning electron microscopy (SEM) combined with energy dispersive spectrometry (EDS) and use of secondary and back-scattered detectors.
- X-Ray diffraction (XRD)
- Mineral liberation analysis (MLA)
- Focused ion beam (FIB-SEM)
- Transmission electron microscopy (TEM)

The OLM enhanced an overview of precipitated minerals along the inside wall of the hollow cylinder. It also eased the measuring of the various thicknesses of those minerals throughout the slices, from inlet to outlet. It enabled the study of color variations. The OLM was also a mandatory tool during preparation of samples.

The intention of preparing and studying thin-sections of these samples, was to identify petrographic characteristics as identifying gross mineral content and micro textural and structure variation. Optical properties as well as to classify the rock. This information was used to navigate extended studies on micron and nanoscale.

The intention of using XRD was to identify the presence of minerals in the cores with the hollow cylinder. The focus was to identify the surface minerals of the reprecipitated inside wall and to compare these with the unflooded rock samples.

Textural variation was imaged by using SEM, and EDS results provided a quantified list of elements present. MLA studies mapped those elements as an entire entity. TEM analysis could further image and identify chemically the new grown phases down to nano-scale.

Preparation of samples were aimed to the specific method and often in a series of steps. It is recognized that preparing chalk samples is a challenge due to high porosity and softness. For

that reason, a few samples of the same origin were prepared to evaluate the quality. It was performed with a specific aim to test if the central part of the precipitated material in OBSV 4 could be preserved while preparing. These unflooded chalk cores were sliced to similar sizes, mounted, and polished. Epoxy penetrated the core adequately and the result of these test cores was an optimal beginning for further preparation of actual samples.

4.1 Optical light microscopy (OLM)

The optical light microscope, Zeiss Stemi DV4, has a maximum of 20 times magnification. The light travels and reflects through the lens of the microscope.

4.2 Light microscope (LM)

The Zeiss Axio polarized light microscope uses visual light which travels through a system of lenses. The light microscope resolves particles down to 0.2 microns, as resolution is limited by the wavelength of visible light. The resolution uncertainties are related to factors like wavelength of the light source, specimen quality, or lens quality (Murphy and Davidson, 2013). An essential application of the light microscope is enhancing the contrasts by using polarized light (MacKenzie and Adams, 1994). Polarized light interacts with the crystal in a specific way which result in an image that ease the identifying of crystalline minerals in the specimen (Murphy and Davidson, 2013). This allows an improved contrast compared to OLM. AxioCam ERc 5s camera is attached and connected to a software and used for micrographs.

4.2.1 Sample preparation of LM

Six thinsections were produced, including the reference rock and one from each of the five cores flooded. The softness of the rock and the dry preparation method of chalk thinsections, complicated the process. As it is not possible to make a parallel cut with the machine after mounting and gluing to the glass, it is challenging to achieve an even thickness of the final thinsection. Two steps of dry grinding on coarse scale of 250 and 500 grits were processed before a final touch using 1000 grits combined with ethanol. A constant focus is to flatten thickness evenly, while it is important not to miss information and destroy the sample. The thinsections were occasionally checked under the microscope to ensure that the sample achieved an optimal thickness which is normally slightly thicker than standard thinsection of 30 microns. A final polish of 3 microns Diapro on Dac performed by Struers Roto Pol-35 increases the quality of the images.

4.3 X-Ray diffraction (XRD)

A D-8000 Bruker was available for study at the University of Stavanger. X-Ray diffraction provides information about the composition of the minerals (Emery and Robinson, 1993). Each crystal has a unique, specific structure. The properties of a mineral are linked to the arrangement of atoms in this crystal system. X-ray diffraction is a method which can yield the unique pattern associated with this crystal structure, by using Bragg`s law. The X-ray source produces a beam of known wavelengths. The sample is rotated until the incident angle is identical to the reflected one. This diffraction behaviour refers to the inversely proportional relationship between the X-ray angle of diffraction and the distance between the arrangement of atoms (Emery and Robinson, 1993). A constructive interference of diffracted X-ray beams occurs, and a reflection will be detected at this specific angle. Peak intensities give information about how much X-ray scattering contribute to the reflection and defines how much of a phase is present in the sample. An interpretation of these spectra will discriminate minerals with similar chemical composition (Emery and Robinson, 1993). The width of the peaks reflects the instrument´s analytical error. The uncertainty increases when the size of the grain decreases. A search by mineral name in the EVA V4.0 software, provides a match of X-ray diffraction patterns, and enables the phase identification of a large variety of crystalline samples.

4.3.1 Sample preparations

X-Ray Diffraction (XRD) Provides the mineralogical composition of bulk samples (about 1 g). Four samples were analysed by XRD method. This included three samples with the hollow cylinder and the reference rock. One gram of chalk from the reference rock was milled and placed in a holder and further compacted. A small amount of powder was scratched from the surface of the inside hollow cylinder and placed into a metal cavity mount holder (Fig. 9).

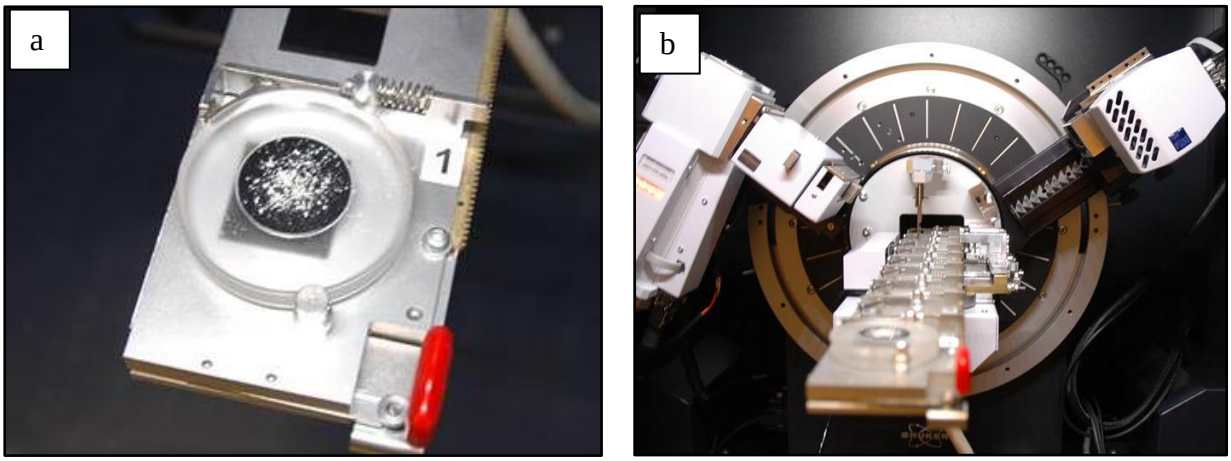

Fig. 9) Identification of the mineral composition by XRD. a) A sample has been prepared and placed on position 1. in the A D-8000 Bruker. b) The prepared sample was further located under the source of the X-ray.

4.4 Field emission gun Scanning electron microscopy (FEG-SEM)

A Zeiss Supra 35-VP FEG-SEM at the University of Stavanger (UiS) was available for investigation (Fig. 10). SEM is an electron microscope that produces images of a sample by scanning the interaction of electrons with the surface. The interaction of these electrons produces various signals that contain information about the sample`s surface topography and composition. The electron beam is scanned in a raster scan pattern, and the beam's position is combined with the detected signal to produce an image. The scanning of the image is created with a focused beam of electrons (Callister, 2007). The wavelength of electrons is smaller compared to light, resulting in a higher resolution compared to LM. By changing the coil, the lens can have variable focal length, providing a focus with high magnification. SEM may achieve a magnification of higher than 50.000 x (Callister, 2007). It has also got a great depth of field, because of the small apertures angle and long working distance. The lenses and specimen are in a vacuum chamber, to prevent electrons from being absorbed by air.

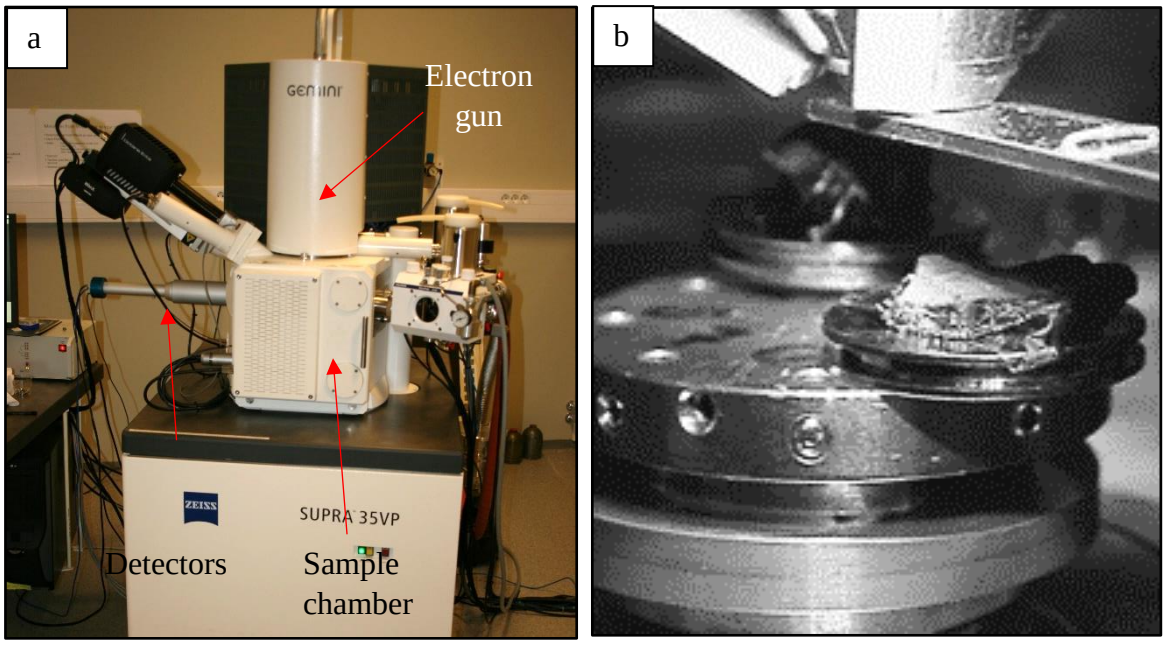

Fig. 10 a) Supra 35-VP FEG-SEM operating at the UIS. Images and spectra were collected with 15 kV acceleration voltage, 30-µm aperture and working distance ~ 10 mm. b) Two samples are inside the vacuum chamber, coated and covered with carbon tape to enhance connectivity.

Electrons are negatively charged, and the specimen needs to be electrically conductive to avoid charging. Samples are therefore coated with a conductive material like palladium, carbon or gold. Various energy signals reflect or produce from the surface when the beam hits the surface of the samples. These signals are collected by different detectors such as secondary electrons (SE), reflected or backscattered electrons (BSE), X-rays or energy dispersive system (EDS) and cathodoluminescence (CL), absorbed current (specimen current) and transmitted electrons. The main difference between the two detectors SE and BSE, is the type of scattering of the electrons they detect, inelastic and elastic, respectively. This allows the BSE to obtain information about features deeper beneath the surface and can therefore produce topographical image that differs from the one created by SE. SE on the contrary, detect inelastic scatter. This inelastic collision occurs when an atom is bombarded with primary electrons. Electrons in an existing atom may be excited and emitted from the sample as secondary electrons. Emission of these secondary electrons will vary as a function of the topography and composition of the sample surface, enabling an image of the surface (Hjelen, 1989). The beam of the electrons is collected and

displayed at the same scanning rate on a screen. The image on the screen represents the surface features of the specimen.

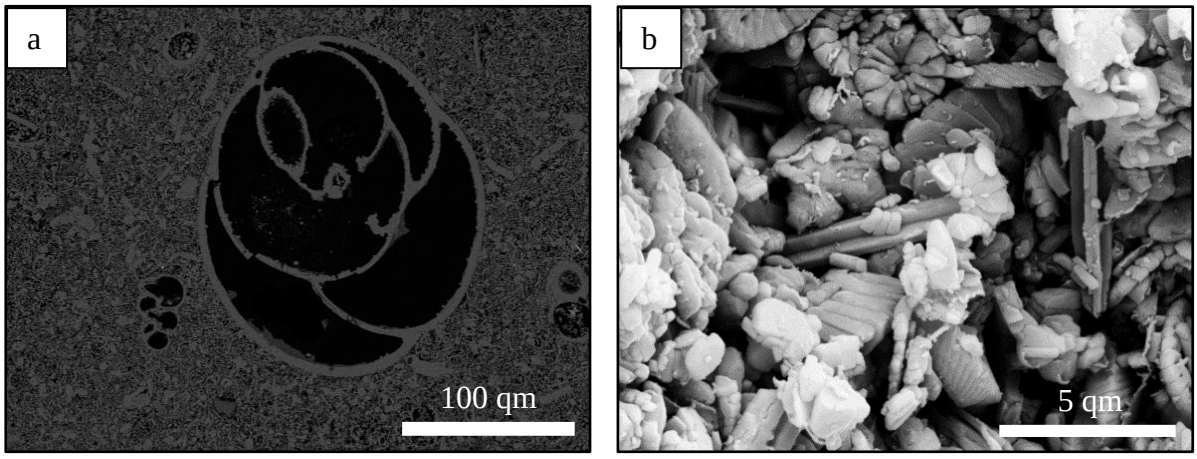

Fig. 11) Images achieved by two different detectors. a) An BSE image of a foraminifera which measured more than 100 microns. The mineral content may be disclosed by variation of the greyscale. b) The image is produced by the SE detector and produces a surface topography of the specimen, here with pieces of broken coccolithophores.

4.5 Energy Dispersive X-ray Spectroscopy (EDS)

Energy Dispersive X-ray Spectroscopy (EDS) analyses the chemical composition of a specimen by obtaining x-rays emitted from the specimen when the electron beam hits it. When the secondary electrons excite from their atom shells, the atom is stabilized by another electron from an outer shell which drop one, or several steps inwards. Since the outer shells achieved a higher state of energy in the first place, some energy is released in the form of an X-ray. The x-rays emitted from the specimen are characteristic in energy and wavelength, and allows the specific atoms to be recognized, based on the electron excited and its energy level. Elements with low atomic number have fewer peaks than higher atomic numbers, since they have fewer shells. The recognition of these characteristic X-rays enables a determination of the chemical composition of the element. The EDS-analysis quantifies the elements by calculating the area beneath the element peak and is given by weight per cent (wt.%) and atomic per cent (at. %) for each element. The accuracy may vary, and lighter elements such as carbon and oxygen are especially difficult to measure precisely. However, measurements without standardisation are only semi-quantitative and EDS are less prone to identify the precise and accurate concentration of an element.

4.5.1 Sample preparations

Samples with both fresh and polished surfaces were prepared with the intention to observe different properties of the samples. Preparation of polished samples is included in chapter of light microscope in form of thinsection and preparation of mounted samples is included in "sample preparation" in chapter of mineral liberation analysis (MLA). Samples are coated with palladium (Fig. 12) to prevent charging and to achieve a clear image in the SEM. Glovers are used not to contaminate samples and equipment.

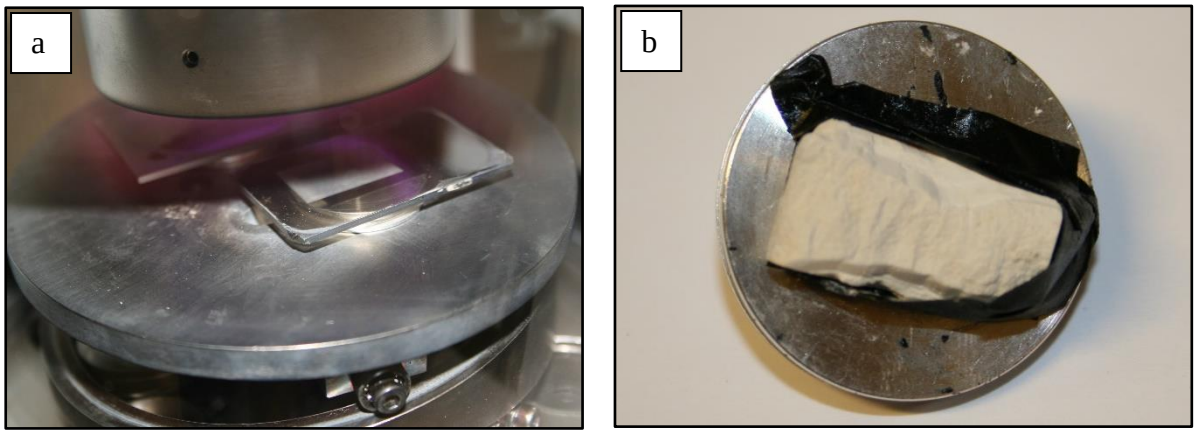

Fig. 12 a) Thinsections are coated with palladium. The thinsections rotate on the table inside a vacuumchamber. b) Preparing fresh sample for coating with palladium. The relatively flat sample is thoroughly attached to a sample holder before coating.

4.6 Mineral Liberation Analyzer (MLA)

A Mineral Liberation Analyzer (MLA) at the TU Bergakademie in Freiberg, provided a map of present minerals. The model is a FEI Quanta 600 F (Fig. 13). It is a scanning electron microscope (SEM) equipped with energy dispersive X-ray (EDX) spectrometers, and computer software that automates microscope operation. MLA measurements are based on backscattered electron (BSE) image analysis for determining grain boundaries on polished and coated specimen. It locates and classify the characteristic X-ray spectra of mineral species by comparing these to a library of reference spectra (Sylvester, 2012). The spectrum is further classified as a specific mineral or group of minerals, assigned a colour and saved in a database.

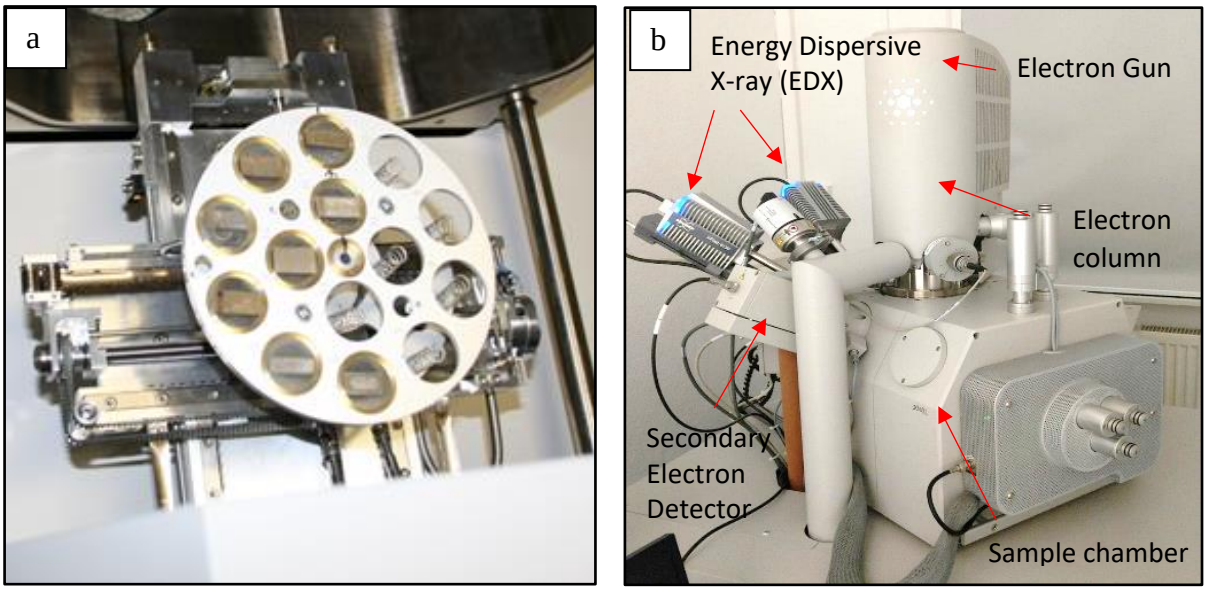

Fig. 13 a) The MLA in Freiberg has a sampleholder that may contain 14 mounted samples of 2,8 cm. in diameter which is placed in the vacuumchamber of the MLA. The OBSV samples are all placed in the same direction with centre core facing left, to keep track on location of processed results. b) The FEI quanta 600 F.

Standard greyscale is calibrated to copper and unique for each mineral. Bright greyscale reflects heavier minerals while the darker end of the greyscale represents lighter minerals. The average greyscale of the mineral in the BSE image is linked to a database of EDS-spectrum for comparison and hence produce a colour map based on the variation in greyscale of the BSE-image. The automatically operation of the MLA analysis, allows a high number of mineral grains to be examined and provide a statistically representative analysis of a sample. It is capable of distinguishing fine-grained and complex intergrown minerals down to micrometres scale (Sylvester, 2012). However, similar mineral compositions may be challenging to distinguish (e.g., hematite and magnetite) and the MLA is unable to distinguish polymorphs like calcite, aragonite and vaterite.

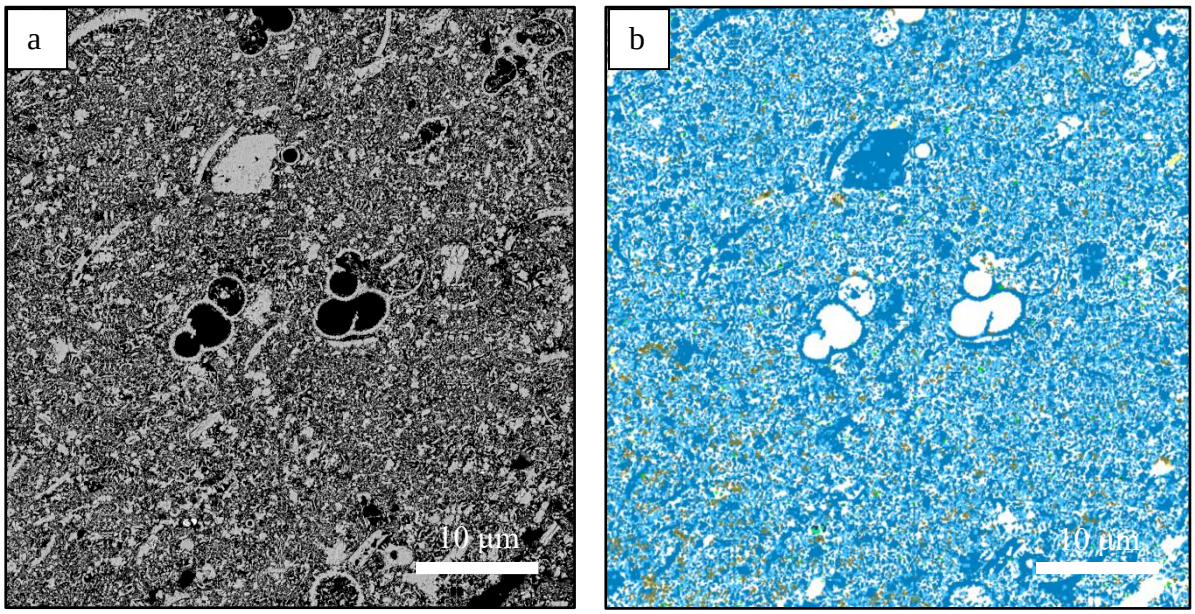

Fig. 14 a) An example of a greyscale BSE image of OBSV 12.2 flooded with SSW. b) Produced colourmap of distinguished minerals of the identical frame.

A SEM-generated electron beam scans the sample in a raster pattern, often called a frame, with a resolution depending on the magnification; increased magnification decreases the size of the frame (Krinsley and Doornkamp, 1973). 15 kV acceleration voltage was used during operating the MLA in Freiberg. The beam current was set to10 nA. The smallest particle size that can be identified and mapped by MLA software is 0,2 µm. Distinguishing minerals at these detailed level, challenges the recognition and spectral interferences. Prepared samples were placed in the vacuum chamber. The sample holder may approximately contain 14 small circular samples of 2,8cm diameters. Three different modes were available depending on the accuracy desired. A GXMAP, a software and a measurement method, was used for the purpose to discriminate the grain boundaries determined by the greyscale of the BSE image. A grid of about 450 squares were measured propagating in a specific pattern. The distance between each measured pixel was set to 0,4 microns, which is near the limit of the maximum level of resolution. Each spot was measured for 10 millisecond and threshold counts to 500 for spectrum recognition. Expected mineral-list was preloaded. This detailed and time-consuming analysis ran two samples overnight. Unknown minerals went through a new process of running spectral recognition before achieving a final map of mineral distribution.

4.6.1 Sample preparations

Chalk samples were mounted in epoxy in available labs at the University of Stavanger (Fig. 15). A pre-mounting test applied before mounting the current samples, showed proper preparation of nicely intact and polished surfaces. Unfortunately, the samples did not cast in epoxy as expected. Several samples had such a thin cover of epoxy, that it vanished immediately during dry grinding. This challenge appeared due to lower permeability of the flooded samples compared to non-flooded rocks. Some samples went through several steps of applying epoxy in a vacuum chamber. A nonpolished sampled would be denied in the MLA or leave sample areas without results. Similar height of samples is favorable, and must not exceed 7 mm. A final step of carbon coating to prevent charging was performed at the Bergakademie in Freiberg.

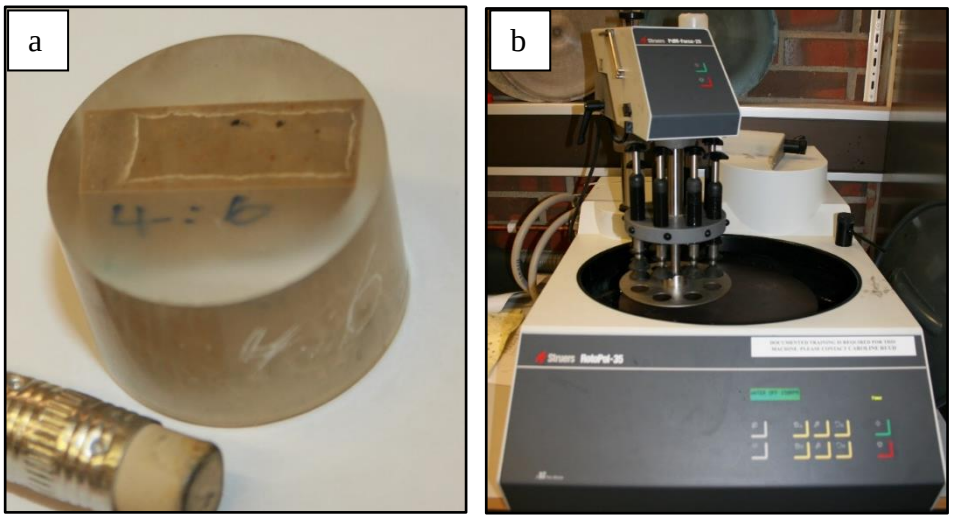

Fig. 15 a) A sample mounted in epoxy, dry grinded and prepared for a final polish. b) The Struers Rotopol-35 with Dac and 3 μm dispension was utilized for a final step of surface polish.

4.7 Focused Ion Beam (FIB)

Focused Ion Beam (FIB) is a method to prepare ultrathin samples of 100 nm for studies with Transmission Electron Microscopy (TEM). This preparation of the samples have been performed at a lab at NTNU and operated by Per Erik Vullum. The FIB used is a Helios G4 UX FEI instrument (Fig. 16) in combination with cryo-compatible accessories. A beam of focused ions removes material from the specimen surface. The FIB instrument is combined with a scanning electron microscope and allows a simultaneously monitoring of the process. When the beam of ionized gallium atoms is accelerated and focused onto the specimen surface, material is removed. The method of layer by layer removal, is called ion milling. The ion beam is generated by a gallium (Ga+) ion source (LMIS) at the top of the ion beam column (Rigort and Plitzko, 2015). Gallium allows an easier grinding process at lower temperatures and the source is kept in liquid phase during operation.

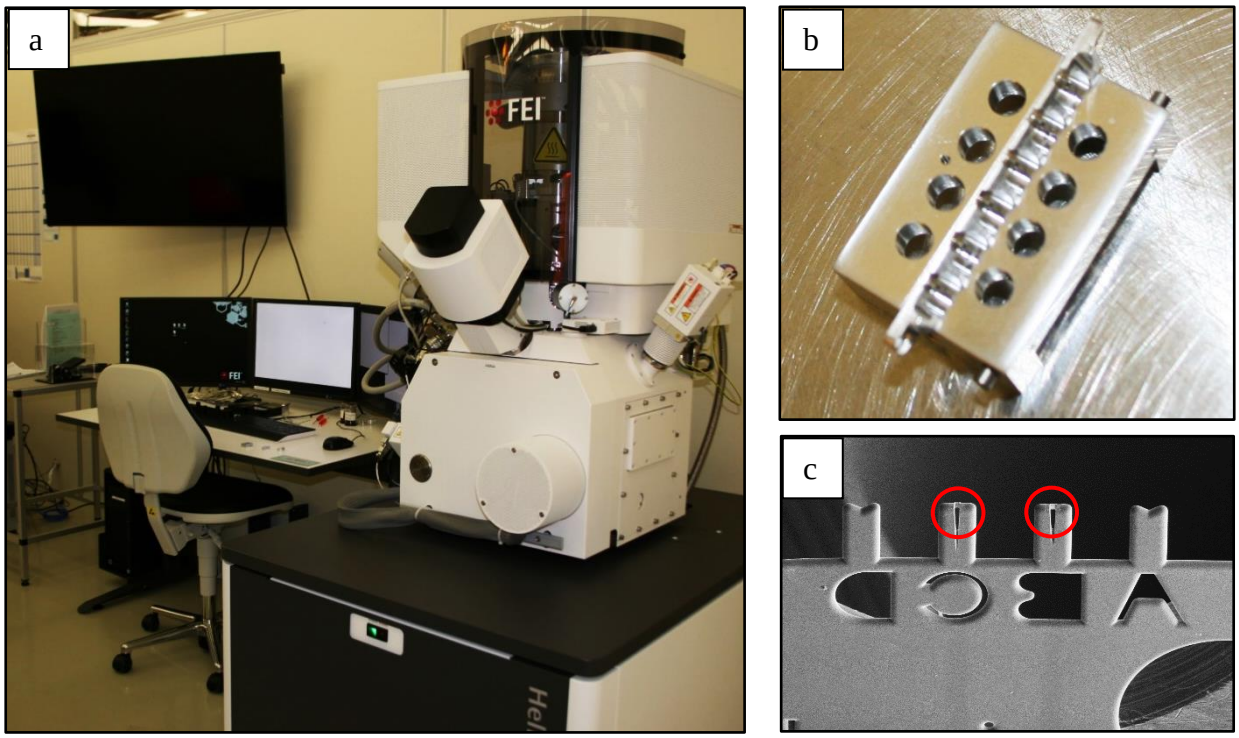

Fig. 16 a) The FIB model, Helios G4 UX, FEI at NTNU. b) An omniprobe holder. c) An omniprobe is a tiny copper plate that will preserve the final product. The sample was attached to the top of point B and C (red circles).

When high energy Gallium atoms are inserted onto the top few tens of nanometers of the surface, atoms will sputter and produce an amorph surface. The high level of energy will also transfer thermal energy to the specimen causing local heating and implantation of Ga-ions into a superficial layer of the specimen. These effects of the Gallium atoms depend on the

accelerating voltage, ion current, angle of incidence used for milling and the chemical composition of the target.

When high energy Gallium atoms are inserted onto the top few tens of nanometers of the surface, atoms will sputter and produce an amorph surface. The high level of energy will also transfer thermal energy to the specimen causing local heating and implantation of Ga-ions into a superficial layer of the specimen. These effects of the Gallium atoms depend on the accelerating voltage, ion current, angle of incidence used for milling and the chemical composition of the target.

The beam of gallium atoms forms a pool (Fig. 17 b) around a carbon cord which mark the top sample. One side is temporarily intact and referred to as “the bridge”. At this stage, the sample normally measure 14 x 14 x 2 micrometers. A sharp wolfram needle is attached to the carbon cord on top of the sample. Naphthalene, $C_{10}H_8$, diffuses into the chamber, and enhance the needle welding to the TEM sample. The bridge is sputtered and the TEM sample is carefully pulled out at a speed of 1 micron /sec when being close to the pool. While the TEM sample is still attached to the needle, an omniprobe holder is prepared. The omniprobe is a carrier for transportation adjusted to the microscopic TEM sample. It consists of copper (Cu) which is a relative soft material. A trace, matching the size of the TEM sample, is made by removal of copper material. It may then be inserted at a point close to B or C on the omniprobe and further attached by applying carbon. Application of carbon is performed under low levels of energy. By increasing the energy, the process turns into sputtering instead. The thickness of the TEM sample was around two microns when it was attached to the omniprobe. A final thickness of 100 nm was achieved by a time-consuming sputtering process. The process is performed in gradual steps, keeping a working distance at 4 mm so that the electron-beam ion beam hit the sample at the same location. The imaged turned brighter, which indicate an optimal thickness for further analysis.

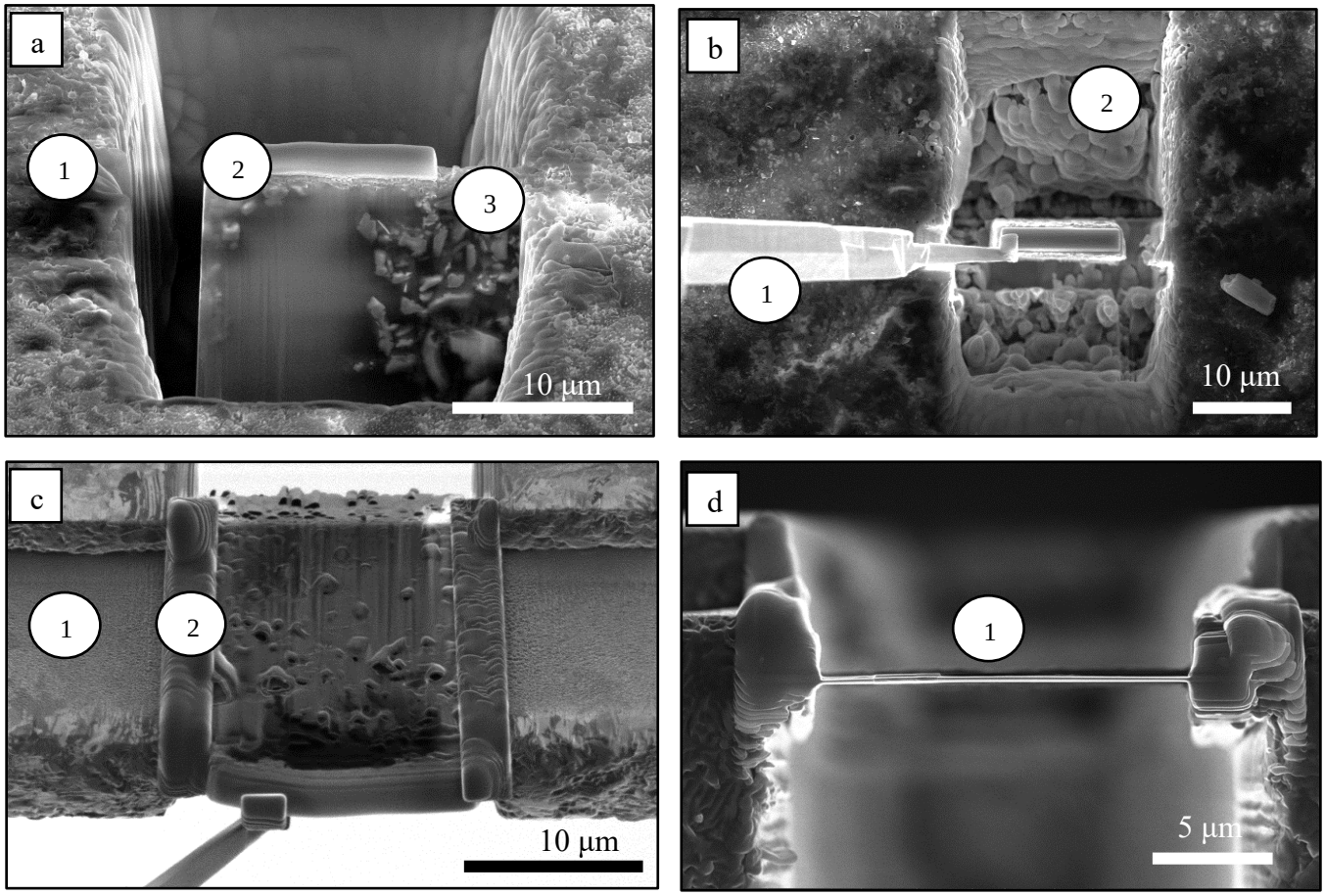

Fig. 17) There are several steps in the process of FIB preparation. a) A pool is formed around the TEM sample (1) by a beam of gallium atoms. The "bridge" (2) is left until a wolfram needle is attached and holds the TEM sample. b) The wolfram needle (1) transports the TEM sample to a sample-holder called omniprobe. FIB leaves an amorphous surface in the pool (2). c) Applied carbon (2) connects the TEM sample (3) to the omniprobe (1). d) The final sample has a thickness of 100 nm (1).

4.7.1 Sample preparations

Sample preparation for FIB-TEM analysis demand a mounted and polished surface as previously described. Samples were cut to a maximum height of 5 mm, and 4 cm width. Samples were further coated with 30 nm gold (Au) and covered by double-sided carbon tape to enhance electrical conductivity to create a steady image for a precise FIB operation. An elemental composition was collected before running the FIB procedures. Cleanroom procedures

at labs at NTNU were followed to prevent contamination. Shoes, clothes, glasses, gloves, and head cap were acquired at separate stations. Private items are not allowed into the cleanroom.

4.8 Transmission electron microscopy (TEM)

Transmission electron microscopy is performed at the University of Stavanger, with a JEM-2100 connected with an EDAX. The TEM may combine several measurement techniques. This electron microscope produces an image that is formed by the interaction of electrons with the sample as the ion beam passes through the specimen. Solid material will normally absorb electron beams. Since the FIB specimen prepared achieved a final thickness of only 100nm, it will allow partly transmission of the ion beam through the specimen. The transmitted beam is projected onto a fluorescent screen where the image may be viewed. Details of internal microstructures are observed, and a single column of atoms may be recognized. The electrons in a conventional transmission electron microscope have an energy of typically 100 keV. The electrons behave as Broglie waves which defines the limit to the resolution of the same order of magnitude at 0.2 to 0.4 nm (Hull and Bacon, 2011). The magnification may approach 1.000.000 x (Callister, 2007) Contrasts are imaged at low magnification due to the variation in the materials composition, followed by differential absorption of electrons. Additional modes of TEM allows observation in chemical variation, crystal orientation, and electronic structure.

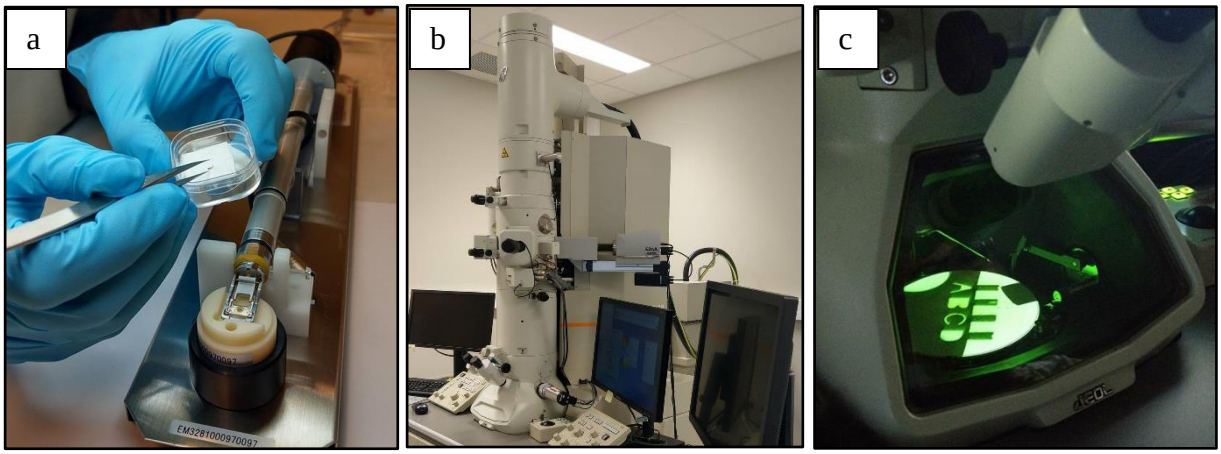

Fig. 18) Primarily, the TEM is prepared by refilling nitrogen for maintenance and to prevent contamination and Current is increasingly rising in several steps until it reaches 200 keV. a) A FIB-sample is loaded into a holder. b) The sample is inserted into the TEM. First zooming and then aligning at one specific particle. c) The magnification in one lens is adjuscted and a diffraction image is visible on the flurescence screen, instead of a regular microscopic image. (Photo: Siri Gloppen Gjersdal)

5. Results

5.1 Optical Light Microscope (OLM)

The different samples display colour variations. The flooded rocks have in general a dirtier appearance, with abundant gey and brown spots spread over the matrix`s surface, compared to the reference rock. Textural and structural differences were greater concerning cores with hollow cylinder. Every slice of OBSV 4 ($MgCl_2$) was recognized by a characteristic hollow circle defining the border between the original core and the reprecipitated new core (Fig. 19 f). Its matrix colour is relatively white in company with the surface of the reprecipitated minerals which also looks pure white (Fig. 19 e). The hollow cylinder has not completely been refilled with minerals for OBSV 4 (Fig. 19 e).

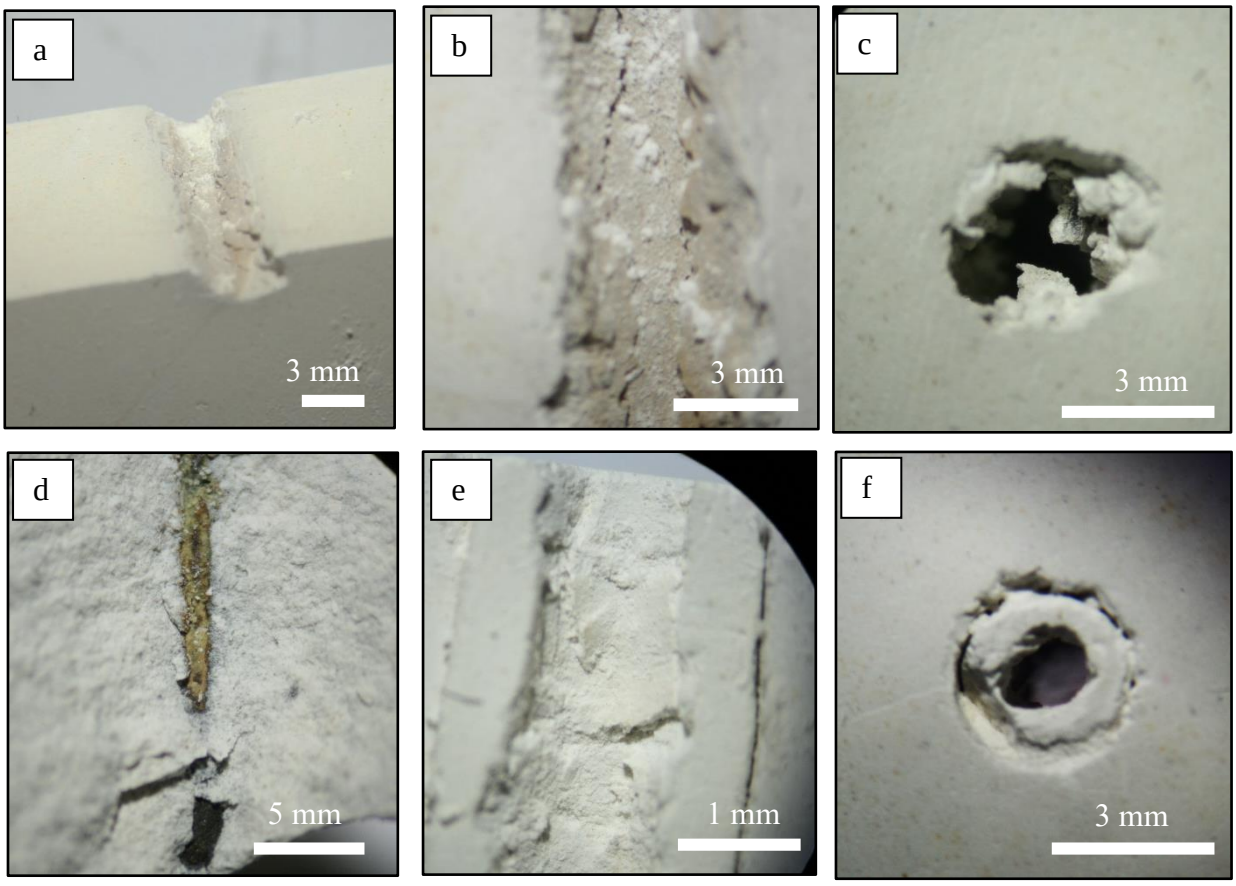

Fig. 19 a and b) OBSV 18.2 (NaCl) cut parallel to flood direction. Beige surface colour. c) OBSV 18.3 (NaCl) cut perpendicular to flooddirection. d) OBSV 12.3 (SSW) cut parallel to flooddirection has accumulation of brown and black minerals in centre. e) OBSV 4.7 ($MgCl_2$) is cut parallel to flood direction. f) OBSV 4.1($MgCl_2$) perpendicular to flooddirection.

OBSV 12 (SSW) showed a tendency of being almost completely refilled in the hollow part (Fig. 19 d). The border between original core and new minerals was not possible to detect. This core has a noticeable yellow-brow and black surface in the central part of the hollow cylinder. OBSV 18 (NaCl) had the most spacious cylinder left after flooding compared to OBSV 4 ($MgCl_2$) and OBSV 12 (SSW). OBSV 18 (NaCl) has a beige surface colour and additionally small brown spots in the matrix. The surface seems to have cracks or looks "platy".

An observation was made while preparing samples for FIB-TEM and thinsection. OBSV 4.5 ($MgCl_2$) was swept in epoxy and further sliced perpendicular to flood direction (Fig. 20 a). As previously mentioned, flooded cores tend to be only superficially penetrated by epoxy. However, OBSV 4.5 is more affected by epoxy adjacent to the hollow cylinder compared to the peripheral parts. The black circle is defining the border between the original core and the reprecipitated new core (Fig 19. e and f). When swept in epoxy, an inner white circle also appears (Fig. 20 b)

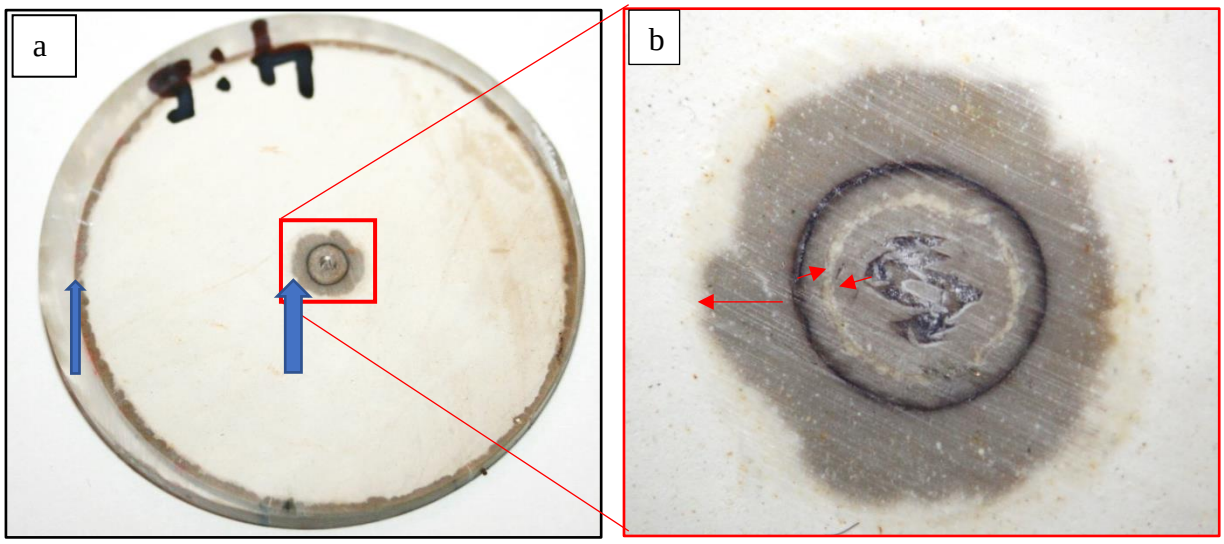

Fig. 20 a) OBSV 4.5 ($MgCl_2$) swept in epoxy and further sliced. Blue arrows highlight differences in depth of epoxy penetration during mounting. Area adjacent to hollow cylinder is deeply penetrated compared to the peripheral parts of the core. b) An OLM image displays a black circle of porous space, and an inner white circle tends to be less influenced by epoxy, hence an area of lower permeability. Red arrows mark the extension and direction of epoxy penetration.

The three cores with a hollow cylinder, OBSV 4 ($MgCl_2$), OBSV 12 (SSW) and OBSV18 (NaCl), showed tendency to refill the vacant space during flooding (Fig. 21). OBSV 18 (NaCl) has on average the lowest dimensions of reprecipitated minerals. OBSV 12 (SSW), has the highest capacity to refill the voids, hence the OBSV 4 ($MgCl_2$) achieved medium volume of the hollow space with reprecipitated minerals. The slice number also seem to affect the trend to reprecipitate minerals. It increases from inlet slice mid core, further it displays various behaviors depending on flooding brine.

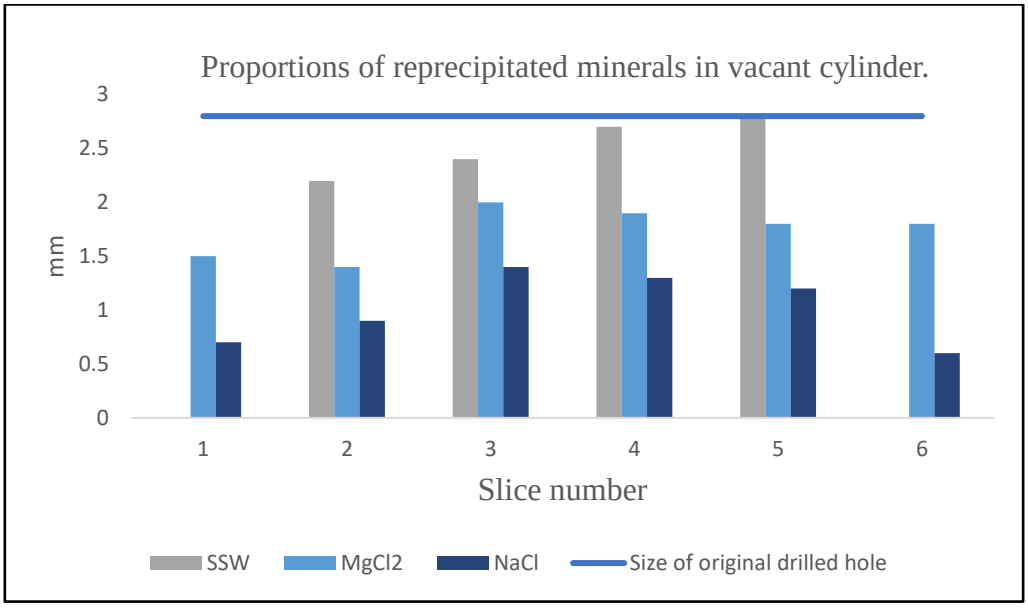

Fig. 21) The three cores with hollow cylinder have precipitated minerals in various dimensions depending on brine injected and the slice number. Blue horizonal line indicate the original cylinder size. OBSV 12 (SSW) achieves the highest proportion and is completely refilled by reprecipitation for slice 5.

5.2 Light Microscopy (LM)

The reference-rock appears homogenous and is defined as a mudrock (Dunham). Foraminifers, bivalves and other shell remains occur. Grains with high birefringence were recognized as mica, with size ranging from 5 to 40 µm. The euhedral shaped is likely to be mica (M) and possibly muscovite. The green subhedral grain is likely glauconite (G) (Fig. 22 a). The reference-rock also contains iron oxide. Darker grey accumulations tend to gather in porous

voids as inside the shell of foraminifers, or as dendritical forms in the matrix. These accumulations seem to be a result of epoxy penetrating higher porous zones, leaving a darker

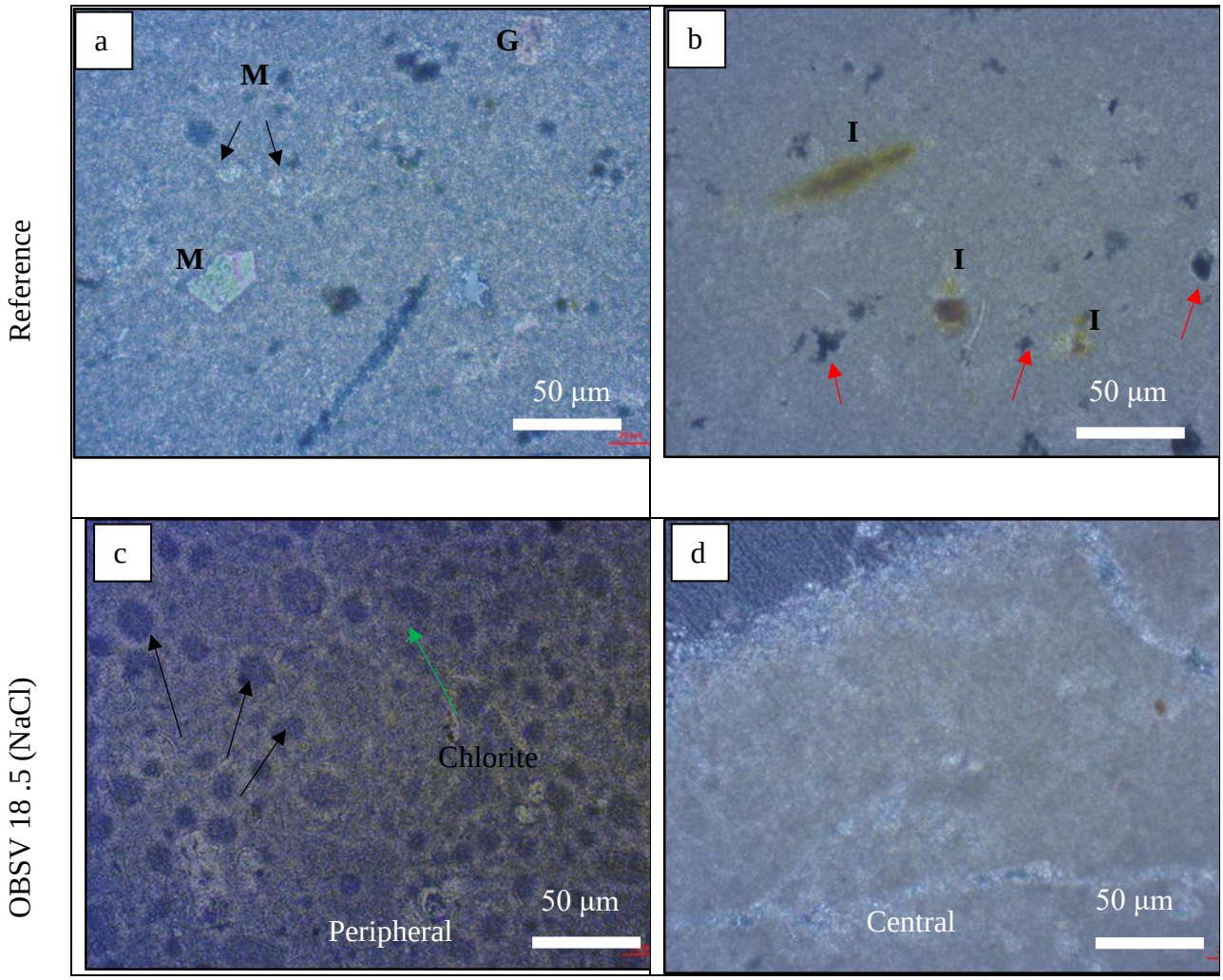

Fig. 22 a) The reference rock has traces of mica and glauconite. b) Brow spots are iron oxide. Dark grey accumulations are of epoxy in porous spaces. c) Chlorite is recognized. Black arrows highlight circular features. d) Homogeneous white in central part of OBSV 18.5 (NaCl).

colour without changing the composition of the rock. OBSV 18.5 (NaCl) tends to be clean, white, homogenous and highly porous in new precipitated minerals in the hollow cylinder area (Fig. 22 d). Shell remains are not observed in the central part. The limit of the resolution of the LM does not allow an observer to recognize whether this white appearance is coccoliths or calcite grains. The peripheral part of OBSV 18.5 (NaCl) has darker circular features with accumulation of chlorite around these (Fig. 22.c).

The intact core flooded with SSW (OBSV 9.6) tends to distribute abundant pyrite, black minerals of size less than one micron (Fig. 23 a). Shells of foraminifers are covered by darker grey epoxy. The same tendency of accumulating epoxy in weak grey dendritical forms occurs. Accumulations of iron-oxides in sizes ranging from a few microns to above 100 μm are distributed throughout the sample. They occur mainly in matrix as minor spots but may also cover porous spaces, typically covering fractures. OBSV 12 (SSW) appears to have a green background of chlorite coating in the peripheral part of the core (Fig. 23 b) This image has distribution of grey dots, larger than for the intact core. These are accumulations of epoxy in porous spaces. Single grains of mica and glauconite appears in sizes ranging from 2-4 μm. Pyrite occurs adjacent the hollow cylinder. OBSV 6.6 ($MgCl_2$) have same tendencies with euhedral black pyrite of approximately one micron. It has also the grey accumulations due to epoxy. Among abundant microfossils, iron-oxide occurs in peripheral parts of sample OBSV 4.5 ($MgCl_2$) (Fig. 23 d) Fractures in the original part of the core are visible as white stripes along the circular hole. The precipitated minerals adjacent the hole-wall distribute a pattern which is filled with dark grey colour from the epoxy which tends to accumulate in porous spaces. The pattern has typically lines that crosses one another (Fig. 23 d). The central part of the hole is still porous, and not completely covered by new minerals. Precipitated minerals have grown in elongated blocks that finally touched each other. The surface of each of these blocks are brown, but not possible to see in this image.

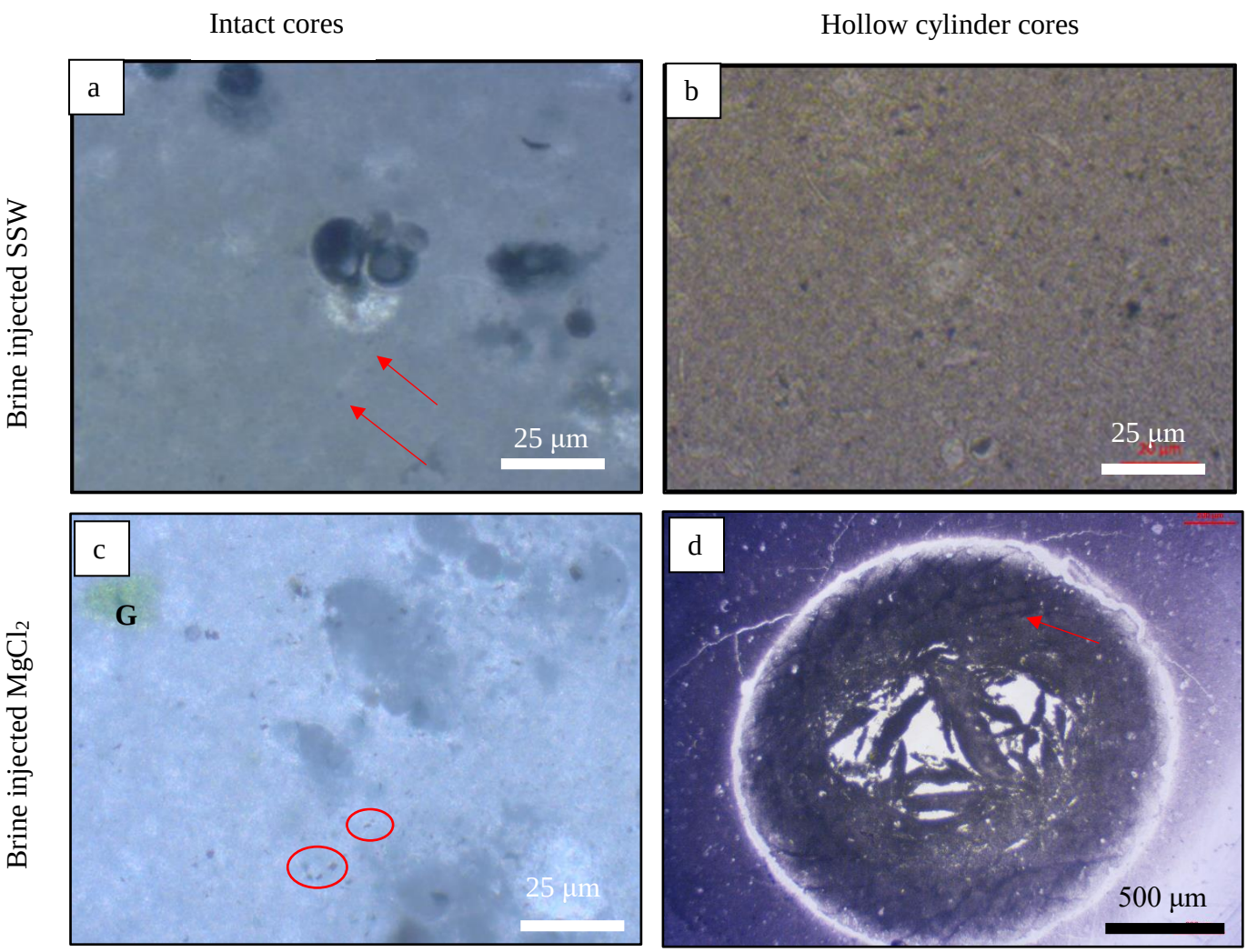

Fig. 23 a) OBSV 9.6 (SSW) Barely identifiable pyrite. Foraminifera coloured by epoxy. b) OBSV 12.5 (SSW) Chlorite and distribution of pyrite among larger grains of coloured epoxy. c) OBSV 6.6 ($MgCl_2$) Euhedral shaped grains are possibly pyrite (in red circles). d) Central part of OBSV 4.5 ($MgCl_2$) has a characteristic pattern (red arrow) in the central precipitated minerals of the previously hollow area.

5.3 X-Ray Diffraction (XRD)

Three hollow cores were subjected for XRD investigation, OBSV 18.1 (NaCl), OBSV 4.4 ($MgCl_2$) and OBSV 12.5 (SSW). A reference rock was measured with an intention to compare results (Fig. 24). One gram of milled chalk attained dominant peak intensities from X-ray scattering derived from calcite reflection. Low numbers of counts developed from muscovite and quartz.

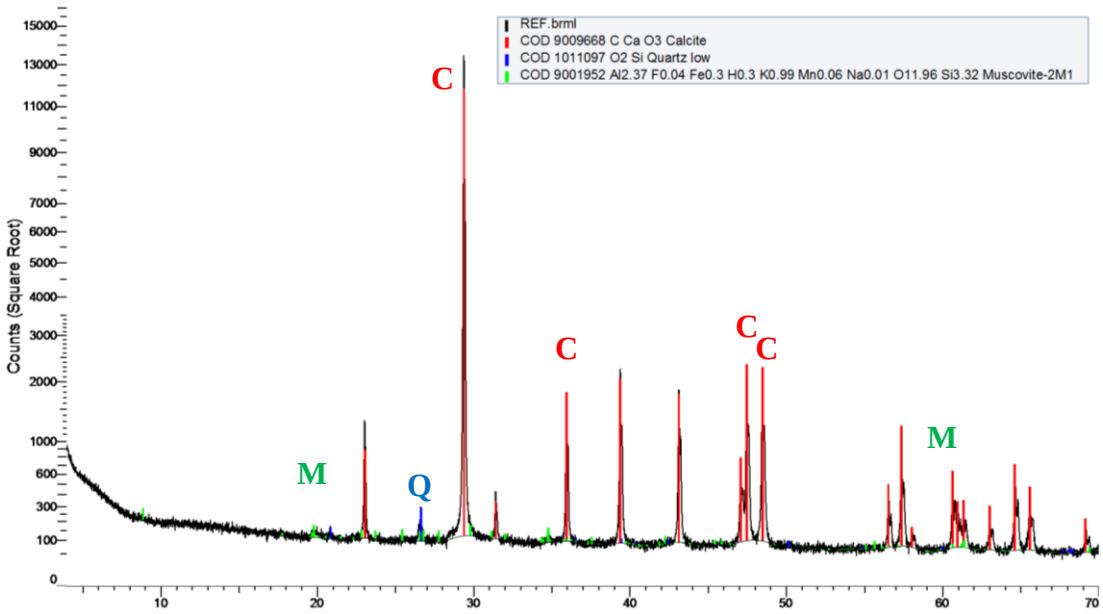

Fig. 24) X-Ray result of reference rock is dominated by calcite (red peaks). Minor traces of muscovite (green) and quartz (blue) occur.

Regarding the three remaining samples, grains from the surface of the inside hollow area were scratched out and collected on a plate. This causes unequal volume used for measurements and will not have comparable numbers of counts. The spectra and the relative number of counts is evaluated. OBSV 18.1 (NaCl) has the highest peak in the calcite spectra (Fig. 25 a). OBSV 12.5 (SSW) contains two different calcite spectra of two discrete lattice system, hexagonal and rhombohedral (Fig. 25 b). OBSV 4.4 ($MgCl_2$) shows a significant peak for magnesite and obtain a less prominent calcite peak (Fig. 25 c) with minor counts for muscovite.

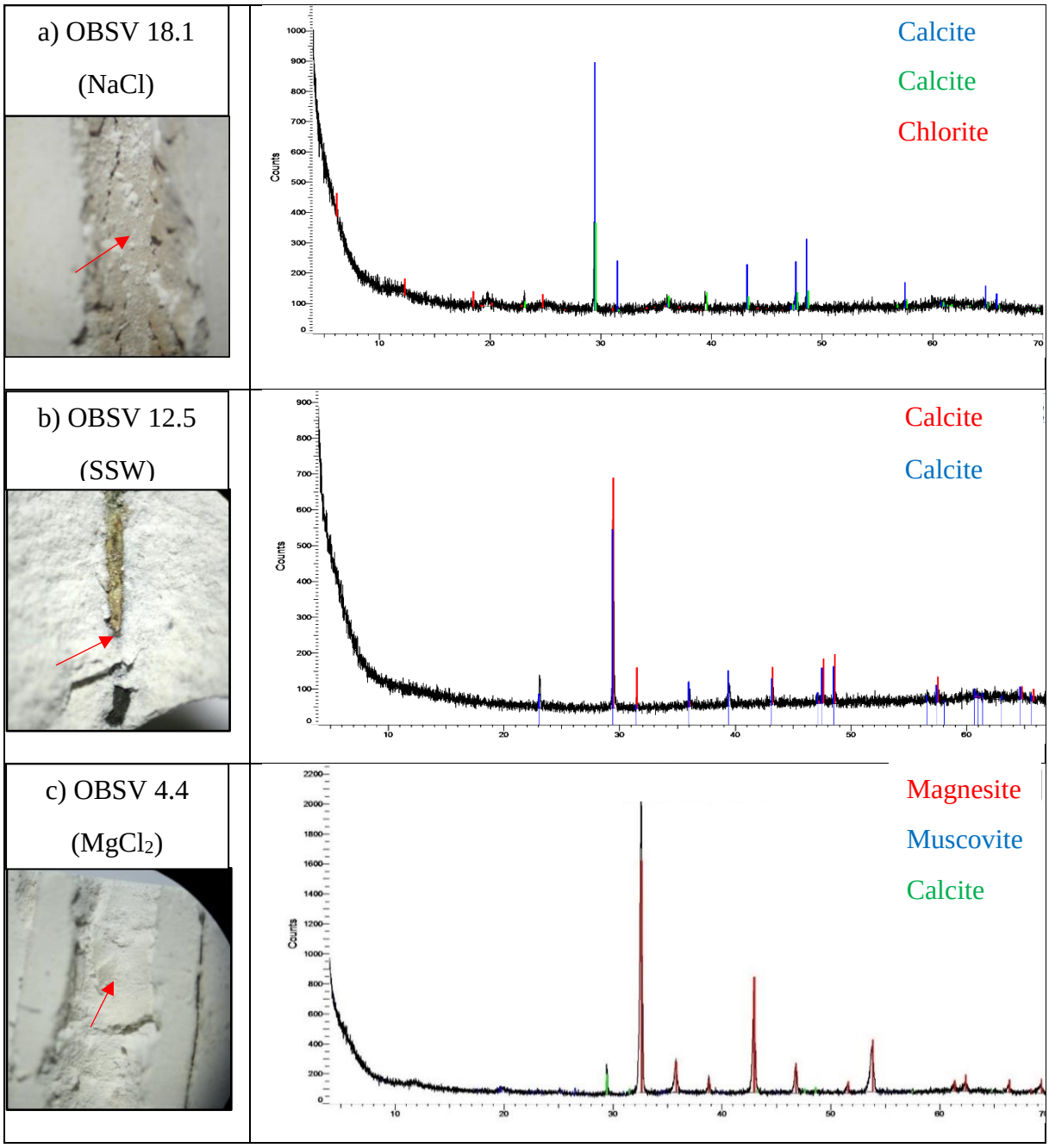

Fig. 25 a) OBSV 18.1(NaCl) is dominated by calcite spectra. b) OBSV 12.5 (SSW) has counts for two calcite polymorphs. c) OBSV 4.4 ($MgCl_2$) counts magnesite most frequently. Calcite seems to be less abundant as is muscovite. Red arrows points to the location from where the sample is extracted.

5.4 FEG-SEM combined with dispersive spectrometry (EDS)

5.4.1 SEM micrographs and textural variations.

Fresh samples were studied with the SE2 detector to identify textural variations compared to a reference rock (Fig. 26 and 27). The unflooded reference rock displays abundant degraded coccoliths, coccolith spine, parts of calciferous organisms like foraminifera, nannoliths, and occurrence of subhedral grains randomly distributed (Fig 26). The reference rock and OBSV 6.1 (MgCl2) as well as OBSV 9.3 (SSW) display similar characteristics at low magnification at 5.000 x (Fig. 26, a, c and e). With increasing the magnification to 20.000 x, OBSV 6.1 ($MgCl_2$) still holds the same characteristics as the reference rock (Fig. 26 b, d and f). However, on this magnification, it is possible to detect small (0,25 μm) elongated crystals in between coccoliths remains for OBSV 9.3 (Fig. 26 f). This may point to precipitation of phyllosilicates. The observation of precipitated minerals in the three hollow cores, shows more textural variations easy to recognize compared to the intact cores (Fig. 27). On a low magnification (Fig. 27, a, c and e|), the surface is dominated by homogeneous grains and coccoliths are less abundant compared to the reference core. A micrograph obtained with increased magnification of the same cores (Fig. 27, b, d and f), images differently shaped grains than compared to low magnification images. OBSV 18.1 (NaCl) (Fig. 27 b) contains euhedral, sheet like grains, while OBSV 12.3 (SSW) (Fig. 27 d) and OBSV 4.3 ($MgCl_2$) (Fig. 27 f) are dominated by cubic phases, however the surfaces of numerous crystals in OBSV 4.3 ($MgCl_2$) show softer edges compared to minerals in OBSV 12.3 (SSW).

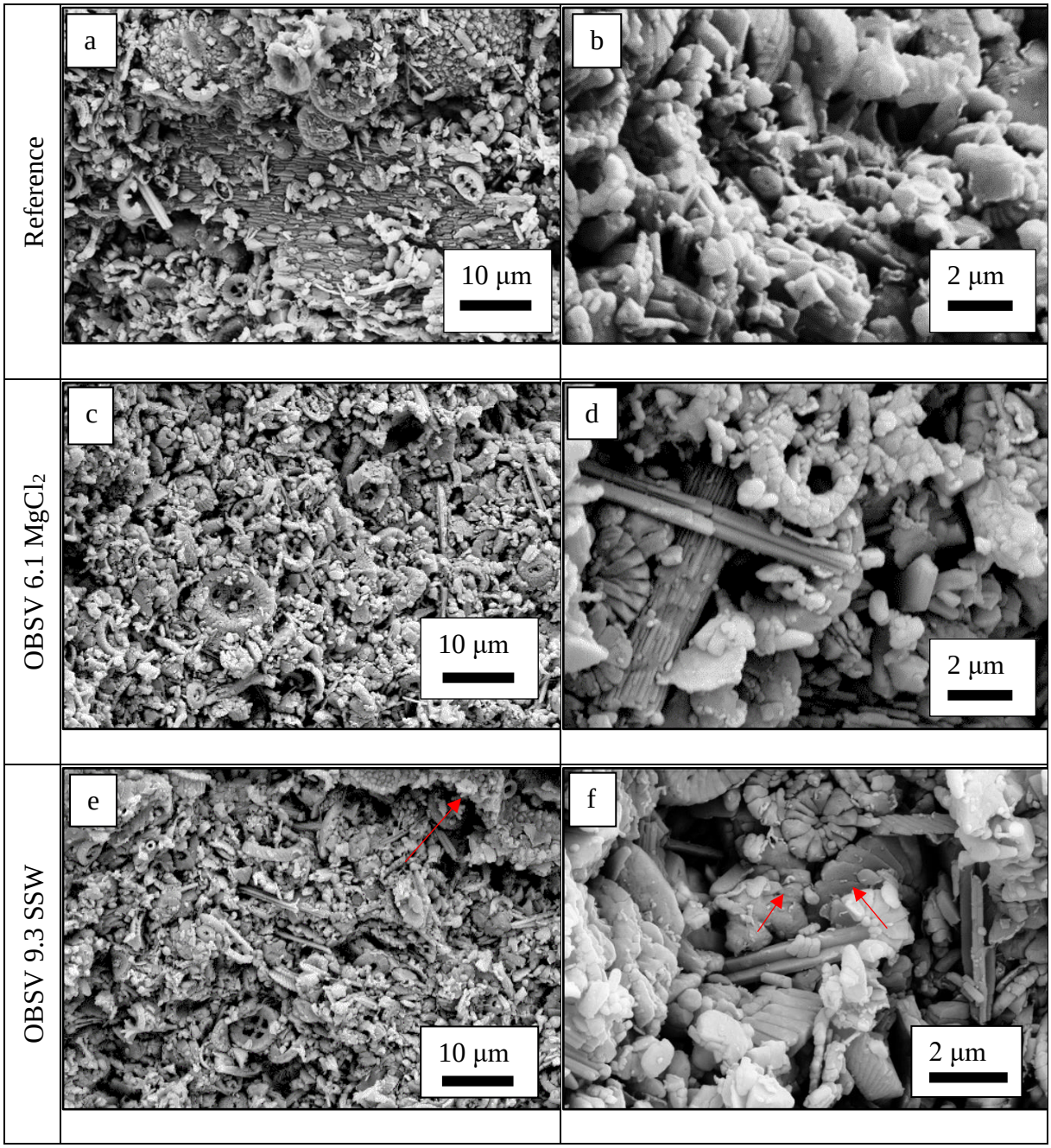

Fig. 26 a) REF rock. Remain of a microorganism which measures approximately 50 µm. b) REF rock. Abundant coccolith rings. c) OBSV 6.1 ($MgCl_2$) Abundance of coccoliths. d) OBSV 6.1 ($MgCl_2$) Coccoliths and possible nannoliths. e) OBSV 9.3 (SSW) Remains of microorganism. f) OBSV 9.3 (SSW). Small elongated white crystals are indicated by red arrows. They are likely to be phyllosilicates.

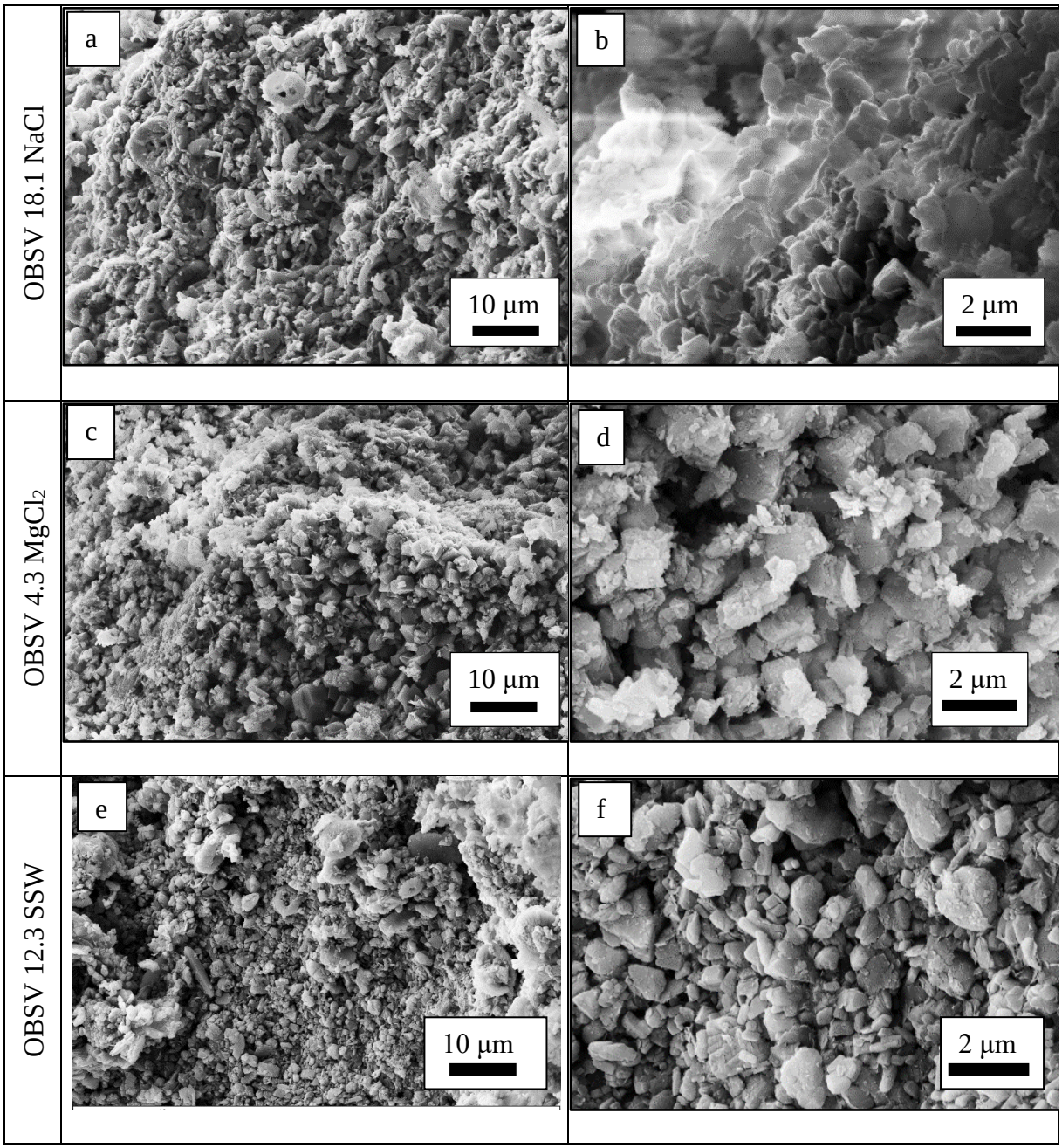

Fig. 27 a) OBSV 18.1 (NaCl) Low abundance of coccoliths on 5.000 x. b) OBSV 18.1 (NaCl) High magnification images, 20.000 x provides sheet like grains. c) OBSV 4.3 ($MgCl_2$) Coccoliths are not recognized. (d) OBSV 4.3 ($MgCl_2$) Cubic and euhedral shaped grains. e) OBSV 12.3 (SSW) Sub-rounded grains are more abundant than coccoliths. f) OBSV 12.3 (SSW) The surface is mainly dominated by cubic and sub-rounded grains.

A variety of elemental components were detected by utilizing EDS on SE2 images. The high resolution of the SEM allows a detailed observation of the grains` texture, shape and size and the EDS a semi-quantitative determination of the chemical composition (Fig. 28). Among the

identified minerals, calcite was naturally the most abundant. Pure calcite ($CaCO_3$) was rarely detected and was often contaminated by other elements, most frequently by Si. This contamination is related to the matrix but is especially relevant to the surface area of the hollow cylinder cores. Coccoliths were occasionally covered by coating of possibly chlorite (Fig. 28 a) The surrounding content of $CaCO_3$ emits X-rays and may therefore be mixed with interaction from a thin cover of coating.

OBSV 12.3 (SSW)

Element	Weight %
O	44.12
Ca	36.01
C	12.27
Al	2.43
Si	1.97
Mg	1.72
Cl	1.49

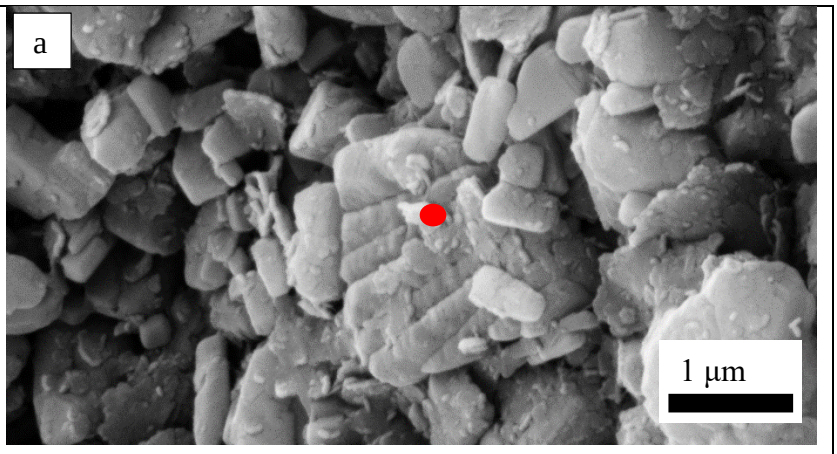

OBSV 12.1 (SSW)

Element	Weight %
O	5.51
Ca	78.98
C	0.40
Al	0.36
Si	0.02
Mg	0.05
S	0.03
Cl	0.03
K	2.53
Ti	0.76
Fe	11.34

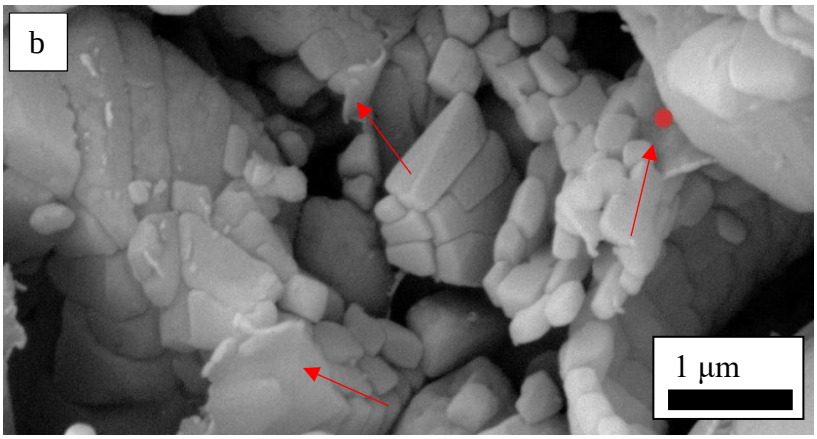

Fig. 28 a) A coccolith remain in OBSV 12.3 (SSW) appears to be coated. EDS on red spot indicate a mix of $CaCO_3$ and possibly chlorite. b) Sheet-shaped iron rich mineral is observed in OBSV 12.1 (SSW) marked by the red arrows.

Besides detrital quartz in OBSV 9.3 (SSW) (Fig. 29 a), possible precipitated ilmenite and magnesite in OBSV 4.3 ($MgCl_2$) (Figs. 29 a and b) were among detected non-carbonate minerals.

OBSV 9.3 (SSW)

Element	Weight%	Weight%
C	10,2	9,61
O	24,94	16,42
Ca	7,9	13,11
Al	0,09	0,03
Fe	6,21	7,21
Si	41,72	43,11
Cl	2,35	2,16
K	6,48	7,30
Ti	0	0,97
S	0	0,08

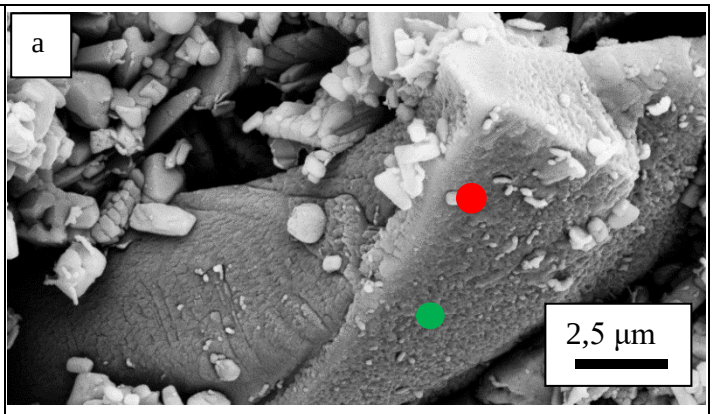

OBSV 4.3 ($MgCl_2$)

Element	Weight%	Weigh%
C	2,07	0
O	18,89	1.64
Mg	4,52	0
K	6,22	0.91
Ca	6,30	12.3
Ti	9,81	10.23
Fe	52,18	75.1

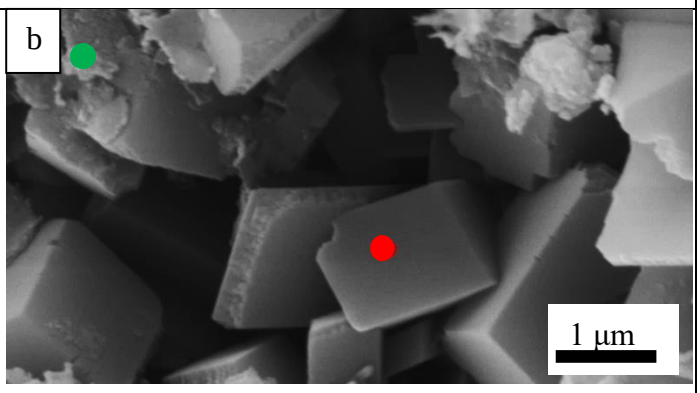

OBSV 4.3 ($MgCl_2$)

Element	Weight%	Weigh%
C	8.95	7.6
O	35.38	35.73
Mg	37.84	44.03
Ca	8.39	4.05
Al	0.58	0
Si	7.29	2.64
Cl	1.57	0.42

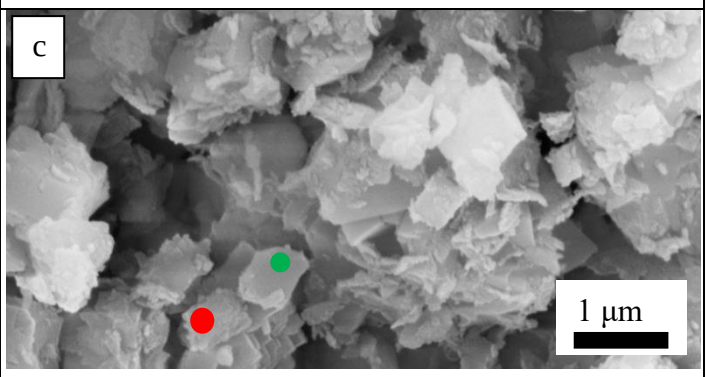

Fig. 29) Results of measurements by SEM-EDS. a) Detrital quartz (SiO_4) with mixed spectra, a grain with spectra of both quartz and clay mineral in OBSV 9 (SSW). b) Possible authigenic ilmenite ($FeTiO_3$) with mixed spectra in OBSV 4.3 ($MgCl_2$). c) Magnesite ($MgCO_3$) was also detected in OBSV 4.3.

5.4.2 Results from FEG-BSE (back scatter electron microscopy) and EDS

The greyscale allows an identification of minerals that have distinct elemental composition compared to calcite. A needle shaped grain, possibly pyrite, is distinct from the grey calcite,

because of a resulting bright appearance caused by higher energetic electrons of heavier elements (Fig. 30).

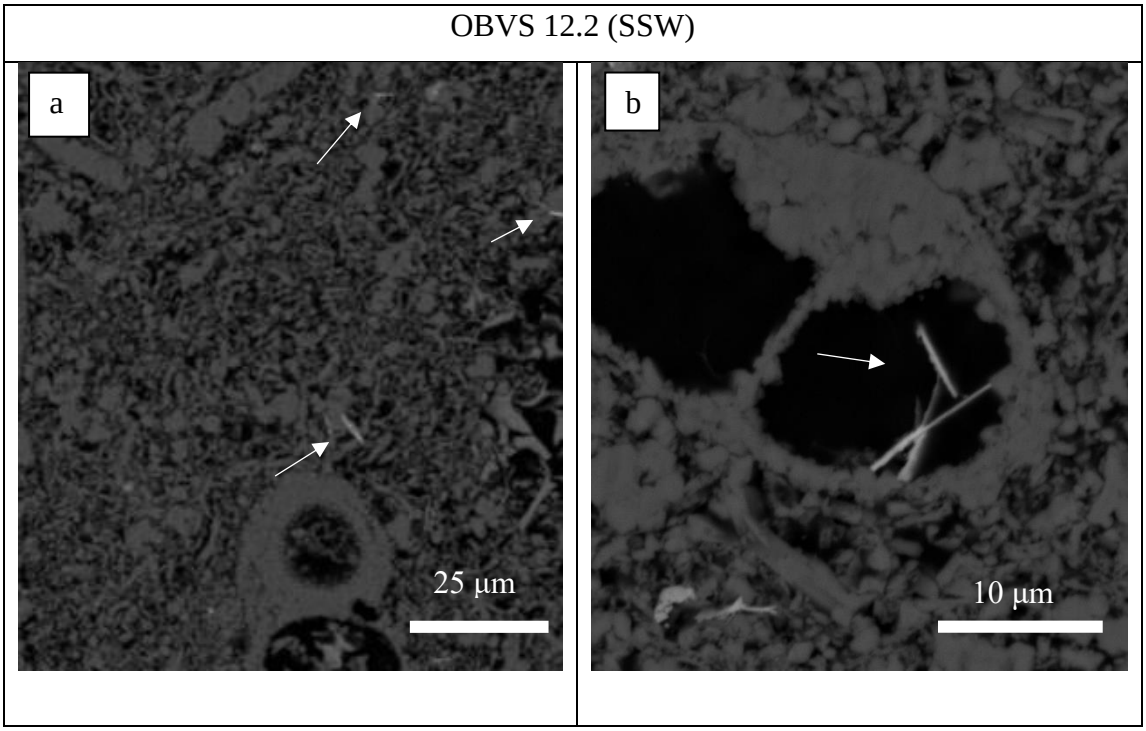

Fig. 30) Possible needle shaped pyrite tends to discrete from the calcite background due to the bright appearance. Pyrite is not possible to detect by EDS as it is too thin. a) Pyrite is precipitated in the matrix. b) Pyrite precipitates in porous space inside foraminifers.

The distribution of elements was mapped by using the EDS detector on BSE images for several samples. A distribution of calcium and magnesium near the hollow cylinder displayed uneven accumulation of those elements in the inlet slice of sample OBSV 4.1 ($MgCl_2$) (Fig. 31). Calcium is barely observed in the precipitated area inside the hollow cylinder. Magnesium is most abundant in the precipitated area, but it also occurs in the matrix. Magnesium tends to have higher accumulation in areas closer to the boarder and fades out towards peripheral parts. Silicon is abundant in the hollow part but also occurs in the adjacent areas. The remaining elements were evenly distributed. The two white lines limits an area adjacent the hole, a ”flushed zone” which tends to have a higher accumulation of Si.

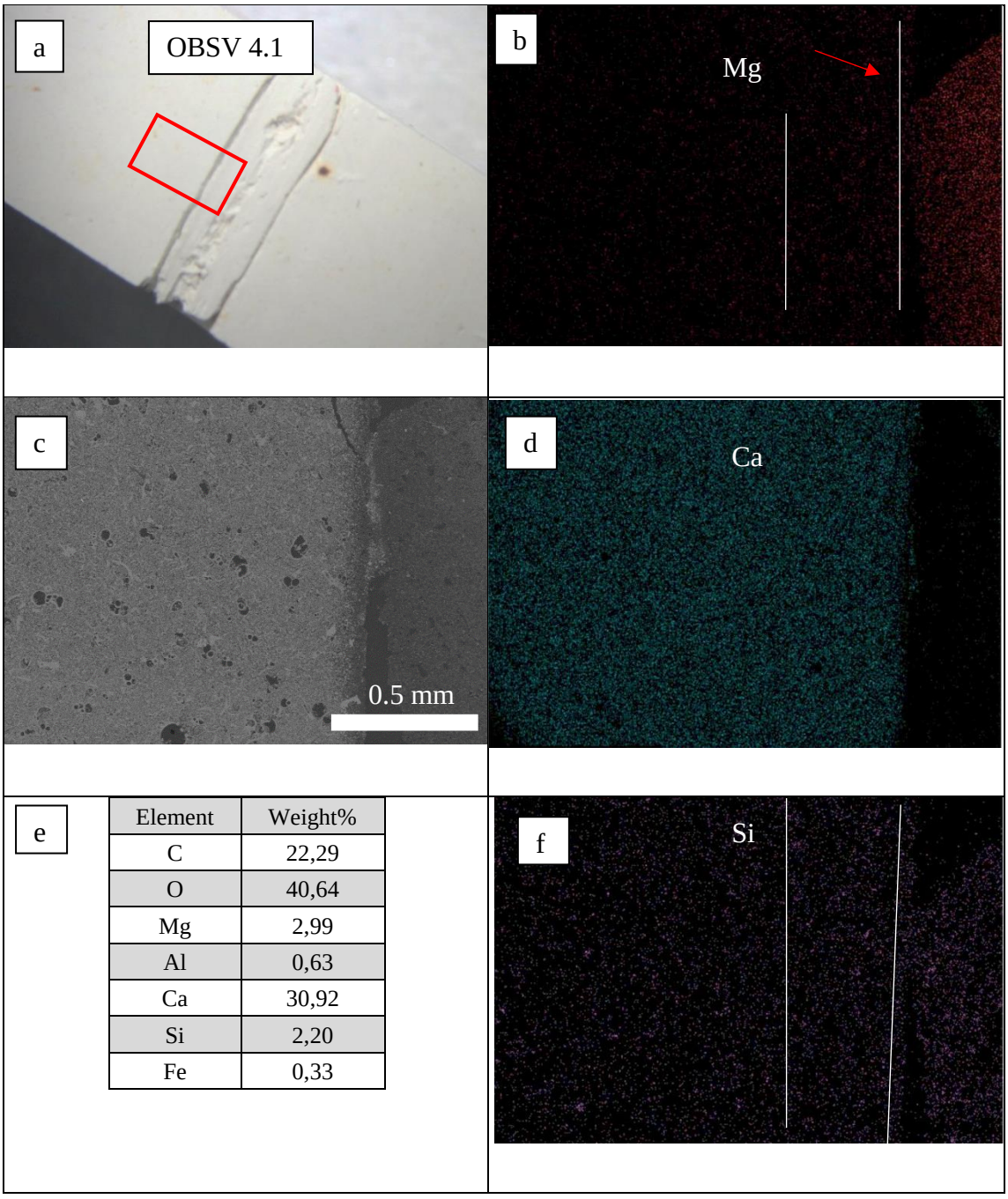

Element	Weight%
C	22,29
O	40,64
Mg	2,99
Al	0,63
Ca	30,92
Si	2,20
Fe	0,33

Fig. 31) Elemental mapping of OBSV 4.1 ($MgCl_2$) at the boarder of the hollow cylinder. a) Location of mapping area is marked by a red rectangle at an identical sample. b) Distribution of magnesium. The highest accumulation is in the precipitated central are but has also a high accumulation in the limited area between the two white lines. c) SEM image of the sample. The dark area is the open space between the core and the precipitated mineral in the hollow area. d) The extent of calcium is mainly limited to the matrix of the core. e) Table of elements and semi-quantification. f) Accumulation of silicon is slightly elevated adjacent boundary at both sides.

A detailed mapping of central parts of the core on OBSV 4.5 ($MgCl_2$), reveals precipitation of elements which favour distinct areas and forms partly geometric patterns (Fig. 32). A lighter grey tone is typical for calcite in the peripheral matrix core and a darker grey scale for the variety of precipitated minerals in the centre. Magnesium dominates the central part, and barely occurs in matrix adjacent the boarder and further diminish with distance from the hole. Calcite dominates the matrix of the core, and the abundance in the central hole is less pronounced. The opposite distribution of magnesium and calcium creates a distinguished boundary. Silicon and oxygen tend to establish a similar pattern, where silicon builds up on both sides of the boundary and oxygen prefers accumulation in an inner circle (Fig. 32 f and i).

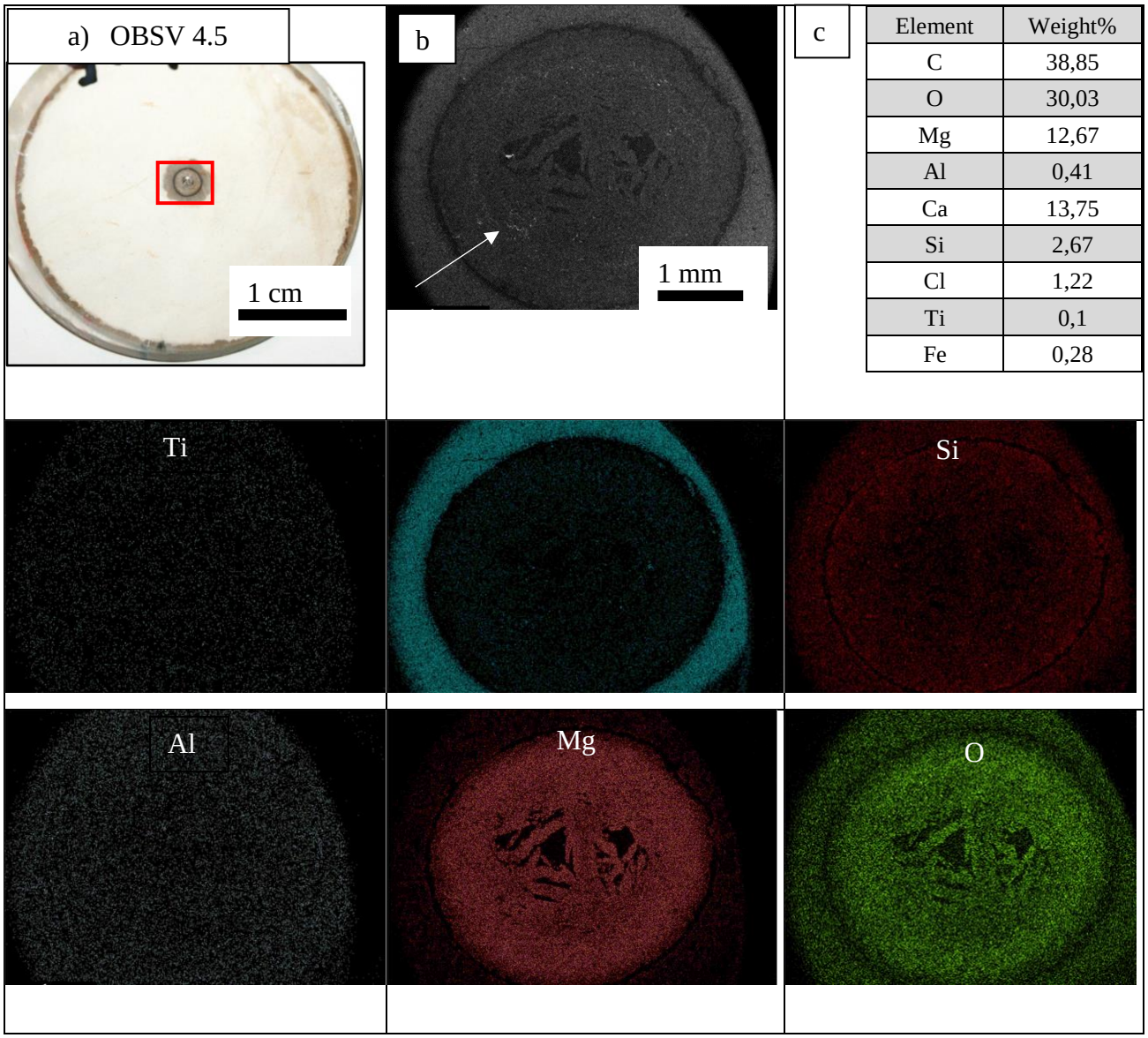

Element	Weight%
C	38,85
O	30,03
Mg	12,67
Al	0,41
Ca	13,75
Si	2,67
Cl	1,22
Ti	0,1
Fe	0,28

Fig. 32) Mapping of elements for OBSV 4.5 ($MgCl_2$) a) Location of mapping area. b) BSE image shows a lighter grey circle. c) Table of elements. The remaining images are distribution of Ti, Ca, Si, Al, Mg and O.

OBSV 12.5 (SSW) has high abundance of mineral accumulation in the central area. The original hole was refilled by precipitated minerals. The central area was mapped (Fig. 33). The distribution of elements revealed a lower calcite concentration inside the hole (Fig. 33 d). This is the only element that obtain an unevenly distribution.

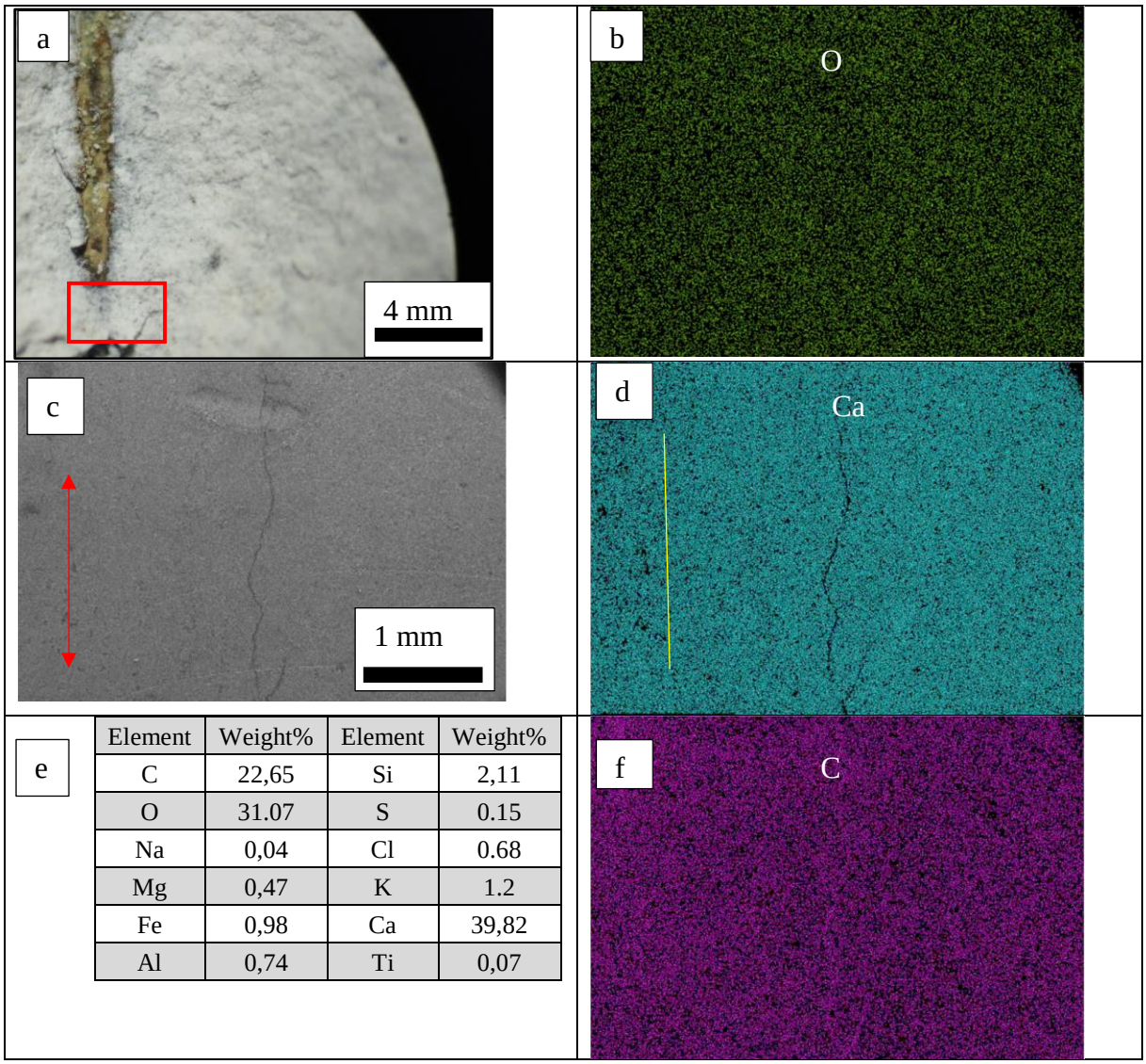

Element	Weight%	Element	Weight%
C	22,65	Si	2,11
O	31.07	S	0.15
Na	0,04	Cl	0.68
Mg	0,47	K	1.2
Fe	0,98	Ca	39,82
Al	0,74	Ti	0,07

Fig. 33). Element distribution of OBSV 12.5 (SSW). a) Location at where sample is extracted on an identical sample. b) Even distribution of oxygen. c) Greyscale of mapped area. Red arrow highlights water transfer. d) Calcite accumulation is less dense in the central area. The original border of the hollow cylinder is possibly on the left side of a yellow line. e) Composition of elements. F) Distribution of carbon.

Similar mapped area for OBSV 18 (NaCl) was achieved. Almost pure calcite occurred, evenly distributed with minor content of additional elements (Fig. 34)

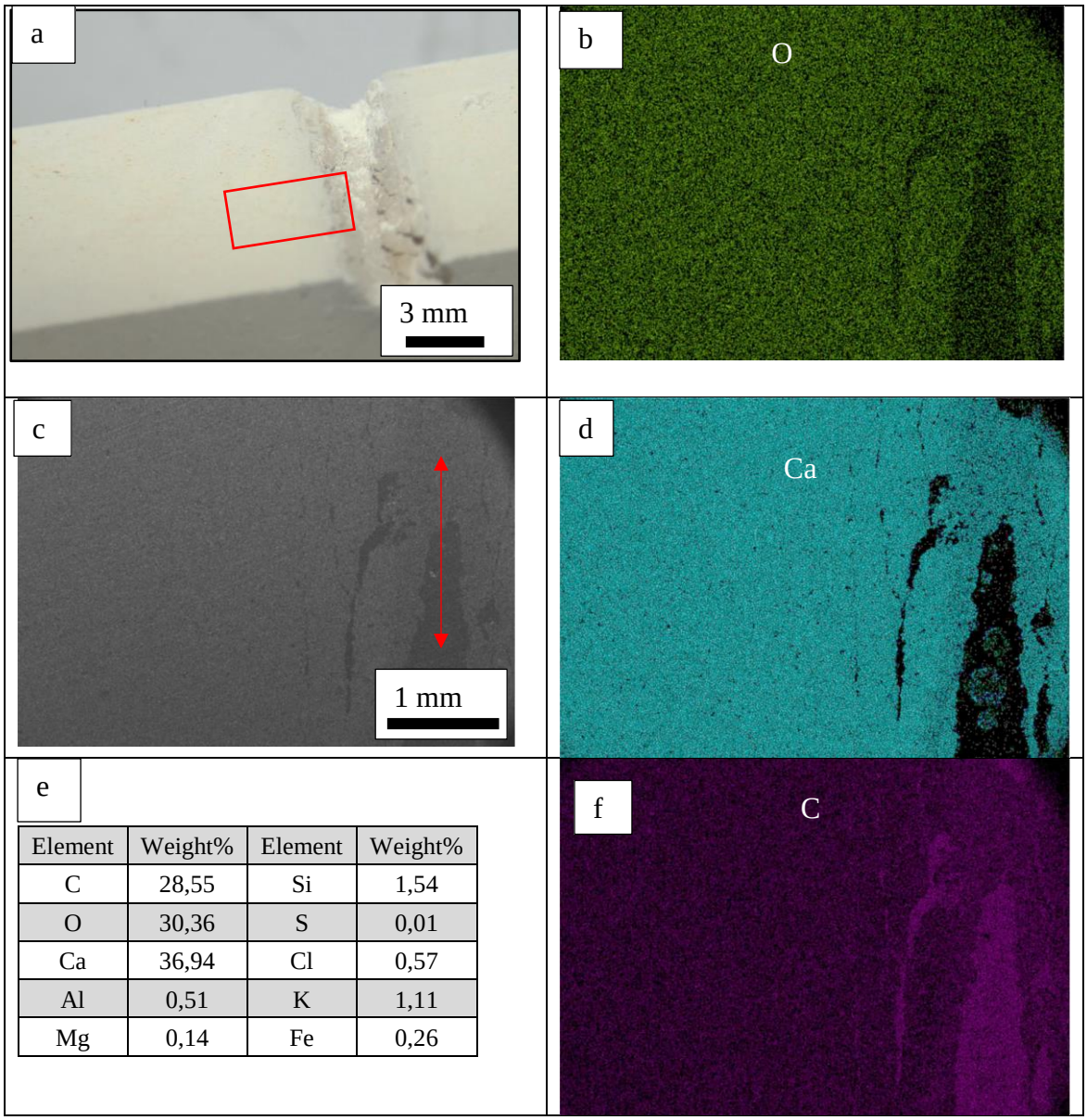

Element	Weight%	Element	Weight%
C	28,55	Si	1,54
O	30,36	S	0,01
Ca	36,94	Cl	0,57
Al	0,51	K	1,11
Mg	0,14	Fe	0,26

Fig. 34) The elements occurrent in OBSV 18 (NaCl), are evenly distributed. a) The location from where the sample is extracted is demonstrated on an identical sample. b) Distribution of oxygen. c) SEM micrograph with flow direction marked by an arrow. d) Distribution of calcium. e) Collected EDS results of the entire map. f) Carbon tends to accumulate in porous space in epoxy.

5.5 Mineral Liberation Analysis (MLA)

5.5.1 Calcite dissolution

Two slices representing each core were analysed, with the purpose of comparing inlet (green) versus outlet (grey) for all five cores (Fig. 35 a). One exception is for core OBSV 12 (SSW), where the inlet core was not available. The second slice was however available for the same purpose. All samples were scanned and all minerals occurrent were quantified by MLA. The reference rock contains a total of 95,07 % calcite. The remaining samples have been depleted in calcite compared to the reference sample. Cores injected by NaCl have a higher quantity of calcite in the inlet compared to the outlet. The opposite trend is observed for cores injected by $MgCl_2$ and SSW. The overall content of calcite is lowest for cores injected by $MgCl_2$.

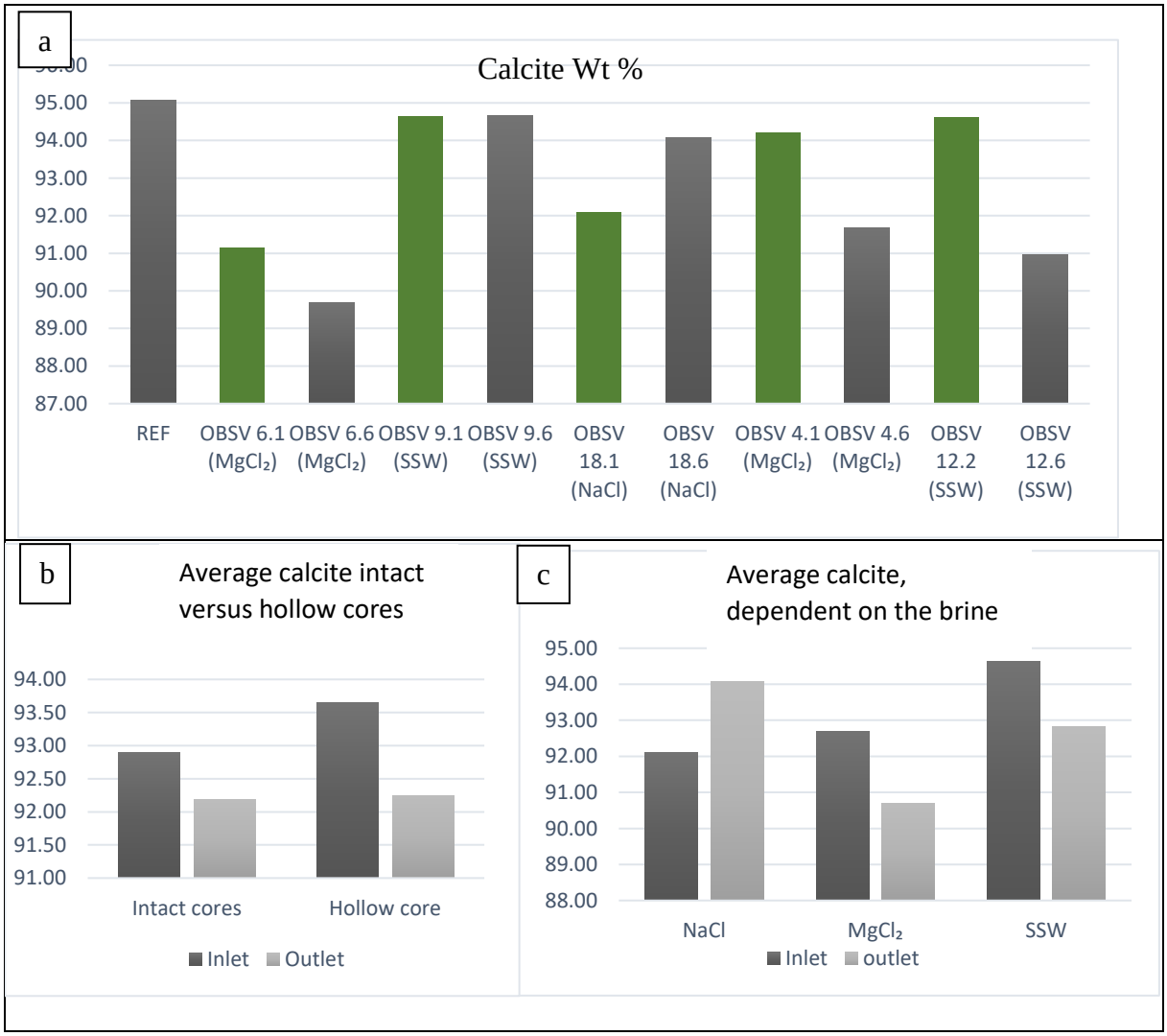

Fig. 35 a) Calcite content is 95,07 % for the reference rock. The graph distributes various, but lower quantities for the remaining samples. b) Calcite content decreases from inlet to outlet. This reduction is more prominent for hollow cores. c) Considering the brines, $MgCl_2$ affects calcite dissolution the strongest. Wt% (weight per cent)

5.5.2 Mineral dissolution and precipitation.

The reference rock has 4,97 % additional minerals. Abundant minerals are chlorite, quartz, muscovite, orthoclase, and other unrecognized minerals (Fig. 36). These elemental groups which have not been recognized, have similar compositions as other minerals and challenge a correct distinction. Trace elements are not included in this context. A gross evaluation of relative quantification of minerals in the reference rock, compared to an average of all the flooded chalk, presents a change in composition. The flooded cores show a lower content of quartz, orthoclase, muscovite and mixed phases with the chemical composition of CaSiAlSKO and CaSiFePAlMgO. An increase of mainly chlorite and mixed phase of SiCaO is observed. Mixed phases may occur because of the resolution limit of EDS at 1-2 micron and these phases may have been smaller or their intergrowth may be on < 1-micron scale. Pyrite occurs in flooded cores but is not detected in the reference rock. Percentages of TiO-mix exhibit relative similar values.

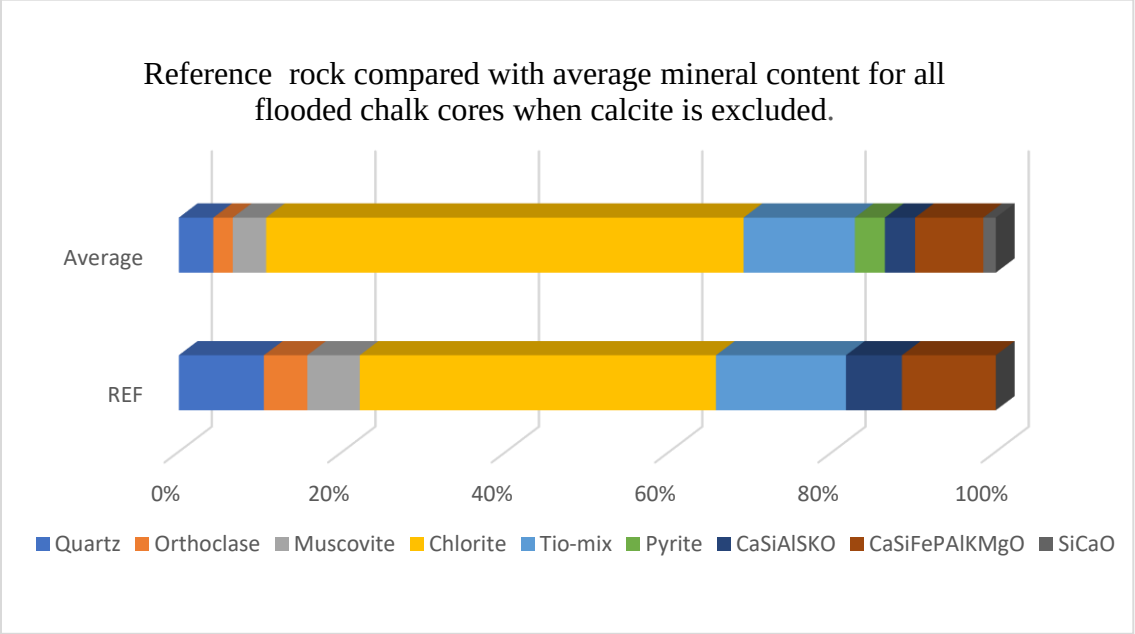

Fig. 36) A relative comparison of the major components, excluding calcite, showing the reference rock compared with an average of the flooded samples.

The change in mineral composition of the flooded cores regarding absolute quantification of the specific sample, is presented in Fig. 37. The increase of chlorite is detected in all cores. This increase ranges from not significant, to tripled values. The hollow cylinder cores injected with $MgCl_2$ and SSW show both an increase at inlet level outlet. OBSV 6 and 18 have high levels of chlorite at early stages at inlet but decreases towards outlet slices. Pyrite has occurred in samples OBSV 6.6 ($MgCl_2$), OBSV 12.2 (SSW) and 12.6 (SSW). The SiCaO- mix increases

for some samples, OBSV 18.1 (NaCl) and OBSV 18.6 (NaCl) and diminishes for other samples like OBSV 6.1 ($MgCl_2$), OBSV 6.6 ($MgCl_2$) and OBSV 4 ($MgCl_2$). For the remaining samples SiCaO achieve relative similar concentration. Content of TiO-mix displays nearly three times the value of the reference rock for the outlet sample of intact core injected by $MgCl_2$, (OBSV 6.6). OBSV 12 (SSW) has almost doubled its value from inlet to outlet samples. Quartz and orthoclase have diminished in some samples OBSV 6.1 ($MgCl_2$), OBSV 6.6 ($MgCl_2$) and OBSV 4.6 ($MgCl_2$) all injected by the same brine. The mixed mineral assemblage CaSiFePAIMgO in 18.1 (NaCl) (1,33%) has more than twice the amount compared with the reference sample (0,52%). OBSV 9 (SSW), inlet and outlet, have both similar quantity and mineralogic composition as the reference (Fig. 37).

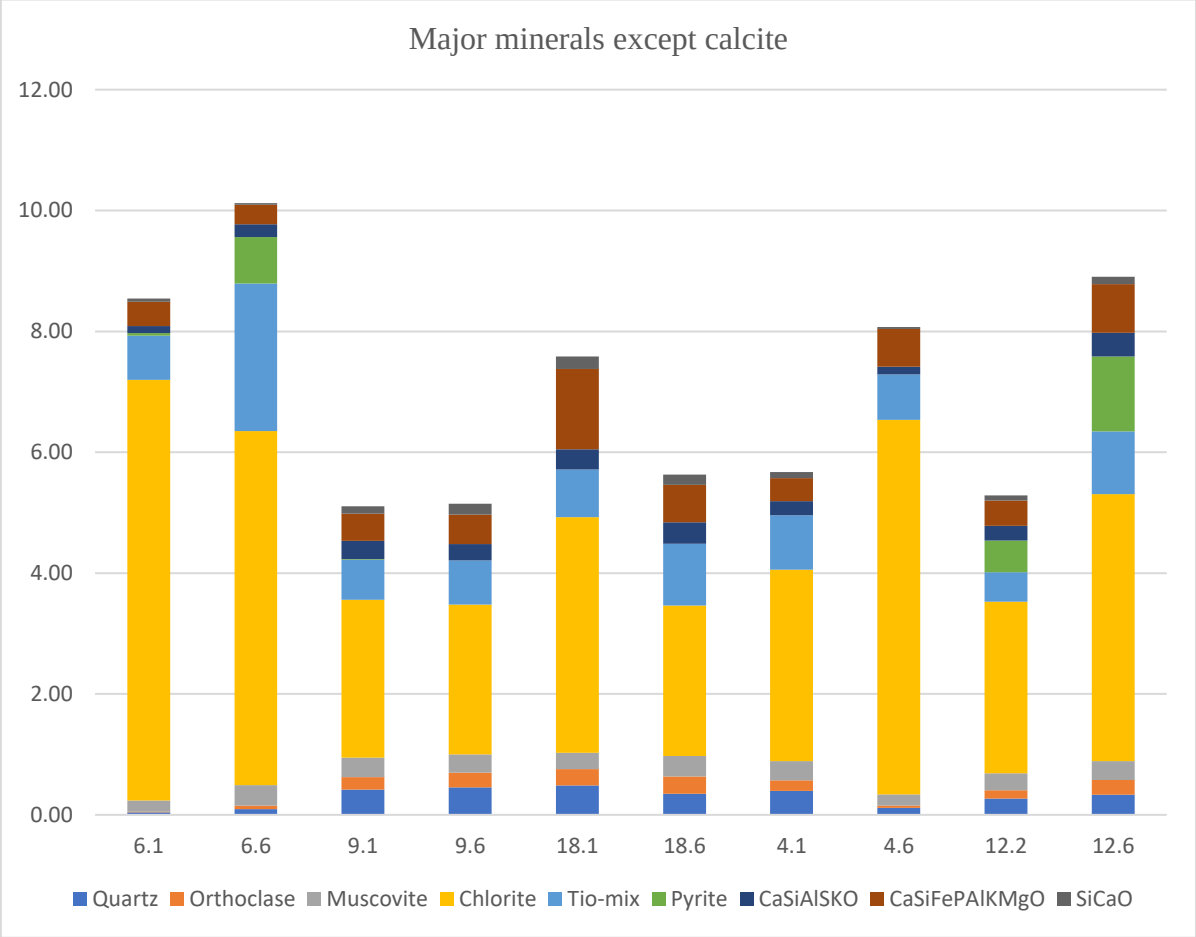

Fig. 37) Absolute levels of major minerals, except for calcite, and the distribution for each sample.

5.5.3 Coloured maps and mineral distribution perpendicular to flooddirection.

Coloured maps and distribution of minerals from the peripheral to the central parts of the cores are presented in Fig. 38 a and b. The overview displays three images from each sample, where the left images represent peripheral part of the sample, the right images represent an area close to the centre of the core and the middle images represent a location from somewhere in between. Each mineral has been assigned a specific colour. White areas are linked to porosity. Porosity is a property exposed to change by injecting brines. OBSV 6.1 ($MgCl_2$) has a lower porosity compared to the reference sample and has a slightly higher porosity in the central part. OBSV 12.2 (SSW) has lower porosity for mid- and peripheral parts of the core. The abundance of calcite is represented by three separate colours in blue, depending on the contamination of Si. These mineral grains are so small that they may not be distinguished and appears as a mix for the light blue (Calcite_2). The distribution of the different calcite compositions is dependent on the porosity itself and slightly higher content of pure calcite in cores with the lower porosity.

As seen from previous graph (Fig. 37), a decrease of chlorite is expected regarding OBSV 6.1 ($MgCl_2$). This trend is visible, where the chlorite is more abundant in inlet slice than outlet (Fig. 38 a) Higher accumulation of chlorite in the precipitated hollow cylinder OBSV 12 (SSW) is demonstrated in Fig. 39. Chlorite is evenly distributed in the matrix of the same core (Fig. 38 b).

Pyrite is observed in OBSV 6.6 ($MgCl_2$) with the highest abundancy in mid-peripheral zone. Pyrite is not recognized for the associated inlet slice. Pyrite also occurs in OBSV 12 (SSW). The outlet slice has high accumulations in the central area (Fig. 38 b).

An unusual excessive accumulation of titanium oxide at the peripheral parts of 18.6 (NaCl) is completely dominating the area in an absence of calcite (Fig. 38 b). The appearance of titanium oxide is in general evenly distributed.

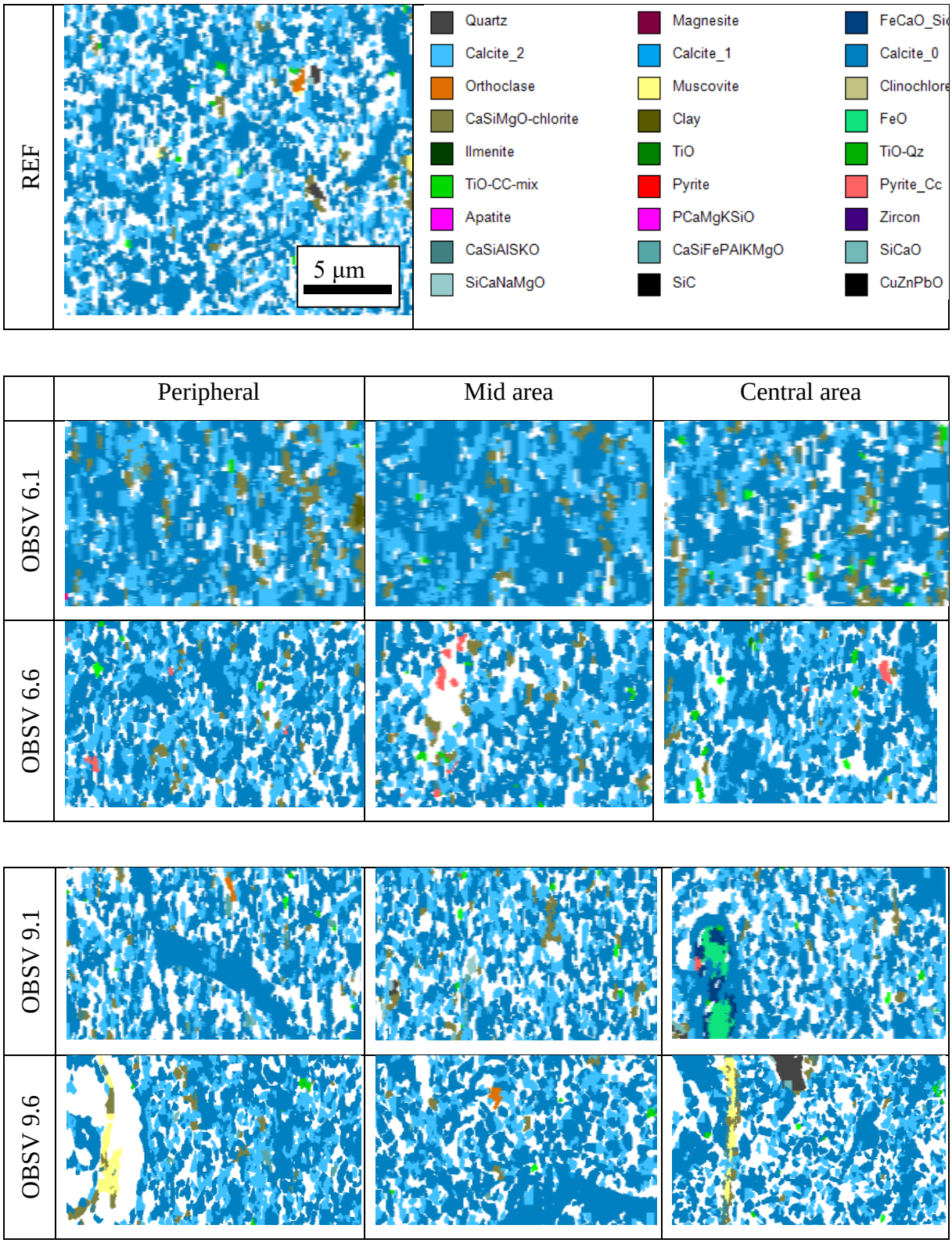

Fig. 38 a) Coloured maps distributing images from peripheral (left) to central part of a core (right). Figures have same scale. Chlorite (green) is more abundant in 6.1 ($MgCl_2$).

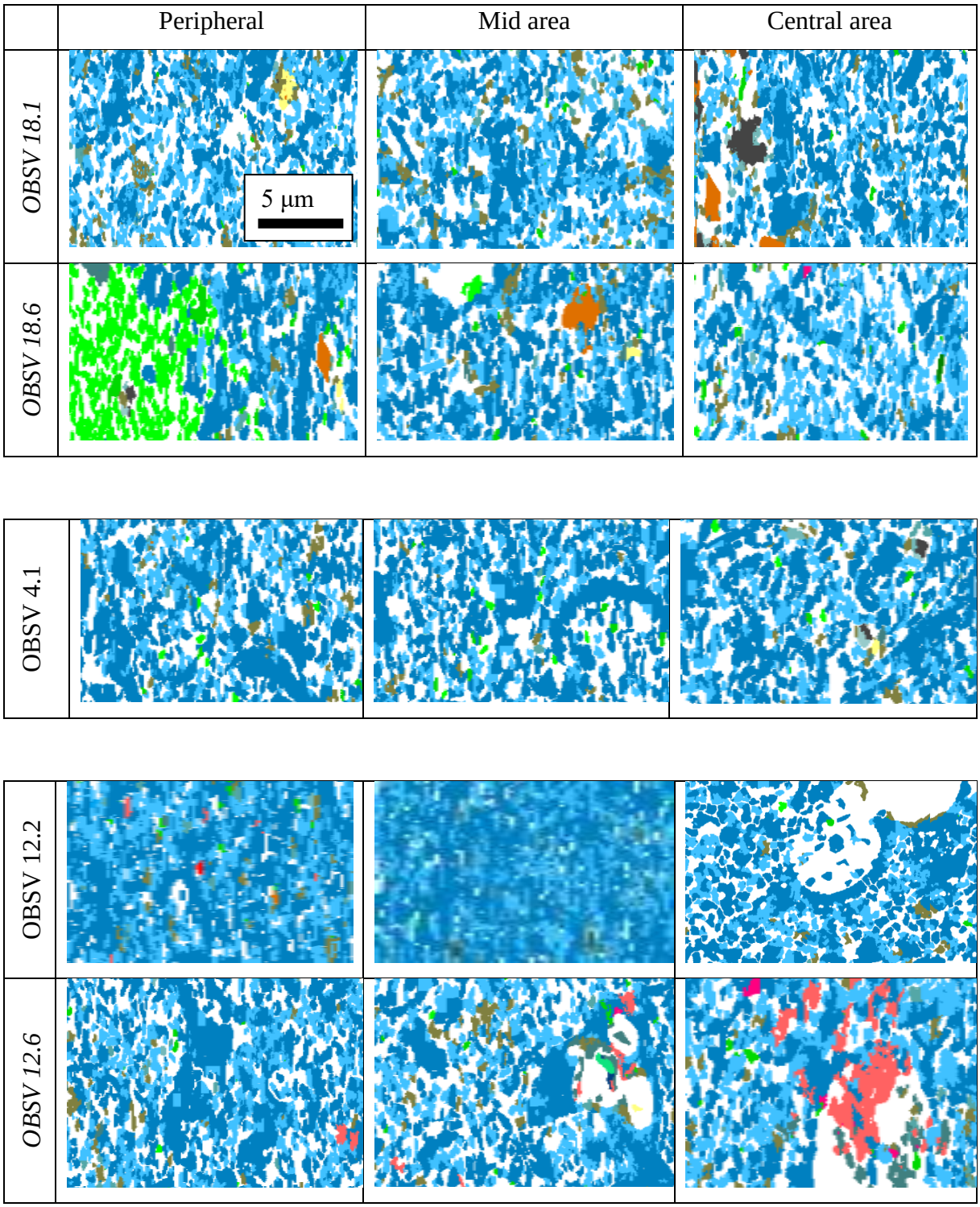

Fig. 38 b) OBSV 18.6 (NaCl) have increased level of silicon bearing calcite in central part (light blue)- OBSV 4.1 ($MgCl_2$) has slightly higher content of TiO-mix than other samples, except for the accumulation in OBSV 18.6 (NaCl). OBSV 12.2 (SSW) has low porosity in mid and peripheral areas. Pyrite is present in both samples of OBSV 12 (SSW) and tends to accumulate close to centre of the core of OBSV 12.6 (SSW).

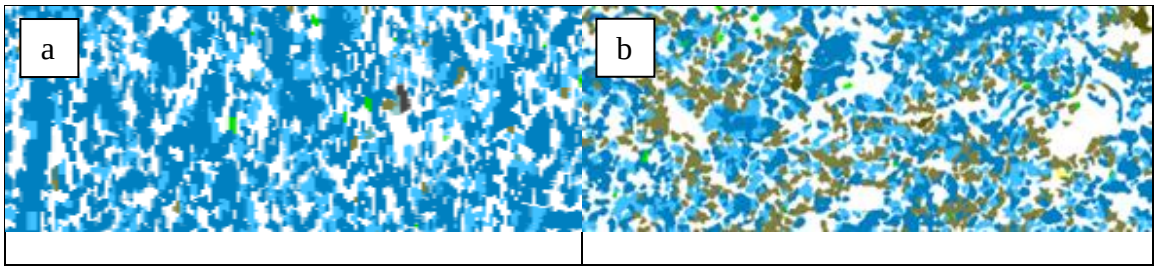

Fig. 39 a) Reference rock and low distribution of chlorite (green). B) The image has higher accumulation of chlorite in OBSV 12.2 (SSW). The image is extracted from the central hollow area.

5.6 Focused Ion Beam (FIB)

Three FIB-samples were prepared for further examination by the transmission electron microscope. The selected cores are OBSV 18.5 (NaCl), OBSV 4.5 ($MgCl_2$) and OBSV 12.5 (SSW). The FIB samples were all acquired from the precipitated minerals in the hollow area (Fig. 40). The OBSV 18.5 (NaCl) was extracted from a border between original matrix and precipitated minerals in central area. The FIB-sample has a distinct accumulation of epoxy in the mid area limited by the green lines (Fig. 40 c) which possibly represent the boundary between matrix and precipitated minerals. The precipitated minerals are located at right side of the epoxy. OBSV 4.5 ($MgCl_2$) is extracted from within the centre of precipitated minerals (Fig. 40 d). The surface of the polished sample is homogenous (Fig. 40 e). Sample OBSV 12.5 (SSW) is also obtained from precipitated minerals close to centre (Fig. 40 g).

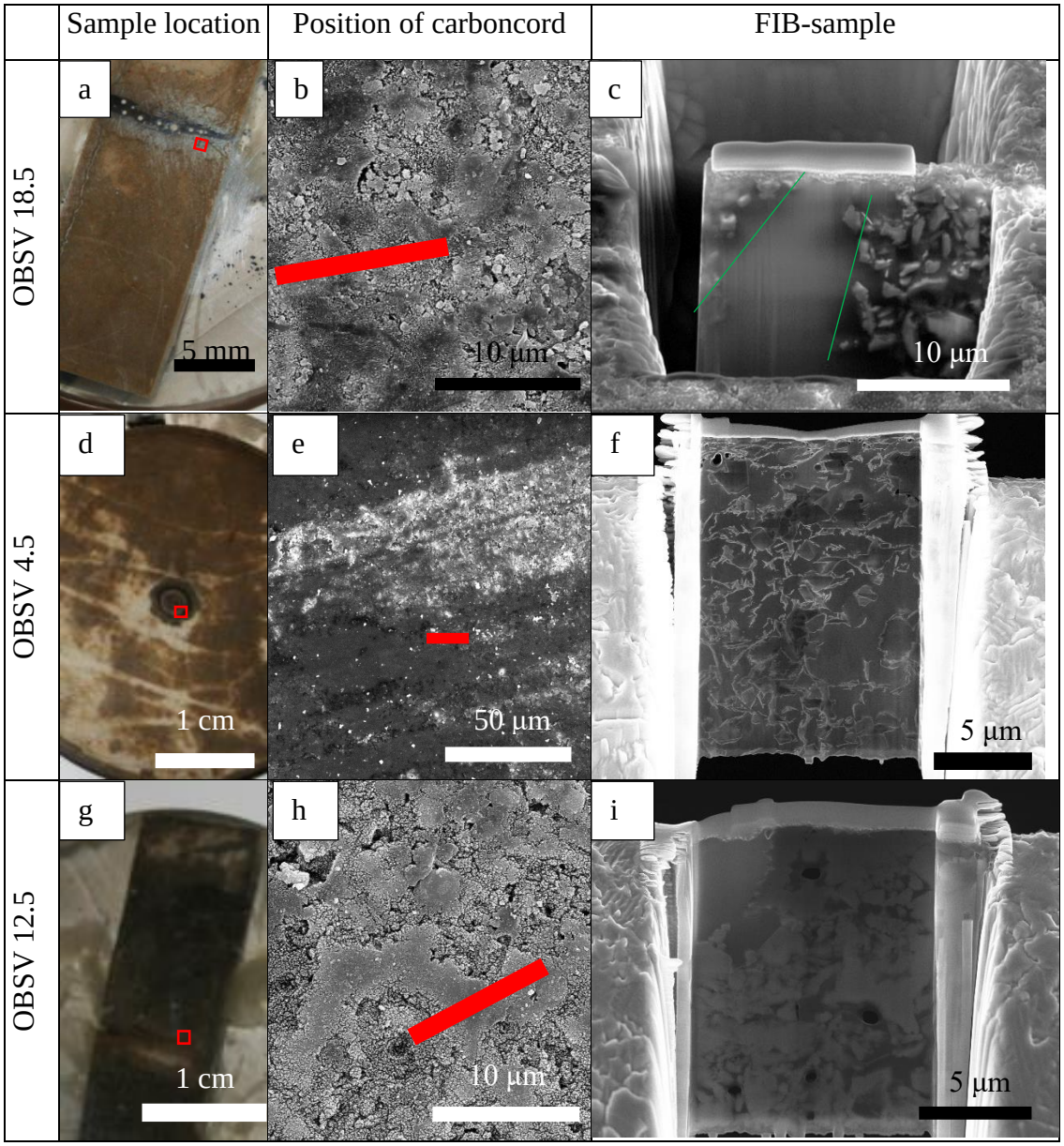

Fig. 40) Three TEM-samples were prepared. a) A central location from where FIB-TEM sample OBSV 18.5 (NaCl) is extracted. b) SEM image the location of the carbon-cord for OBSV 18.5 (NaCl). c) Prepared FIM-TEB sample for OBSV 18.5 (NaCl). d) Location from where FIB-TEM sample OBSV 4.5 ($MgCl_2$) is extracted. e) Polished and homogeneous surface where carbon-cord (red line) is applied. f) Prepared FIB-TEM sample displays euhedral shaped grains. g) Location from where FIB-TEM sample OBSV 12.5 (SSW) is extracted. h) Carbon-cord is applied on a microorganism. i) FIB-TEM sample of OBSV 12.5 (SSW) shows inhomogeneous distribution of grains.

5.7 Transmission Electron Microscopy (TEM)

5.7.1 Sample OBSV 18.5 (NaCl)

A few calcite grains were detected in OBSV 18.5 (NaCl) (Fig. 41). A needle shaped grain which measures one µm and approximately 0,2 µm was too small to retrieve the crystal pattern (Fig. 41 a). This grain is likely to be an authigenic feldspar due to its shape and composition of elements. Several nearby grains the feldspar, were measured by EDS and emitted calcite spectra (Fig. 41 b). Some samples tend to emit X-ray from Cu (Fig. 41 c). This is contamination due to the short distance from the Cu- grid which the sample was welded to, called an omniprobe. This was more prominent for samples close to the edge.

Location of measure	Spectra	Quantification of elements
a 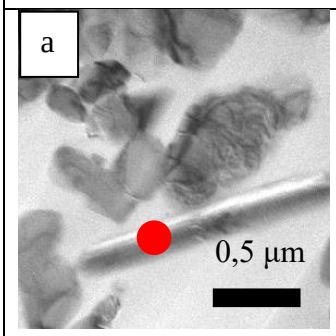	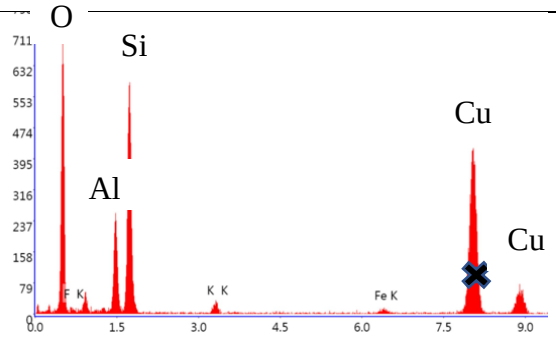	Element / Weight%: O 67,45; F 4,46; Al 9,48; K 0,47; Si 17,99; Fe 0,15
b 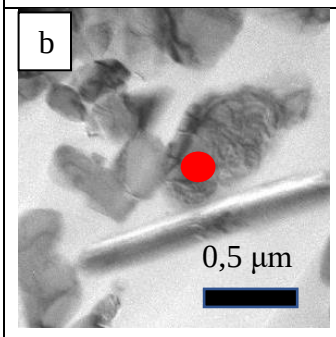	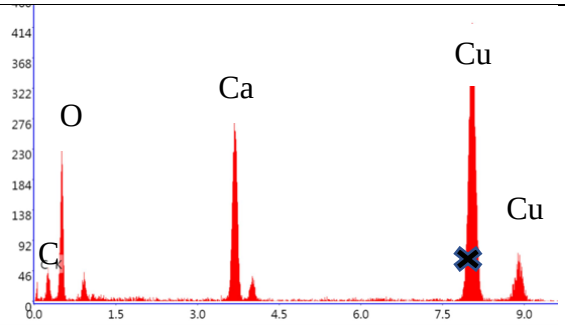	Element / Weight%: O 77,38; C 17,09; Ca 5,53
c 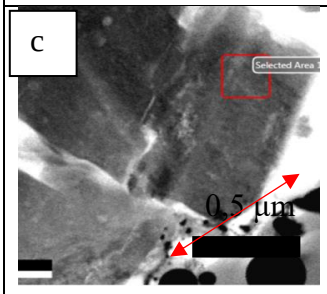	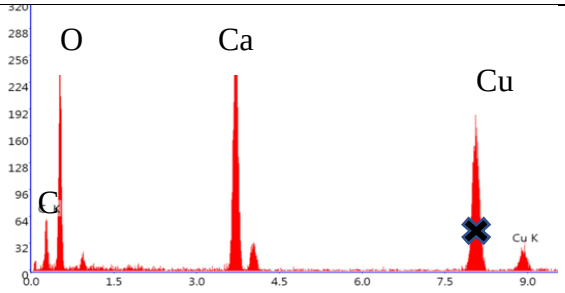	Element / Weight%: O 67,10; C 22,65; Ca 4,42; Cu 5,83

Fig. 41) Three different grains subjected for EDS in a TEM sample extracted from BSV 18.5 (NaCl) and its associated spectra and elemental distribution. a) A possible precipitated feldspar. b) Calcite. c) The spectra presents calcite with contamination of Cu from the cupper grid the sample was welded to, called omniprobe. The location of the sample was close to the edge of the sample (red line).

Crystalline patterns were obtained for some grains (Fig. 42).

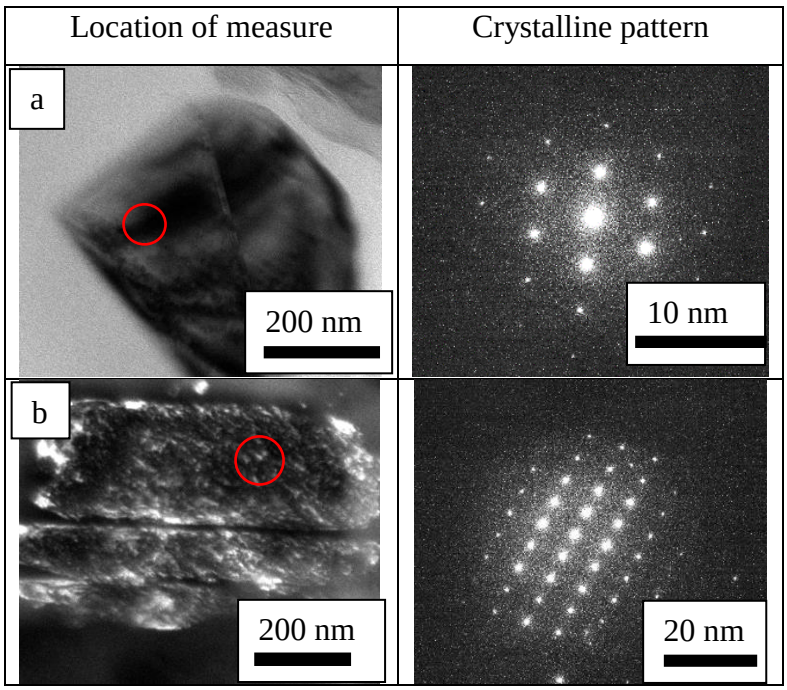

Fig. 42) Two different locations with associated crystalline pattern. The red circle highlights the area of analysis. a) Subhedral grain of 400 nm length obtained crystalline pattern. b) A grain of 700 nm also obtains crystalline pattern.

5.7.2 Sample OBSV 4.5 ($MgCl_2$)

The characteristic shape of euhedral grains in sample 4.5 ($MgCl_2$) (Fig. 40) distinguishes from calcite grains previously measured for OBSV 18 (NaCl) (Fig. 42) which presented subhedral and needle shaped forms. An EDS-map achieved from the area where the sample was extracted, revealed high content of magnesium, carbon and oxygen (Fig. 43). Gold (Au) was also measured followed by coating.

.

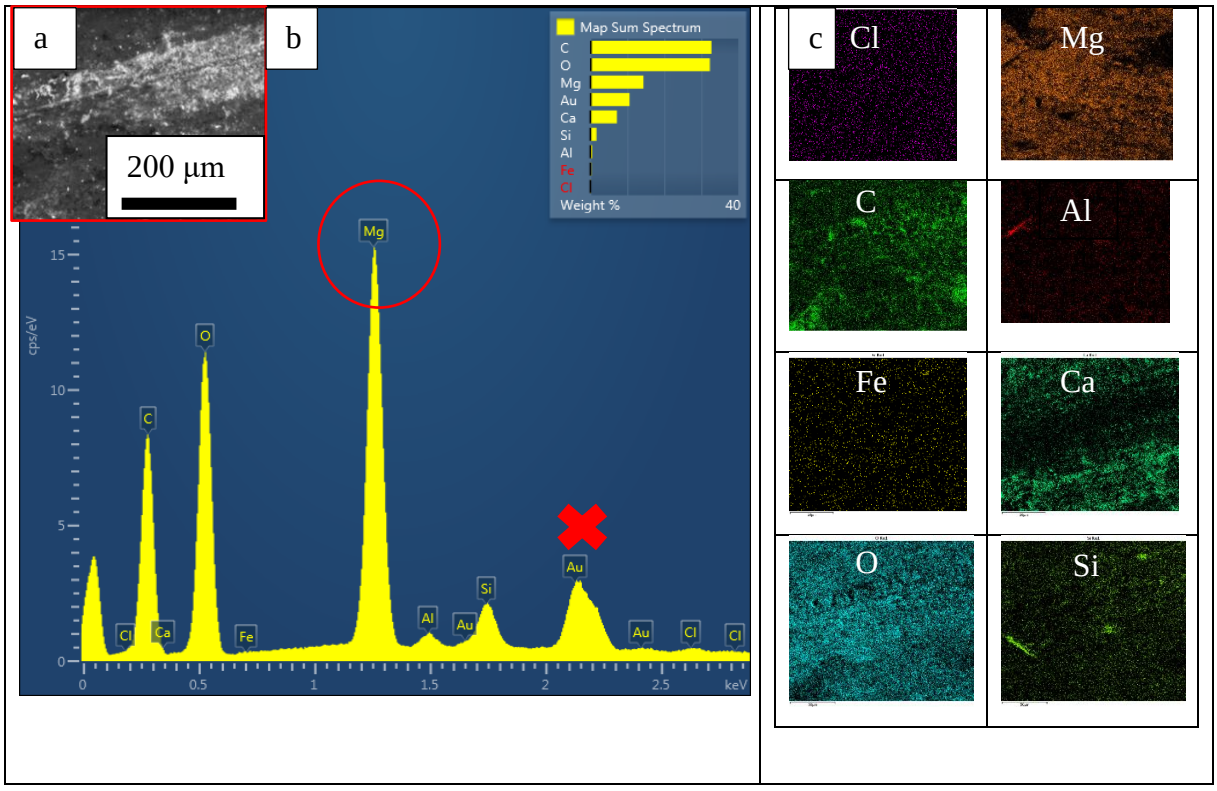

Fig. 43 a) Homogeneous surface at location of FIB-TEM sample. b) Spectra of mapped area have peaks corresponding to content of mainly Mg, C and O. Magnesite is likely to be abundant. c) Homogeneous distribution of elements at the location from where OBSV 4.5 ($MgCl_2$) was extracted.

Two crystalline patterns were achieved with associated EDS results (Fig. 44 a and c). Both implies magnesite. Another grain with similar composition as the two magnesite, holds a lower content of magnesium and abundant titanium (Fig. 44 b) The grain revealed an amorphous surface and does not permit any crystal structures.

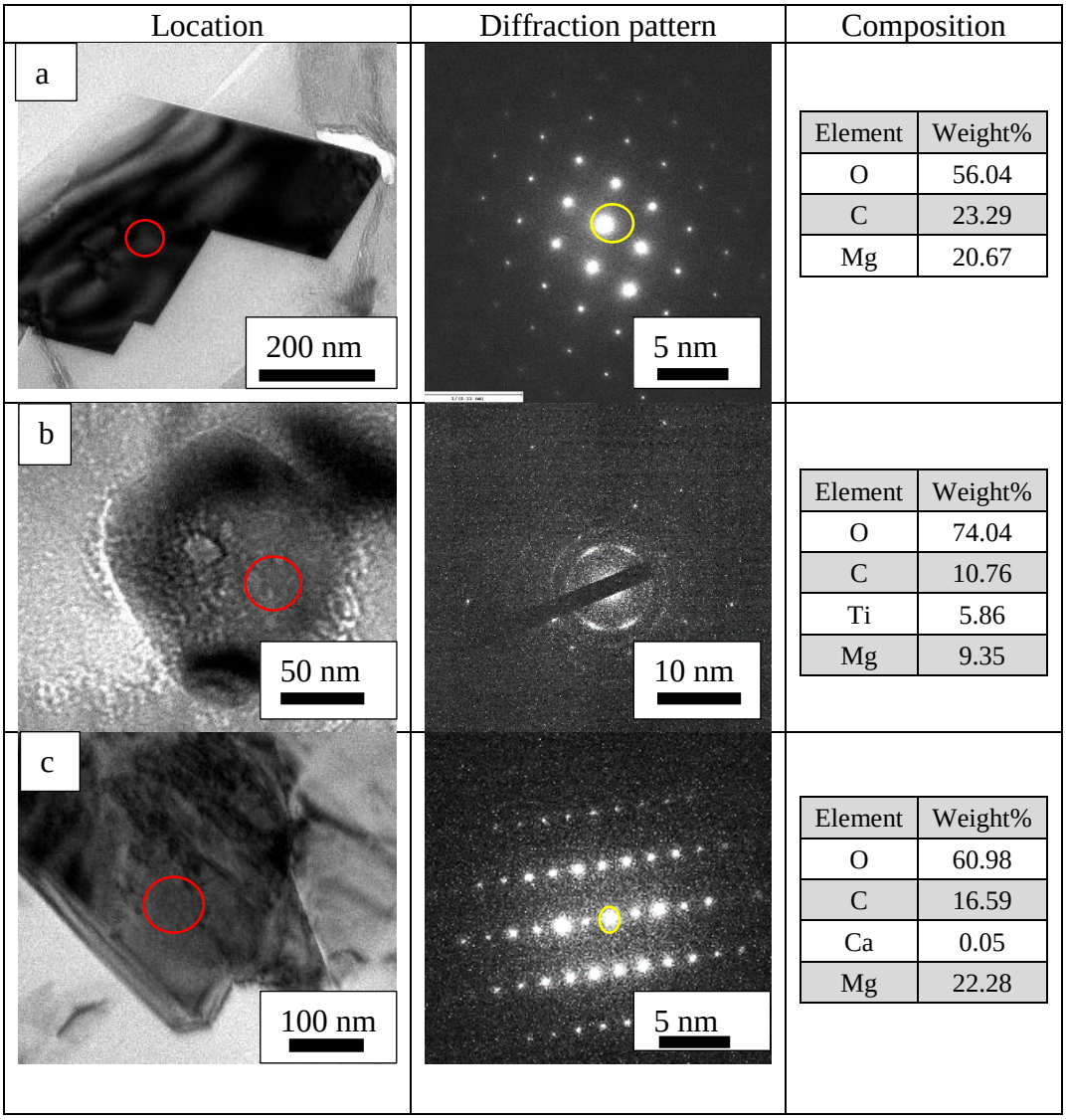

Element	Weight%
O	56.04
C	23.29
Mg	20.67

Element	Weight%
O	74.04
C	10.76
Ti	5.86
Mg	9.35

Element	Weight%
O	60.98
C	16.59
Ca	0.05
Mg	22.28

Fig. 44 a) EDS points at magnesite in OBSV 4.5. b) The grain displays an amorphous surface. EDS allows a recognition of magnesite with titanium c) The grain has a crystalline structure and EDS hints toward a magnesite.

5.7.3 Sample OBSV 12.5 (SSW)

The location selected for FIB- sample OBSV 12.5 (SSW) was a section of a microfossil, most likely a foraminifer. The FIB-sample show this feature of remains in the upper left corner clarified by a blue line (Fig. 45). A single grain inside the foraminifera is distinct compared to the surroundings. It is transparent and smaller than adjacent calcite grains. However, the EDS results confirmed that it is calcite. Point EDS- analysis elsewhere in the sample, all confirmed pure calcite.

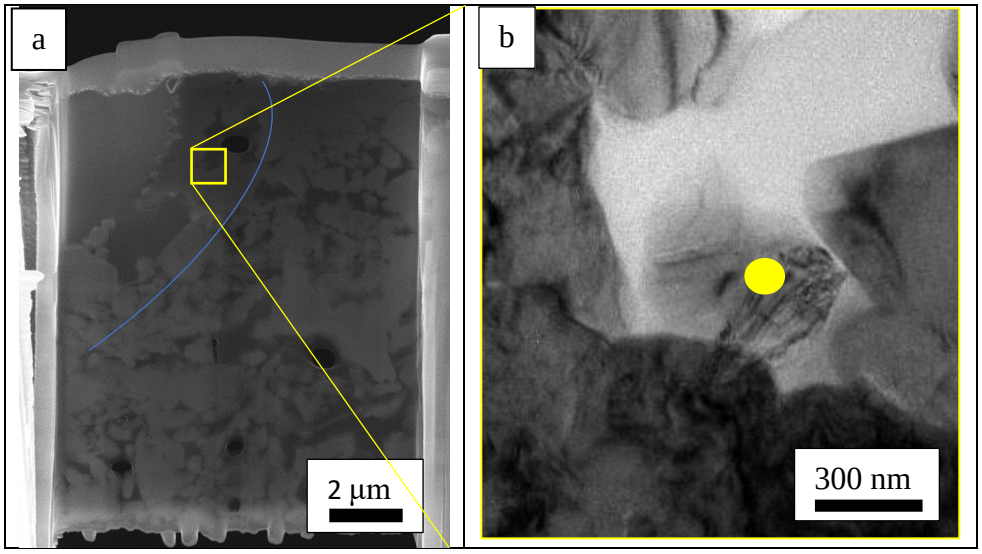

Fig. 45 a) FIB-sample for OBSV 12.5 (SSW) contains remains of a microfossil which is limited by a blue line. The EDS result is acquired in the yellow box. b) A possible precipitated grain is confirmed to be calcite, marked by the yellow dot.

Two crystalline patterns were also acquired in OBSV 12.5 (Fig. 46).

‘

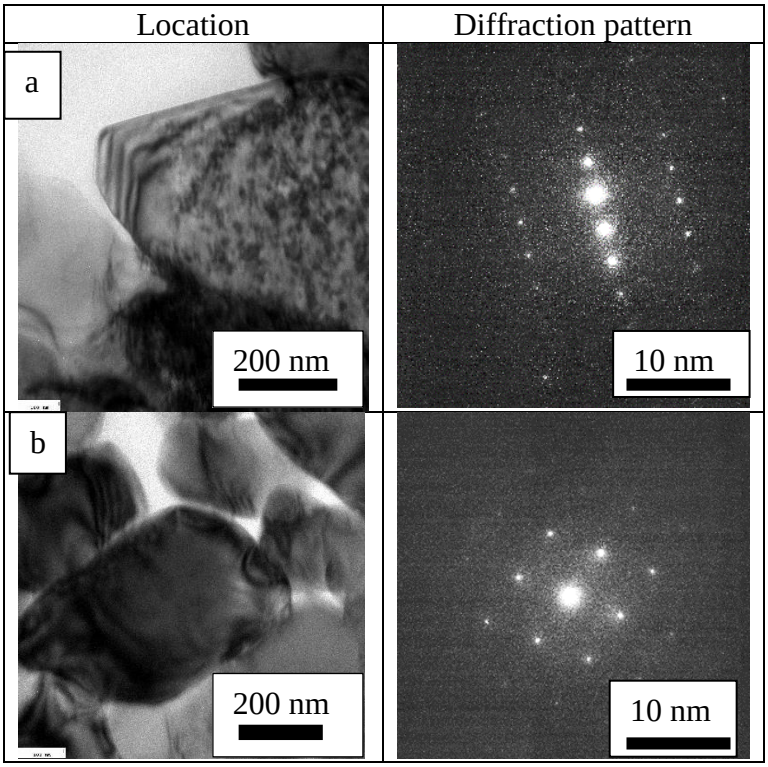

Fig. 46 a) Diffraction pattern was acquired (right image) from a grain imaged on left side. b) Dark grain in left image allowed a crystalline structure in the right image.

6. Discussion

The pattern of fluid transfer and diffusion within a core has through this study shown the importance of void space and connectivity of pores (Fig. 47). An interpreted flow-through pattern for hollow cores will pass faster through high porous space and further diffuse into lower permeability areas with a delay. It is likely that water transport in intact cores will distribute differently and most likely diffuse through slice by slice evenly. The time of arrival to the outlet slice will probably be longer than for hollow cores.

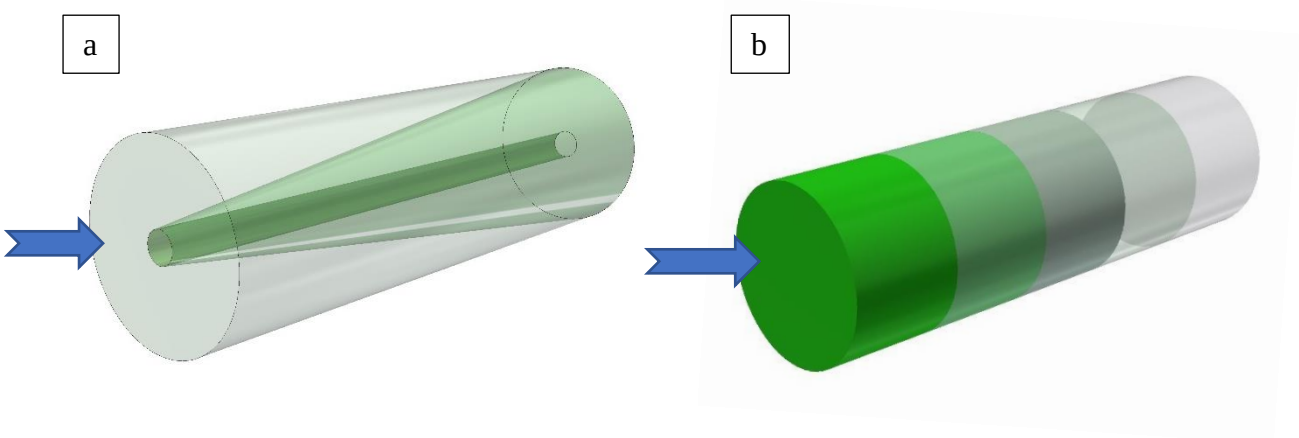

Fig. 47) Water transfer in hollow cylinder core versus intact core. Blue arrows indicate inlet and flooding direction. Dark green is related to area where fluid arrives first. The fluid will further diffuse into lighter green areas and finally have a delayed arrival in the lightest green locations. a) Hollow cylinder and water transfer indicates a preferred route through the central open space hence a delayed diffusion at peripheral parts most related to the inlet. b) Intact cylinder distributes a pattern of water transfer which allows the latest arrival at the outlet slice.

Calcite has been dissolved in all samples exposed to this experiment but to different extent. For some samples the process of dissolution has significantly altered the original mineralogical composition. Calcite dissolution may be caused by injecting brines, but also simultaneously by the compression applied to the core during flooding. OBSV 9 (SSW) was clogged after 20 days and flooding experiment stopped. The sample experienced an instantly rapid creep phase when SSW was injected, and this effect reduced during the last few days before it clogged. The final composition of both OBSV 9 (SSW) samples, compared to the reference rock (Fig. 37), distributed similar composition with insignificantly higher silicate and clay abundance in the flooded samples. Pores could have been clogged solely due to the compression and dissolution causing grain to grain contacts during flooding. OBSV 6 ($MgCl_2$) is also intact, and had same composition and characteristics, though this sample did not clog. The reason for OBSV 9 (SSW)

was clogged and OBSV 6 ($MgCl_2$) continued a more intense dissolution, is most likely related to the injected brine. OBSV 6 ($MgCl_2$) was the sample showing the highest degree of calcite dissolution (Fig. 35) included those samples with the hollow core. This indicates that $MgCl_2$ amplify the dissolution process more than SSW. This trend is coinciding with the measured effluent water, where $MgCl_2$ produced five times more calcium than samples injected with SSW (App. A). (Andersen et al., 2017) found that chalk from Aalborg injected with $MgCl_2$ displays strong increase in the specific surface area (SSA). An increase in SSA distributes a larger surface area that is exposed to additional dissolution and may contribute to the stronger dissolution for OBSV 6 ($MgCl_2$). On the contrary, this trend of increased dissolution by $MgCl_2$ was not evident comparing the cores with the hollow cylinder. The change in relative composition of calcite versus other minerals seemed similar, but calcite volume decreased slightly in OBSV 12 (SSW) when adding results from MLA. This difference in the dissolution trend is possibly related to water transport being more efficient through the hollow cylinder and diffuses simultaneously gently into the matrix. The arrival of diffused brine at peripheral parts is more likely to be delayed, hence a later onset of dissolution. The process of calcite dissolution regarding the hollow cylinder cores displaced an inhomogeneous pattern. OBSV 4.5 ($MgCl_2$) was exposed to a more prominent dissolution adjacent to the hole (Fig. 20 b) than the rest of the core. This is proven by the increased epoxy penetration closest to the hollow cylinder, indicating an area of higher porosity thus increased permeability. This may amplify the "flushed zone", which also has an increased accumulation of Si bearing minerals (Fig. 31 f). The size of the precipitated ring, measures approximately 3 mm. The drill used to produce this hole was 2 mm, which implies that the original hole was larger. However, this was not measured afterwards, and the original size is therefore unknown. The increase to approximately 3 mm could be a result of completely dissolved calcite along the inside hollow wall, hence enlarged the diameter. Another possibility is that increased the diameter developed solely due to the drilling process. (Angeliera et al., 2006) found that carbonate dissolution occurred near a fault. They argued that increased accumulation was caused by relatively insoluble material in layers (0.1-1 m) close to the fault zone on the hanging wall side of normal faults.

Nermoen et al. (2016) found that precipitation of magnesium-bearing minerals drives dissolutions of calcium ions in aqueous solution. It seems that precipitation of magnesium did not occur in OBSV 9 (SSW). The calcite dissolution and compression during testing was followed by a decrease in porosity and further reduced the permeability. Another interesting result is the change in abundance of calcite as opposed to "other" minerals from the inlet

towards the outlet regarding $MgCl_2$ and SSW, and that the calcite quantity decreases by almost 2 % (Fig 35 b). OBSV 6 ($MgCl_2$) experiences a reduction of 4 %. A further interesting result is the change of relative composition of calcite versus non-carbonatic minerals from the inlet towards the outlet in $MgCl_2$ and SSW flooded cores, as such that the quantity of calcite decreases (Fig. 35 c). The difference might be related to the impact of the hollow cylinder and the flow-through pattern, previously interpreted. The dissolution is more prominent towards the outlet. This could be explained by the injected water being less able to diffuse into the matrix from the easy flow-through path in the centre. The opposite was the fact for the core injected by NaCl, where relative content of calcite increased by 2 % from the inlet slice compared to the outlet. This contrasting observation may be related to contamination of the inlet slice, or optimal conditions for precipitation at or near the inlet. It could also be explained by NaCl having different dissolution effects on the calcite.

The impact of calcite dissolution could also be dependent of the reaction with present silicate. Lind (1993) found that dissolution of calcite takes place when it is in contact with silicates. Fabricius (2003) discovered that stylolites form where high concentrations of silicates are already present. She also argued that carbonate dissolves adjacent stylolites and that calcium may cause cementation of the pore-space followed by a decrease in porosity. Calcite is highly soluble, furthermore dependent on pH values.

Dissolved calcite in a flooding experiment is likely to be redeposited. Considering the hollow samples, the most favourable location of deposition of calcite is accumulation along inside the wall of the hollow cores regarding OBSV 18 (NaCl) and OBSV 12 (SSW). Observation of OBSV 4 ($MgCl_2$) showed mainly magnesite ($MgCO_3$) precipitation in central areas (Fig. 43 b). Calcite is likely to be redistributed in the matrix and crystalizes as well as contributing the reduction of total porosity. Observation of a calcite crystal inside the shell of a microorganism may be an example of redistribution of intra porosity. Wanless (1979) described that intra-fossil porosity in some microfossils is reduced by calcite cement when studying North Sea chalk. Zhou and Zheng (2001) found that during dissolution of calcium carbonate under reservoir conditions and precipitation of non-carbonate minerals, there will also occur reprecipitation of $CaCO_3$.

A chalk reservoir may have various content of silicate, depending on the depositional environment. The quantity of non- calcite minerals was for the reference rock 4,93% recognized by MLA. Next to chlorite (1,97%), the highest concentration of a non- calcite mineral is the

TiO-mix (with Cc and Qz), like ilmenite ($MgCO_3$), with 52 % Fe, which also was identified as precipitation in the hollow cylinder (Fig. 29 b). The third most abundant mineral was the combination of CaSiFePAl,KMgO which was recognized by MLA. This counts for 0,52% of the rock, or 10.5% of the non-carbonate content and is interpreted as an intergrowth of apatite and a phyllosilicate. Observation by light microscopy allowed the determination of rounded green minerals. As previous described for the evolution of the Mons basin, the Saint Vaast Formation was deposited on top of glauconitic sand. During uplift, slopes developed, and chalk may have been mixed with the glauconitic sand after redeposition through slumps or turbidity currents or other gravity flows. This explains the presence of glauconite in the samples. Other abundant minerals in the reference rock are quartz, orthoclase and muscovite as identified by MLA. Calcite, muscovite and quartz were confirmed by measurement of XRD (Fig. 24). Occurrence of these latter minerals may be related to detrital input from distant deltas.

The composition and quantity of non-carbonatic minerals and their reactivity can play an important role in fracture-controlled fluid networks. Dissolution may be dependent on the brine and the level of pH. Dissolution of silicate and clay minerals generates new void space, removes cement and physically transports mineral grains. Reservoir temperature influences the progress of a fluid network evolution but was not an issue in current study, as the temperature was set to reservoir conditions at 130°C. Muscovite is a sheet silicate mineral with potassium and aluminium present. Dissolution of muscovite is likely to effect evolution of fluid flow. OBSV 4.6 ($MgCl_2$) and OBSV 6.1 ($MgCl_2$) had significantly lower amounts of muscovite while the remaining flooded sample showed no variation. This could indicate that the influence of $MgCl_2$ may enhance dissolution of muscovite. Lammers et al, (2017) found that concentration of Al, Si and K dissolved in muscovite is dependent of pH. A reduction of pH-value from 7.6 to 2,5 was followed by a reduced concentration of muscovite. Steady concentrations at 7,6 and reduced concentrations at 2,5 pH. They also implied that temperature was strongly related to pH value.

Precipitation of minerals is a result of an exchange between the brine injected and composition of the original rock. Not only dissolution, but precipitation of specific minerals is also dependent on environmental conditions as temperature and pH. Temperature was set to 130° C, and as previously mentioned, this was not a parameter to change. Location of the precipitated minerals is dependent on the permeability and void space. Precipitation may narrow or seal off fluid pathways as was the case for OBSV 9 (SSW) which was clogged after 20 days of flooding.

The most remarkable observation among precipitation, was the occurrence of pyrite (FeS_2). Pyrite was not counted at all in the reference rock. However, a level of 1,24 % was recognized by MLA for OBSV 12.6 (SSW) (Fig 37). Pyrite was also identified at the inlet slice of the same sample. The same trend was observed for OBSV 6.6 ($MgCl_2$) with an increase from inlet to outlet. Pyrite was also detected by the high contrast in greyscale micrographs (Fig. 30) as well as by observing the contrast of pyrite against the white calcite background by optical characterization (Fig. 23). Fabricius (2007) found that pyrite, among other minerals, frequently precipitated in and adjacent stylolites in the Tor Formation, North Sea.

The level of chlorite increased in all samples. The increase was insignificant regarding the intact samples flooded with SSW (Fig. 37), the one which was clogged. Simultaneously, this was the only mineral that increased during the short time the experiment lasted. The precipitation of chlorite was remarkable especially for OBSV 6.1 ($MgCl_2$), OBSV 4.6 ($MgCl_2$) and OBSV 6.6 ($MgCl_2$). The quantity was 6,96%, 6,20% and 5,86% respectively. The content of the reference rock is 1,97% and is a significant increase. The same samples had at the same time the lowest quantity of quartz, muscovite and orthoclase. This coinciding observation indicate that the latter may have supplied the growth of chlorite. Fabricius (2007) found also when studying North Sea samples, a depth dependent change in clay mineralogy. She observed a change from smectite-illite via illite-smectite to smectite-chlorite by burial. A similar process of mineral transformation is likely to have taken place during the flooding experiment here.

The quantity of glauconite was unevenly represented in the various samples. An overall change showed an increase from 0,52 % to 0,58%, and this increase was more noticeable for OBSV 18 (NaCl) with an increase to 1,33 %. This increase is nonetheless insignificant. It is likely to explaine and increase by local variations at deposition. Nermoen et al. (2016) found that the purity of Saint Vaast Formation varied.

The precipitation of magnesite in central hollow area in OBSV 4, flooded with $MgCl_2$ was identified by several methods. Magnesite may have a white appearance and could not be distinguished from calcite using binocular (Fig. 19 e). Magnesite was however recognized by XRD, SEM and FIB-TEM analysis. This mineral was however not identified by MLA. This may seem unlogic as MLA detection turns out to give exact results with high resolution. The most likely reason for this, it due to sample preparation, where loose parts of the sample may have been slightly removed during mounting in epoxy and following not been detected by the microscopy.

A SEM micrograph images a mineral that is likely ilmenite ($FeTiO_3$) deposited on the surface of the hollow area of OBSV 4.3 ($MgCl_2$). Ilmenite was determined by its cubic form and the high content of iron, titanium and oxygen. On the other hand, the spectra were not unambiguous, and the decision it not final. Fabricius & Borre (2007) found that minerals that had derived from volcanic ash, would recrystallize while releasing iron to the porewater and incorporation magnesium gradually with depth, in their study on deep sea samples from Ontong Java Plateau and the Caribbean Sea. Ilmenite could have precipitated followed by dissolution of iron and titanium derived from detrital grains as this accumulation of ilmenite appears to be authigenic (Fig. 29 b).

An elongated mineral in OBSV 18.5 by utilizing TEM was recognized as authigenic feldspar due to the size and the mixed composition of OSiAlFK. Fabricius (2007) described that zeolites and feldspar, in addition to clay minerals, precipitate in chalk during burial diagenesis. Another event that may argue that this is authigenic feldspar, is that MLA detected this combination of elements (CaSiAlSKO) with a vaguely increase for OBSV 18 (NaCl) compared to the reference rock.

The different composition of the three brines utilized in this project, seems to influence the type of mineral that favours precipitation. NaCl and $MgCl_2$ are pure. The composition of SSW has a mix of elements including NaCl and $MgCl_2$ (App. 1). Additional components in SSW are Na_2SO_4, $NaHCO_3$, KCl, and $CaCl_2 2H_2O$. These six previously mentioned minerals that precipitated, were distributed in distinct cores with different quantities. The most significant precipitation due to flooding by NaCl was chlorite. Insignificant increase was noted for combination of CaSiFePAlKMgO (glauconite plus X like apatite) and possibly feldspar. $MgCl_2$ seems to favour precipitation of chlorite, titanium-oxid, magnesite, ilmenite. When it comes to SWW the samples are dominated by an increase in foremost chlorite and pyrite. Other minerals with less significant increase related to SSW, are titanium oxide and the combination, earlier mentioned, that might be glauconite plus apatite. This increase is however more likely to be a result of depositional variances. The summary (Tab. 2) indicate that chlorite precipitate independently of which brine that is injected. Pyrite seems to be related to $MgCl_2$. Since this brine does not contain FeS_2, it likely due to dissolving and mineral exchange caused by the brine. The increase in titanium-oxid could be reasoned by the same process, but this increase is probably more related to depositional variances. This implies that injected brine affects the core in facilitating precipitation of minerals.

Tab. 2) Brines injected and associated minerals that precipitate.

NaCl	Chlorite			
$MgCl_2$	Chlorite	Pyrite	Magnesite	Ilmenite
SSW	Chlorite	Pyrite		

Magnesite and ilmenite precipitated in the hollow cylinder core, OBSV 4, flooded with $MgCl_2$. The location of the precipitation of these minerals was indeed limited to the central hollow area. Neither magnesite nor ilmenite had been identified in the intact core, OBSV 6, flooded with the same brine. The precipitation of these minerals is dependent on the location. This could indicate that certain minerals are dependent on either a porous location or transfer of fluid. In this case, the fluid transfer will primarily pass the hollow cylinder and mainly precipitate magnesite and ilmenite from the fluid directly without further diffusing through the matrix.

Except the above mentioned that magnesite and ilmenite are limited to the central hollow area, the mineral distribution tends to be relative even. Another trend for same sample, OBSV 4, also accumulated silicon adjacent the hole in the flushed area described in (Fig. 31). Silicon content along with magnesium rapidly decrease and fade into the matrix core of OBSV 4 ($MgCl_2$). The crossing pattern linked to the central area (Fig. 23 d), is likely to be related to contraction of precipitated minerals, due to a smaller grainsize. This potentially contraction leaves an inner circle (white in the greyscale image) (Fig. 32 b) which indicate accumulation of lighter components. Simultaneously a higher accumulation in oxygen is recognized in the same circle. It is likely that a contraction is more efficient in this white circle and therefor epoxy is not allowed to penetrate at this location (Fig. 20 b).

A less obvious distribution chlorite was observed for OBSV 12 (SSW). MLA maps indicate a higher accumulation in the central precipitated area (Fig. 37). EDS maps were also collected from central area but did not point to distribute any variations in composition (Fig. 33). Not enough data is collected to determine where chlorite decreases from the centre core (Fig.37). However, by studying MLA maps it is possible that this increased chlorite accumulation is also limited to the precipitated hollow area (Fig. 38 b). No significant variation of chlorite along perpendicular to the flooding direction was noticed for OBSV 18 (Fig. 34). The same is applied for intact cores.

Several slices from the same core were analysed with the intention to study the importance of distribution of minerals from inlet to outlet. Regarding OBSV 9 (SSW) which was clogged,

was the only pair of samples (inlet and outlet) that presented a similar composition in both. In addition, the quantity of non-carbonatic minerals is 5,11% and 5,15% comparable to the reference rock with 4,97%. There was possibly not enough time for minerals to precipitate. The other intact core however, OBSV 6 (MgCl2), showed a tremendous change along the flood direction. The content of non-carbonate content increases from around eight to ten percent, by almost two percent of the whole rock composition from inlet to outlet. The initial high content of chlorite tends to decrease and simultaneously increase quantity of pyrite and titanium oxid. The two hollow cylinder cores injected by $MgCl_2$ and SSW, also present a trend of enhanced clay minerals growth from inlet to outlet. For OBSV 4 ($MgCl_2$) there is an increase of typically chlorite with a simultaneous decrease of quartz, orthoclase and muscovite, which indicates that the latter three contribute to precipitation of chlorite. Besides an increase in chlorite, a more than doubled value of pyrite is seen for the outlet slice compared to the inlet. This increase could explain that continuous fluid transport carry newly precipitated minerals from inlet along the flood direction. The hollow cylinder core injected by NaCl exhibit, on the contrary, a decrease in content of non-carbonates from inlet to outlet. This could be related to contamination of the inlet slice of OBSV 18 (NaCl), as previously mentioned.

The advantage of applying several methods to identify the distribution of minerals, is the fact that one method may support with data another and that the simple larger set help in evaluating the processes. If the here used variety of methods had not been accounted, important information might have been missed. MLA results were, by the way, not as expected. One problem with the MLA results is the resolution and scaling of the images. The original size of each frame measured 100 times 100 μm. These images lacked proper scale when results were returned from the MLA laboratory Freiberg. This means that the images given in Fig. 38 might have a misleading scale. The resolution of both samples of both samples of OBSV 4 ($MgCl_2$) were too low to be used. Another issue is that magnesite was not detected by MLA. The most logic explanation for this, is the challenging preparation of OBSV 4 ($MgCl_2$) due to central part of the precipitated minerals not being attached to the rest of the core. The preparation for MLA samples were performed first and differently compared to TEM and thinsections. The technique improved by cutting the sample perpendicular to the flood direction, instead of parallel to flood direction. This enhanced the ability to keep its original position. A paramount objective of this thesis might be the achieved knowledge of preparing challenging thinsection of chalk. The disadvantage when implementing six various methods, is the time-limit related to analysing all methods entirely. The identification of diffractions-patterns for TEM methods, is a skill that

needs experience to both perform and to distinguish and was left for the benefit of a future project. However, exactly that showed the project, that ideally expertise shall be combined.

The importance of simulating a fracture versus an intact core, it to highlight the importance of calcite dissolution and distribution of precipitated minerals dependent on void space and connectivity of pores. This essential precipitation is a key factor in fracture-controlled fluid networks where maintaining or increasing permeability is a goal. This study has shown that dissolution generates new void space, dissolves detrital grains and that secondary precipitation acts to narrow or seal off fluid pathways. Sheet silicate mineral reactivity is likely to affect permeability evolution in a chalk reservoir further. Water transport in hollow cylinder cores may mirror waterflow in reservoir styloliths. Fabricius and Hjuler (2009) found well-developed styloliths in deeply buried chalk of the central North Sea. Stylolithic joints are typical pressure solution features and typically occurrent in highly porous reservoirs (Anglier, 2006) Another aspect of the process of precipitation is the possible contribution of increased mechanical strength of the rock as new minerals tends to clog and cement pores as seen for OBSV 9 (SSW). Hjuler and Fabricius (2009) found that calcite redistribution has strengthened particle contacts and reduced porosity, assumingly providing a geomechanically stronger chalk.

The initial abundance of non-calcite minerals seems to influence further precipitation and is therefore vital information. Primary porosity of the reservoir rock is essential to map as this property will strongly affect the following process of dissolution and distribution of precipitated minerals.

6.1 Reliability of data

The main issue when studying minerals that precipitate in chalk, is the accuracy of predicting the minerals due to their small grainsize. Thinsections may distribute various thickness which may influence the interpretation of minerals present. Optical properties are dependent of thickness to be correctly recognized. Error in preparation may have caused mis- interpretation. Samples may have been contaminated during preparation. The size of the minerals that precipitate in this study is small that it challenges various methods when determining the correct minerals. The diameter of the beam is likely larger than the size of the grain in focus, hence the surroundings may emit X-rays and further influence the EDS-results. This may challenge new precipitated minerals to be distinguished from adjacent grains and cause mis-interpretation. The examiners experience is another factor which could cause, like being

accurately enough concerning identification of peaks in XRD results. The width of the peaks in XRD, reflects the instrument´s analytical error; the smaller the grain, the higher the uncertainty.

7. Conclusions

The process of mineral precipitation and dissolution of a chalk seems to be dependent on several aspects. Circumstances that influence these processes are dependent on the composition of the brine injected, and further on the distribution of pore network. To study these factors for this project chalk from the Mons basin, has been used and flooded with NaCl, $MgCl_2$ and SSW. Three samples were hollow caused by a drilled hole with an approximately diameter of 3 mm, to observe possible changes in key parameter of a rock prone to hydrocarbon production, like porosity, permeability and mineralogy.

To acknowledge the process of mineral dissolution and precipitation, is it an advantage to be aware of the exact composition of the silicate content of the rock that it subjects to flooding. The reactivity of these minerals will determine further mineral exchange. Chlorite is the mineral that stands out and precipitate independently of which brine was injected. Magnesite and ilmenite dominate porous areas followed by $MgCl_2$ injection. TiO-mix and pyrite precipitate elsewhere in the matrix with a tendency to accumulate adjacent to high permeability zones. Next to chlorite, pyrite is highly abundant in the matrix resulted by SSW injection. Glauconite and authigenic feldspar is abundant in addition to a growth in chlorite when NaCl is introduced. Accumulation of precipitated minerals tend to increase with distance from the inlet, regarding all cores flooded by $MgCl_2$ and SSW. An opposite trend was only observed for cores injected by NaCl.

The composition of the brine is also subjected to influence dissolution of calcite. It is likely that pH-values determine the effect of dissolution. The dissolution of calcite seems to be more prominent when the chalk provides a homogeneous network of pores. When water flows through a fracture or high permeable zone, it tends to have a delayed transfer of fluid perpendicular to the flow direction. Hence it forms a primary dissolution adjacent the main water-transfer and allow the shaping of a “flushed zone” (Fig. 31 f). The hollow cylinder cores provide an overall lower distribution of calcite compared to nonfractured chalk.

Precipitation of minerals in the flooding experiment, seems here to distribute in a specific pattern. The diameter of a fracture diminishes and may occasionally seal off porous networks. By implementing water-injection to a reservoir, a high permeable zone will reduce and force the fluid into lower permeable zone. It has here been proven that the various brines have unlike properties in combination with different permeability zones. Before introducing a reservoir for

EOR methods, it is of significant value to map connectivity of pores and then introduce the optimal brine composition and increase the oil recovery.

8. Recommendations for further work:

- Further studies on the FIB-TEM samples that have been prepared is recommended. The diffraction patterns have not yet been assigned a specific mineral. Additional information may confirm, in details, precipitated minerals in the hollow cylinder. This may also amplify the two distinct calcite diffraction-patterns obtained by XRD.

- For additional method, it would be interesting to study specific surface area (SSA) applied to reference rock and to compare these results with both intact and hollow cylinder cores. It would be preferable to sample a series from the center core, the flushed zone, and the peripheral part of the core. It would be of interest to study the different result depending on brine injected. The impact of SSA in a water-wet reservoir will have high influence on the oil recovery factor. It is therefore of high interest to understand how SSA changes when injecting water into the reservoir.

- A further geochemistry study of each slice of all samples, would provide a more specific weight percent minerals when subjected for HCl and calcite vanish. A clear visualisation of amount distribution throughout the slices would be provided.

- Changing parameters of flooding set-up, for instance duration. What will happen if the flooding experiment continued will calcite be more dissolved and leave a higher porosity, or will minerals continue to precipitate and clog pores?

9. References

Agosta, F., and Aydin, A., 2006, Architecture and deformation mechanism of a basinbounding normal fault in Mesozoic platform carbonates, central Italy: Structural Geology, v. 28, no. 8, p. 1445-1467.

Andersen, P., Wang, W., Madland, M., Zimmermann, U., Korsnes, R., Bertolino, S., Minde, M., Schulz, B., and Gilbricht, S., 2017, Comparative study of five outcrop chalks flooded at reservoir conditions: chemo-mechanical behaviour and profiles of compositional alteration: Transport in Porous Media, v. 121, no. 1, p. 135-181.

Angeliera, J., Vandyckeb, S., Bergeratc, F., Gavigliod, P., Schroedere, C., and Coulonf, M., 2006, Can belemnite distribution reveal pressure-solution processes along faults? A case study in the chalk of the Mons Basin, Belgium: Journal of Structural Geology, v. 28, no. 64–82.

Bjørlykke, K., and Høeg, K., 1997, Effects on burial diagenesis of stress, compaction and fluid flow in sedimentary basins, 267-276 p.:

Boulvain, F., and Vandenberghe, N., 2018, An Introduction to the Geology of Belgium and Luxembourg.: Landscapes and Landforms of Belgium and Luxembourg. World Geomorphological Landscapes., p. 9-33.

Brace, W. F., 1980, Permeability of crystalline and argillaceous rocks: International Journal of Rock Mechanics and Mining Sciences & Geomechanics Abstracts, v. 17, no. 5, p. 241-251.

Callister, J. W. D., 2007, Material Science and Engineering. An Introduction., New York, Department of Metalurgical Engieering. The University of Utah.

Chester, F. M., Evans, J. P., and Biegel, R. L., 1993, Internal structure and weakening mechanisms of the San Andreas Fault: Journal of Geophysical Research: Solid Earth, v. 98, no. B1, p. 771-786.

Dubicka, Z., Wierzbowski, H., and Wierny, W., 2018, Oxygen and carbon isotope records of Upper Cretaceous foraminifera from Poland: vital and microhabitat effects: Palaeogeography, Palaeoclimatology, Palaeoecology, v. 500, p. 33-51.

Dusar, M., and Lagrou, D., 2007, Cretaceous flooding of the Brabant Massif and the lithostratigraphic characteristics of its chalk cover in northern Belgium, 27-38 p.:

Emery, D., and Robinson, A., 1993, Inorganic geochemistry; applications to petroleum geology, London, United Kingdom, Blackwell Scientific Publications.

Fabricius, I. L., 2003, How burial diagenesis of chalk sediments controls sonic velocity and porosity: AAPG Bulletin, v. 87, no. 11, p. 1755-1778.

-, 2007, Chalk: composition, diagenesis and physical properties: Bulletin of the Geological Society of Denmark, v. 55, p. 97-128.

Hancock, J. M., 1990, Cretaceous: Introduction to the Petroleum Geology of the North Sea, no. Oxford, p. 255-272.

Haupt, B. J., and Seidov, D., 2001, Warm deep-water ocean conveyor during Cretaceous time: Geology, v. 29, no. 4, p. 295-298.

Heggheim, T., Madland, M. V., Risnes, R., and Austad, T., 2005, A chemical induced enhanced weakening of chalk by seawater: Journal of Petroleum Science and Engineering, v. 46, no. 3, p. 171-184.

Hjelen, J., 1989, Scanning elektron-mikroskopi, Tronheim, Norway, Metallisk Institutt, NTH.

Hjuler, M., and Fabricius, I. L., 2009, Engineering properties of chalk related to diagenetic variations of Upper Cretaceous onshore and offshore chalk in the North Sea area: Journal of Petroleum Science and Engineering, v. 68, no. 3-4, p. 151-170.

Hull, D., and Bacon, D. J., 2011, Chapter 2 - Observation of Dislocations, *in* Hull, D., and Bacon, D. J., eds., Introduction to Dislocations (Fifth Edition): Oxford, Butterworth-Heinemann, p. 21-41.

Korsnes, R. I., Madland, M. V., Austad, T., Haver, S., and Røsland, G., 2008, The effects of temperature on the water weakening of chalk by seawater: Journal of Petroleum Science and Engineering, v. 60, no. 3, p. 183-193.

Krinsley, D. H., and Doornkamp, J. C., 1973, Atlas of Quartz Sand Surface Textures, London, Press, Cambridge Univ.

MacKenzie, W. S., and Adams, A. E., 1994, A colour atlas of rocks and minerals in thinsection: Rocks and minerals in thin section, London, Manson Publ.

Madland, M. V., Hiorth, A., Omdal, E., Megawati, M., Hildebrand-Habel, T., Korsnes, R. I., Evje, S., and Cathles, L. M., 2011, Chemical Alterations Induced by Rock–Fluid Interactions When Injecting Brines in High Porosity Chalks: Transport in Porous Media, v. 87, no. 3, p. 679-702.

Megawati, M., Madland, M. V., and Hiorth, A., 2015, Mechanical and physical behavior of high-porosity chalks exposed to chemical perturbation: Journal of Petroleum Science and Engineering, v. 133, p. 313-327.

Micarelli, L., Benedicto, A., and Wibberley, C. A. J., 2006, Structural evolution and permeability of normal fault zones in highly porous carbonate rocks: Journal of Structural Geology, v. 28, no. 7.

Michie, E. A. H., Haines, T. J., Healy, D., Neilson, J. E., Timms, N. E., and Wibberley, C. A. J., 2014, Influence of carbonate facies on fault zone architecture: Journal of Structural Geology, v. 65, p. 82-99.

Murphy, D. B., and Davidson, M. W., 2013, Fundamentals of Light Microscopy and Electronic Imaging, Hoboken, N.J, Wiley-Blackwell.

O'Brien, C. L., Robinson, S. A., Pancost, R. D., Sinninghe Damsté, J. S., Schouten, S., Lunt, D. J., Alsenz, H., Bornemann, A., Bottini, C., Brassell, S. C., Farnsworth, A., Forster, A., Huber, B. T., Inglis, G. N., Jenkyns, H. C., Linnert, C., Littler, K., Markwick, P., McAnena, A., Mutterlose, J., Naafs, B. D. A., Püttmann, W., Sluijs, A., van Helmond, N. A. G. M., Vellekoop, J., Wagner, T., and Wrobel, N. E., 2017, Cretaceous sea-surface temperature evolution: Constraints from TEX86 and planktonic foraminiferal oxygen isotopes: Earth-Science Reviews, v. 172, p. 224-247.

Olgaard, D. L., and Gerald, J. D. F., 1993, Evolution of pore microstructures during healing of grain boundaries in synthetic calcite rocks: Contributions to Mineralogy and Petrology, v. 115, no. 2, p. 138-154.

Paterson, M., 1973, Nonhydrostatic thermodynamics and its geologic applications: Reviews of Geophysics, v. 11, no. 2, p. 355-389.

Pirson, S., Spagna, P., Baele, J.-M., Damblon, F., Gerrienne, P., Vanbrabant, Y., and Yans, J., 2008, An overview of the Geology of Belgium, 5-25 p.:

Rigort, A., and Plitzko, J. M., 2015, Cryo-focused-ion-beam applications in structural biology: Archives of Biochemistry and Biophysics, v. 581, p. 122-130.

Risnes, R., 2001, Deformation and yield in high porosity outcrop chalk: Physics and Chemistry of the Earth, Part A: Solid Earth and Geodesy, v. 26, no. 1, p. 53-57.

Risnes, R., Madland, M., Hole, M., and Kwabiah, N., 2005, Water weakening of chalk—Mechanical effects of water–glycol mixtures: Journal of Petroleum Science and Engineering, v. 48, no. 1-2, p. 21-36.

Snow, S. E., and Brownlee, M. H., 1989, Practical and Theoretical aspects of Well Testing in the Ekofisk Area Chalk Fields.: SPE Annual Technical Conference and Exibition.

Strand, S., Hjuler, M., Torsvik, R., Pedersen, J., Madland, M., and Austad, T., 2007, Wettability of chalk: impact of silica, clay content and mechanical properties: Petroleum Geoscience, v. 13, no. 1, p. 69-80.

Strand, S., Standnes, D. C., and Austad, T., 2003, Spontaneous Imbibition of Aqueous Surfactant Solutions into Neutral to Oil-Wet Carbonate Cores: Effects of Brine Salinity and Composition: Energy & Fuels, v. 17, no. 5, p. 1133-1144.

Sulak, R. M., and Danielsen, J., 1989, Reservoir Aspects of Ekofisk Subsidence.

Sylvester, P. J., 2012, Use of the mineral liberation analyzer (MLA) for mineralogical studies of sediments and sedimentary rocks: Quantitative Mineralogy and Microanalysis of Sediments and Sedimentary Rocks (P. Sylvester, ed.). Mineralogical Association of Canada Short Course Series, v. 42, p. 1-16.

Tanner, R. S., Udegbunam, E. O., McInerney, M. J., and Knapp, R. M., 1991, Microbially enhanced oil recovery from carbonate reservoirs: Geomicrobiology Journal, v. 9, no. 4, p. 169-195.

Zhou, G.-T., and Zheng, Y.-F., 2001, Chemical synthesis of $CaCO_3$ minerals at low temperatures and implication for mechanism of polymorphic transition: N.Jb.Miner.Abh, v. 176, no. 3, p. 323-343.

Ziegler, P. A., 1990, Geological atlas of Western and Central Europe, Amsterdam, Elsevier, Shell International Petroleum.

10. Appendix

App. A) Composition of injected brines utilized in previous experiment of studied chalk.

Brine	SSW [g/l]	0.219 M $MgCl_2$ [g/l]	0.675M NaCl [g/l]
NaCl	23.38		38.4
$MgCl_2$ $6H_2O$	9.05	44.5	
Na_2SO4	3.14		
Na HCO3	0.17		
KCl	0.75		
$CaCl_2$ $2H_2O$	1.91		

App. B) Effluent water for the various cores flooded in previous test.

Core	Mineral	Original	Effluent	Change in M
OBSV 9 Intact SSW	Sulphate	0.024	0.015	-0.009
	Calcium	0.013	0.016	0.003
	Magnesium	0.045	0.031	-0.014
	Potassium	0	0.011	0.011
OBSV 6 Intact $MgCl_2$	Chloride	0.43	0.431	0.001
	Calcium	0	0.02	0.02
	Magnesium	0.219	0.203	-0.016
OBSV 4 Fracture $MgCl_2$	Sodium	0	0.015	0.015
	Chloride	0.44	0.445	0.005
	Calcium	0	0.015	0.015
	Magnesium	0.219	0.208	-0.011
OBSV 12 Fracture SSW	Sodium	0.44	0.44	0
	Chloride	0.52	0.52	0
	Sulphate	0.024	0.024	0
	Calcium	0.013	0.016	0.003
	Magnesium	0.045	0.041	-0.004
	Potassium	0.01	0.01	0

App. C) Permeability for intact cores pre and post-flooding.

Sample	Initial value	Post flooding
OBSV 6 ($MgCl_2$)	0,53 mD	0,17 mD
OBSV 9 (SSW)	0,59 mD	0,00 mD

App. D) Wt% distribution of minerals by MLA-method

Mineral	4-6 GXMAP Wt%	4-1 GXMAP Wt%	18-1 GXMAP Wt%	18 Wt%	12-6 GXMAP Wt%	12-2 GXMAP Wt%	REF GXMAP Wt%	9-6 GXMAP Wt%	9-1 GXMAP Wt%	6-6 GXMAP Wt%	6-1 GXMAP Wt%
Quartz	0.12	0.39	0.49	0.35	0.33	0.27	0.47	0.46	0.42	0.09	0.04
Magnesite	0.00	0.00	0.00	0.00	0.00	0.00	0.00	0.00	0.00	0.00	0.03
FeCaO_Siderite	0.03	0.03	0.10	0.11	0.01	0.01	0.08	0.07	0.07	0.02	0.01
Calcite_2	35.17	24.93	37.34	30.56	35.04	30.29	28.14	27.04	26.29	32.48	28.54
Calcite_1	0.00	0.03	0.00	0.10	0.01	0.05	0.03	0.08	0.04	0.18	0.00
Calcite_0	56.51	69.24	54.76	63.43	55.92	64.28	66.89	67.55	68.31	57.04	62.61
Orthoclase	0.04	0.18	0.27	0.29	0.24	0.14	0.24	0.24	0.20	0.06	0.01
Muscovite	0.18	0.31	0.27	0.34	0.31	0.28	0.29	0.30	0.33	0.34	0.19
Clinochlore	0.01	0.00	0.00	0.00	0.00	0.00	0.00	0.00	0.00	0.01	0.02
CaSiMgO-chlorite	6.19	3.17	3.90	2.49	4.42	2.84	1.97	2.48	2.61	5.85	6.94
Clay	0.08	0.00	0.00	0.00	0.01	0.01	0.00	0.00	0.00	0.11	0.15
FeO	0.03	0.02	0.08	0.07	0.01	0.00	0.03	0.03	0.07	0.02	0.01
Ilmenite	0.00	0.01	0.01	0.01	0.00	0.00	0.01	0.00	0.01	0.00	0.00
TiO	0.02	0.02	0.02	0.02	0.02	0.01	0.02	0.01	0.03	0.01	0.01
TiO-Qz	0.00	0.00	0.00	0.00	0.00	0.00	0.00	0.00	0.00	0.00	0.00
TiO-CC-mix	0.73	0.88	0.77	1.00	1.02	0.48	0.70	0.72	0.63	2.43	0.72
Pyrite	0.00	0.00	0.00	0.00	0.02	0.01	0.00	0.00	0.00	0.04	0.00
Pyrite_Cc	0.00	0.00	0.00	0.00	1.22	0.51	0.00	0.00	0.01	0.73	0.04
Apatite	0.02	0.00	0.01	0.01	0.00	0.00	0.01	0.01	0.02	0.01	0.01
PCaMgKSiO	0.00	0.00	0.00	0.00	0.00	0.00	0.00	0.00	0.00	0.00	0.00
Zircon	0.00	0.00	0.00	0.00	0.00	0.00	0.00	0.00	0.01	0.00	0.00
CaSiAlSKO	0.13	0.24	0.33	0.36	0.39	0.25	0.31	0.27	0.30	0.21	0.12
CaSiFePAlKMgO	0.63	0.38	1.33	0.62	0.81	0.42	0.52	0.49	0.45	0.32	0.40
SiCaO	0.03	0.10	0.20	0.17	0.12	0.08	0.19	0.18	0.12	0.02	0.05
SiCaNaMgO	0.06	0.05	0.10	0.07	0.07	0.05	0.07	0.06	0.06	0.01	0.07
SiC	0.02	0.00	0.01	0.01	0.01	0.00	0.01	0.00	0.01	0.00	0.01
CuZnPbO	0.01	0.00	0.00	0.01	0.00	0.00	0.00	0.00	0.00	0.00	0.00
Unknown	0.00	0.00	0.00	0.00	0.00	0.00	0.00	0.00	0.00	0.00	0.00
Low_Counts	0.00	0.00	0.00	0.00	0.00	0.00	0.00	0.00	0.00	0.00	0.00
No_XRay	0.00	0.00	0.00	0.00	0.00	0.00	0.00	0.00	0.00	0.00	0.00
Total	100.00	100.00	100.00	100.00	100.00	100.00	100.00	100.00	100.00	100.00	100.00